



Master's Thesis in Quantum Engineering

Academic Year 2024/2025

Superconducting Isolator Design and High Power Impulse Magnetron Sputtering Optimization

of NbTiN/NbN Thin Films

Lorenzo Barbati

Academic Supervisors:

Dr. Erik Piatti – Politecnico di Torino

Prof. Marco Colangelo – Northeastern University

October 20, 2025

Contents

A	cknov	wledgen	ments	6					
\mathbf{A}	bstra	\mathbf{ct}		:					
In	trodi	uction		i					
1	Dep	Deposition of Superconducting Nitride Thin Films: Materials and Methods							
	1.1	Context	t and Scope	1					
	1.2	Key Su	perconducting Parameters and Physical Meaning	1					
	1.3	Device	Figures of Merit	2					
	1.4	Magnet	ron Sputtering: Working Principles, DC vs HiPIMS, and Process Control	3					
		1.4.1	Working Principles	3					
		1.4.2	DC vs HiPIMS	3					
		1.4.3	Physically Meaningful Process Parameters	3					
	1.5	Operati	ive Considerations	4					
	1.6	Deposit	tion Overview	4					
	1.7		and HIPIMS	Ę					
	1.8		ates, Buffers, and Texture Control	6					
			Buffer engineering: Nb_5N_6 on Si	7					
			AlN templates for δ -NbN and NbTiN	7					
			Substrate choice and texture	7					
			Implications for device integration	7					
			Experimental values in NbTiN and NbN	7					
	1.9	Process	S-Structure-Property Links	8					
	1.10	Conclus	sions	Ć					
2			of Superconducting Nitride Thin Films: Results and Discussion	10					
	2.1		Overview	10					
	2.2		llable Deposition Parameters	10					
			Sputtering Current and Target Power	10					
			Working Pressure	10					
			Argon Flow	11					
			Nitrogen Flow	11					
			Substrate Temperature	11					
			Sputtering Angle α	11					
			Target–Substrate Distance L	12					
			Process Pressure and Plasma Diagnostics	12					
	2.3		ce of Parameters on Film Properties	12					
		231	Voltage-Current Mapping for Stoichiometry Control	13					

	2.4	Structural characterization
	2.5	Cryogenic Setup for T_c Measurements
		2.5.1 Chamber Assembly
	2.6	Superconducting Transition Measurements
		2.6.1 Discussion
	2.7	Results
	2.,	2.7.1 Niobium Nitride Films 24
		2.7.2 High Power Impulse Magnetron Sputtering
		2.7.2 High Fower Impulse Magnetion Sputtering
		v .
		2.7.5 Comparative Performance
3	Sup	erconducting Isolator: Theory and Literature Overview 29
	3.1	Introduction and scope
	3.2	Josephson nonlinearity in a transmission-line unit cell
	3.3	Four-wave mixing and coupled-mode gain
	3.4	Parametric amplification and the applied modulation
	3.5	Resonant phase matching: pump-selective dispersion engineering
	3.6	Bandwidth and gain flatness
	3.7	Noise and the quantum limit
	3.8	Dynamic range, saturation, and intermodulation
	3.9	Comparison with alternative dispersion strategies
		Magnet-free nonreciprocal isolator via traveling index modulation
		Sketch of the coupled-mode derivation
		KI-TWPA Synthesis for Isolator Design
		Implementation and Materials
		Fabrication and Material Requirements
	5.14	
	9 15	3.14.1 Superconducting Materials and Film Quality
	5.10	Applications and System Integration
	2.16	3.15.1 Quantum Computing Applications
	3.10	Future Directions
		3.16.1 Advanced Modulation Schemes
		3.16.2 Integration with Emerging Quantum Technologies
4	Sup	erconducting Isolator:
	_	ulation and fabrication 42
	4.1	Simulation of the CPW Isolator
		4.1.1 Workflow
		4.1.2 Extension to Reverse Transmission
	4.2	Process Overview
		4.2.1 CPW Layer Stack and Cross-Section Schematic
	4.3	Substrate Preparation
	4.4	Reactive Sputter Deposition of NbTiN
	4.5	ZEP 530 Coating and Prebake
	4.6	HS50 Electron-Beam Lithography
	4.7	Cold Development (ZEP)
	4.8	Dry Etch of NbTiN (Pattern Transfer)
	4.9	Resist Strip with Remover 1165
	_	Metrology, Acceptance, and Impact on RF Performance
	4.10	Troubleshooting and Run-to-Run Notes
	4.11	Troublebrooming and run-10-run roles

	4.12	Run Sheet (example targets)	47
	4.13	Device Micrographs and Layout Notes	47
		Klopfenstein Taper Synthesis and Layout	49
	4.15	Results and Discussion	52
		4.15.1 Frequency Selection and Resonant Shape Evolution	52
		4.15.2 Effect of Apodization via a Third Loading Structure	54
		4.15.3 Evaluation of Idler versus Source Frequency Response	56
		4.15.4 Optimization through Bias Current and Line Length	57
		I_c testing	57
		Measurement Principle	58
		Results and Discussion	59
	4.19	Implications for Spiral-Based Devices	59
5	Circ	culator	60
	5.1	System Architecture and Integration	60
		5.1.1 Four-Port Circulator Topology	60
		5.1.2 Scattering Matrix Formulation	61
	5.2	Component Implementation Details	61
		5.2.1 Parametric Isolator Design	61
		5.2.2 High-Impedance Directional Coupler Theory	62
		5.2.3 Directional Coupler Implementation	64
	5.3	Operational Analysis and Performance	65
		5.3.1 Signal Flow and Circulation Mechanism	65
	5.4	Theoretical Performance Limits	66
	5.5	Integration with Emerging Quantum Technologies	66
	5.6	Conclusion	66
6	Con	clusions	68
Co	onclu	sions	68
	6.1	Summary of Achievements	68
	6.2	Limitations and Challenges	69
	6.3	Future Work and Research Directions	70
		6.3.1 HiPIMS Parameter	70
		6.3.2 Device Testing with FPGA Control	71
		6.3.3 Circulator Fabrication and Experimental Demonstration	71
	6.4	Broader Impact and Concluding Remarks	72

List of Acronyms

NbN Niobium Nitride

NbTiN Niobium Titanium Nitride

HiPIMS High Power Impulse Magnetron Sputtering

DCMS Direct Current Magnetron Sputtering

TWPA Travelling-Wave Parametric Amplifier

KIT Kinetic Inductance TWPA

SNSPD Superconducting Nanowire Single-Photon Detector

3WM Three-Wave Mixing

4WM Four-Wave Mixing

WHH Werthamer-Helfand-Hohenberg (theory of upper critical fields)

AFM Atomic Force Microscopy

SEM Scanning Electron Microscopy

XPS X-ray Photoelectron Spectroscopy

RBS Rutherford Backscattering Spectroscopy

EDS Energy Dispersive Spectroscopy

Tc Critical Temperature

Hc2 Upper Critical Magnetic Field

OES Optical Emission Spectroscopy

CPW Coplanar Waveguide

GBP Gain-Bandwidth Product

SDE System Detection Efficiency

PEC Proximity Effect Correction (in lithography)

DBR Distributed Bragg Reflector

DCMS Direct Current Magnetron Sputtering

TEM Transmission Electron Microscopy

XRD X-ray Diffraction

XRD X-ray Diffraction

SAED Selected Area Electron Diffraction

HRTEM High-Resolution Transmission Electron Microscopy

HAADF-STEM High-Angle Annular Dark-Field Scanning Transmission Electron Microscopy

 ${\bf RHEED}$ Reflection High-Energy Electron Diffraction

 $\mathbf{MBE} \quad \text{Molecular Beam Epitaxy}$

 ${\bf XANES}\,$ X-ray Absorption Near-Edge Structure

 \mathbf{XPS} X-ray Photoelectron Spectroscopy

RBS Rutherford Backscattering Spectroscopy

Acknowledgements

I would like to express my sincere gratitude to all those who have supported and guided me throughout this research journey.

First and foremost, I am deeply grateful to my supervisors, Dr. Erik Piatti and Prof. Marco Colangelo, for their invaluable guidance, expertise, and patience throughout this work. Their insights into superconducting materials and quantum devices have been instrumental in shaping both this thesis and my understanding of the field. I am particularly thankful for their willingness to discuss challenges openly and for encouraging me to develop a rigorous scientific approach.

I would like to acknowledge Politecnico di Torino for providing me with an outstanding educational foundation throughout my Master's degree and for the opportunity to pursue this degree program in Quantum Engineering. The knowledge and skills I acquired there have been fundamental to this research work.

My gratitude extends to Northeastern University for hosting me during my thesis work and for providing access to excellent research facilities and technical support. I am particularly grateful to the technical staff for their assistance with the experimental facilities, especially with the AJA Orion sputtering system and cryogenic measurement setups. This international experience has greatly enriched my academic journey and broadened my perspective on research.

I am especially grateful to my dear friend and colleague Federica Marinelli who has been like a sister to me throughout this journey. I consider myself truly fortunate to have had the opportunity to work alongside her these past months. I hope that our paths will cross again for future collaborations. Her unwavering support and friendship represent one of the greatest gifts of this entire experience.

I wish to thank my fellow students in the Quantum Engineering program, particularly Emanuele and Antonio, for the stimulating discussions, shared challenges, and mutual encouragement.

A special thanks to the Boston group, including Davide, Giacomo, Ilaria, Nicole and all the others, for making my time there unforgettable. Your warmth, friendship, and support helped me feel at home in a new city and made the experience both personally and academically rewarding.

A special thanks goes to the members of the Eta Kappa Nu honor society for welcoming me into such a stimulating environment. Being part of this community has brought me great satisfaction and has enriched my academic experience in ways I had not anticipated.

I am also grateful to my Roma and Pisa groups for making this experience memorable and for the sense of community that made being far from home easier. Especially to my friends Daniele, Leonardo, Fabrizio, Marco, Lorenzo, Alessio, Giulio, Giovanni, and Alessandro: thank you for your constant support, for the moments of joy and distraction, and for always being there when I needed to step away from research and simply enjoy life. Your friendship has been a source of strength and balance.

My deepest gratitude goes to my parents Adriana and Giovanni and my family for their unconditional love, support, and encouragement throughout my entire academic journey. Their sacrifices, understanding, and belief in me have made all of this possible. I am forever grateful for everything they have done for me.

Finally, I would also like to acknowledge the people I have met and, unfortunately, lost along this journey. Every relationship, however brief, has contributed to shaping who I am today, and I am grateful for the lessons learned and the moments shared.

This research has been a profound learning experience, and I am grateful to everyone who contributed to it in ways both large and small.

Lorenzo Barbati

Abstract

The advancement of superconducting quantum computing technologies increasingly relies on the availability of low-loss, wide-bandwidth microwave amplifiers and non-reciprocal components such as isolators and circulators. This thesis addresses two principal challenges in this context: the optimization of superconducting nitride films through advanced deposition techniques and the realization of magnet-free non-reciprocal devices based on parametric modulation.

On the materials side, the main focus is on ultrathin niobium nitride (NbN) and niobium titanium nitride (NbTiN) films, whose superconducting properties are strongly influenced by stoichiometry, disorder, and microstructure. High Power Impulse Magnetron Sputtering (HiPIMS), an advanced deposition technology, is employed to systematically investigate and optimize process parameters for NbN and NbTiN, with the goal of surpassing conventional Direct-Current Magnetron Sputtering (DCMS) methods. HiPIMS is shown to generate denser films with enhanced critical temperatures, thereby providing a solid foundation for the fabrication of superconducting devices.

Building on these material advances, the work progresses toward non-reciprocal superconducting circuits. A travelling-wave parametric amplifier (TWPA) based on NbTiN transmission lines is adapted to operate as a parametric isolator, exploiting the nonlinear kinetic inductance of thin films under parametric pumping. In parallel, the high-impedance forward coupler introduced by Colangelo et al. is adopted as a compact and scalable element to interconnect isolators. A potential four-port circulator architecture is proposed by merging these devices, enabling magnet-free non-reciprocity.

This thesis outlines a comprehensive framework that encompasses both HiPIMS-based thin-film optimization and the design of superconducting isolators and circulators. By merging advanced thin-film engineering with novel circuit topologies, it provides a new pathway for their integration into next-generation quantum computing and cryogenic detection systems.

Introduction

The development of quantum information and quantum sensing technologies critically depends on the availability of low-noise, broadband, and scalable microwave components. Among these, parametric amplifiers have become indispensable as near-quantum-limited front-end devices for qubit readout, dark-matter searches, and precision sensing. Conventional Josephson parametric amplifiers¹, while successful in achieving quantum-limited noise performance, remain constrained by narrow bandwidths, low dynamic range, and vulnerability to magnetic fields. Travelling-wave parametric amplifiers (TWPAs)² provide a natural path to overcome these limitations by distributing nonlinearity over centimeter-scale transmission lines and thereby achieving multi-gigahertz gain bandwidths.

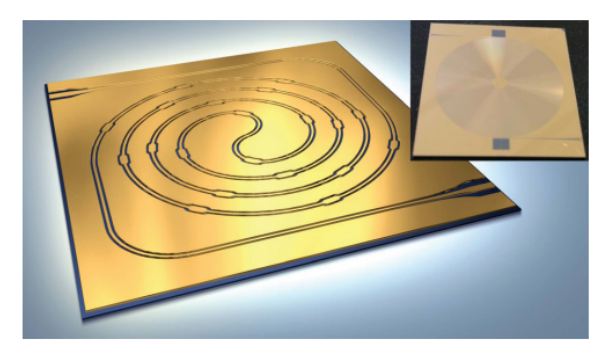


FIG. 1. Stylized illustration of the kinetic inductance traveling-wave (KIT) amplifier CPW with tapered launches and loadings. The inset shows photograph of the actual 2 cm \times 2 cm chip with a 2 m spiral.

Figure 1: Reproduced from Ref.[1]

Within this framework, kinetic inductance TWPAs (KITs) exploit the current-dependent inductance of superconductors such as NbN and NbTiN and represent a compelling alternative to Josephson-based devices. KITs feature simplified fabrication, resilience to magnetic fields, and dynamic ranges orders of magnitude higher than Josephson counterparts. However, their performance has historically been critized by high pump power requirements, dispersion engineering challenges, and difficulties in reproducible film growth. Recent work has demonstrated that dispersion-engineered architectures

¹A Josephson Parametric Amplifier (JPA) is a superconducting microwave device that exploits the nonlinear inductance of Josephson junctions to provide phase-sensitive or phase-insensitive amplification of weak quantum signals. By modulating the junction's inductance with a strong pump tone near twice the signal frequency, the JPA enables nearly quantum-limited amplification, making it essential in superconducting qubit readout and quantum measurement systems.

²A Travelling-Wave Parametric Amplifier (TWPA) is a broadband superconducting amplifier that utilizes the distributed nonlinear inductance of a transmission line loaded with Josephson junctions or kinetic-inductance elements. By launching a strong pump tone that co-propagates with the signal, the TWPA achieves continuous parametric interaction along its length, enabling wideband, near quantum-limited amplification with high dynamic range, crucial for multiplexed qubit readout and low-noise cryogenic detection.

such as stub-loaded coplanar waveguides and inverted microstrip lines can mitigate phase-matching limitations and reduce pump power to experimentally viable levels.

:	SYSTEM DETECTION	ON EFFICIENCY				
COUPLING EFFICIENCY		ABSORPTION EFFICIENCY	INTRINSIC EFFICIENCY	DARK COUNT RATE	COUNT RATE	JITTER
Distance	Nanowire film properties	High [22]	High [26]	Low [26]	High [38]	Low [38]
between fiber end and SNSPD [1]	Nanowire geometry:					
In-plane	Thickness	High [22]	High [27]	No	High [26]	No
misalignment	Width	No	High [27]	No	High [26]	No
between optical fiber	Length	No	No	No	High [26]	Low [42]
and SNSPD active area [21]	Fill-factor	High [23]	No	No	No	No
	Nanowire design	No	High [27]	High [27]	No	No
SNSPD active area [20]	Optical cavities	High [24]	No	No	No	No
active area [20]	Bias current	No	High [28]	High [29]	High [40]	High [41]
	Bath temperature	No	High [28]	High [29]	No	Low [43]
	External noise	No	No	High [32]	No	High [44]
	Measurement setup	No	No	No	High [39]	Low [41]
	Light polarization	High [20]	No	No	No	No
	Photon wavelength	High [25]	High [29]	No	Low [40]	No
	Photon flux	No	High [1]	Low [32]	High [1]	No

Figure 2: Hierarchical breakdown of factors affecting system detection efficiency (SDE) in superconducting nanowire single-photon detectors (SNSPDs). High coupling efficiency and absorption efficiency require optimization of optical cavity design; high intrinsic efficiency demands precise control of nanowire geometry and film critical temperature; low dark count rate depends on film uniformity and operating temperature; high count rate is enabled by short recovery time, set by kinetic inductance; and low jitter requires high slew rate during resistive transition. This diagram emphasizes that film T_c and sheet resistance—parameters directly controlled by HiPIMS deposition—are central to multiple performance metrics. (Reproduced from Ref.[2])

The present thesis builds on the ground of a dual objective. First, it addresses the optimization of NbN and NbTiN ultrathin films via High Power Impulse Magnetron Sputtering (HiPIMS). Compared to the traditional Direct Current Magnetron Sputtering (DCMS), this relatively novel deposition technique is capable of enhancing density, stoichiometric control, and thus superconducting performance compared to conventional sputtering. The goal is to reproduce and possibly surpass state-of-the-art film properties reported in the literature, thereby establishing a robust materials platform for device fabrication. These results could not only be useful in terms of the TWPA, but also in terms of Superconducting Nanowire Single Photon Detectors (SNSPDS)³. As stated by Ilya A. Stepanov et al. [2], the properties of these devices are strongly influenced by the nanowire material's characteristics, mainly the critical temperature and sheet resistance. With HIPIMS it is possible to further set other parameters, such as the refractive index n and k, mainly using NbTiN as stated by Del Giudice et al. [3].

Second, it translates these material improvements into circuit-level demonstrations, beginning with the adaptation of KITs into parametric isolators and culminating in the conceptual design of a superconducting circulator. The former is based on a broadband amplifier device designed by Eom et al. [4]. By exploiting the band engineering exploiting three-wave mixing (3WM) and periodic loadings, it is possible to implement a time modulated isolator. The design starts based on the theory by Pappas

³A superconducting nanowire single-photon detector (SNSPD) consists of a narrow, current-biased superconducting strip operated close to its critical current. Absorption of a single photon locally breaks Cooper pairs, forming a resistive hotspot that momentarily diverts the bias current and generates a measurable voltage pulse. After thermal relaxation and current recovery, the device returns to the superconducting state, allowing subsequent detections with sub-nanosecond reset times and near-unity quantum efficiency.

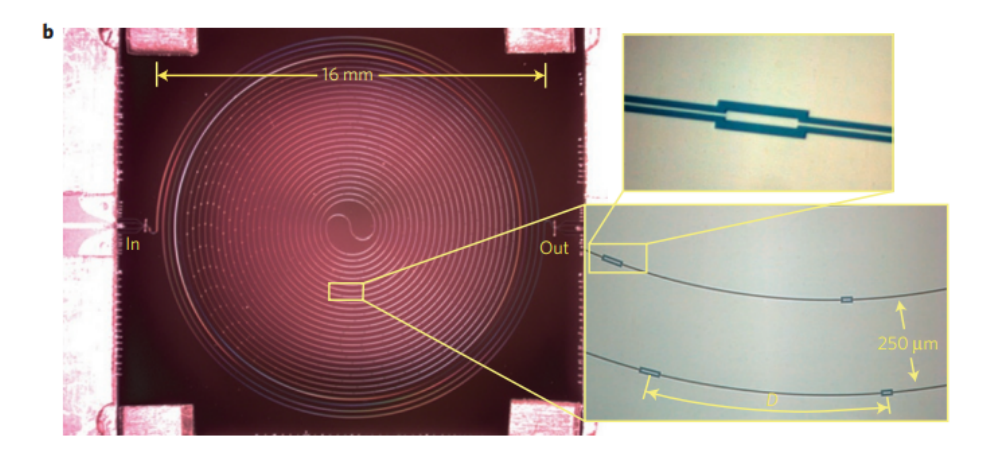


Figure 3: Optical micrograph of a fabricated KIT-TWPA device showing the Eom et al. broadband amplifier. Reproduced from Ref.[4]

et al. and the simulation framework proposed by Sweetnam et al. [1]. The latter is envisioned as a modular device that integrates isolators with the high-impedance forward coupler introduced by Colangelo et al. [5]. This component allows to implement isolation in a four port circulator allowing a viable route to magnetic-field-free non-reciprocal circuits for scalable quantum technologies.

Thesis Objectives

This thesis addresses the optimization of superconducting nitride thin films and their application in non-reciprocal quantum microwave devices through an integrated experimental and theoretical program.

Primary Objectives

HiPIMS Process Development for Superconducting Nitrides

The first objective establishes a complete deposition process for ultrathin NbN and NbTiN films using the AJA Orion sputtering system. Beginning with a baseline DCMS process for reactive NbN deposition, the work progresses to implementing High Power Impulse Magnetron Sputtering (HiP-IMS) with the goal of demonstrating superior film properties. The central hypothesis is that HiPIMS will deliver enhanced critical temperatures, narrower superconducting transitions, and improved film uniformity compared to DCMS at device-relevant thicknesses between 5 and 10 nm. Success is defined as achieving comparable T_c for NbN films deposited by HiPIMS with thickness around 10nm, representing a measurable improvement over DCMS baseline performance. This comparison directly addresses whether the increased complexity and cost of HiPIMS deposition is justified for quantum device fabrication.

Voltage-Current Discharge Mapping for Stoichiometry Control

The second objective develops a reproducible diagnostic method for reactive sputtering process control. By systematically mapping discharge voltage versus current characteristics across varying nitrogen flows, the work establishes quantitative relationships between target state, nitrogen incorporation, and resulting film properties. This approach moves beyond reliance on nominal flow rates alone, which are subject to chamber conditioning effects and hysteresis. The goal is to demonstrate

that discharge voltage at fixed current serves as a reliable proxy for nitrogen concentration in the growing film, enabling process specifications based on measurable $\{V, I\}$ operating points. Validation requires correlating these electrical signatures with compositional analysis and superconducting transition measurements across multiple deposition runs.

Design and Simulation of Parametric Isolators

The third objective translates optimized thin-film properties into functional non-reciprocal devices. This work develops a dispersion-engineered coplanar waveguide architecture employing periodic impedance loading to enable three-wave mixing processes. Following the theoretical framework established by Erickson and Pappas and the simulation methodology demonstrated by Sweetnam et al., the design targets forward transmission better than -1 dB with reverse isolation exceeding 20 dB across a 300–500 MHz bandwidth centered near 5 GHz. A critical component is the synthesis of Klopfenstein impedance tapers that provide broadband matching between high-impedance spiral sections (150–300 Ω) and standard 50 Ω measurement environments while maintaining in-band reflections below -20 dB. The simulation phase validates phase-matching conditions, predicts achievable isolation performance, and identifies optimal pump frequencies and power levels before committing to fabrication.

Fabrication and Initial Characterization of Isolator Structures

The fourth objective establishes a complete microfabrication process flow for realizing the designed isolator structures. This encompasses optimized NbTiN reactive sputtering, electron-beam lithography with ZEP 530 resist using a 50 kV HS50 writer, cold development at 0 °C for enhanced resolution, and pattern transfer via inductively coupled plasma reactive ion etching. Successful implementation requires achieving sub-micrometer lithographic fidelity in the periodic loading features while maintaining clean, vertical sidewalls and minimal edge roughness. Initial device characterization focuses on DC transport measurements including critical current extraction from fabricated spiral structures and four-point resistance versus temperature sweeps to verify that patterned devices retain superconducting properties comparable to blanket films. These measurements validate both the fabrication process and provide essential calibration data for the nonlinear kinetic inductance parameters required in parametric device models.

Secondary Objectives

Beyond the primary experimental and design goals, two supporting objectives enable the core work. First, the design and validation of a compact cryogenic measurement station provides the infrastructure for reproducible T_c characterization between 4 and 20 K with temperature stability better than 0.1 K and the capability to measure multiple samples in parallel. This system enables rapid feedback during process optimization and forms the basis for future RF measurements at cryogenic temperatures.

Second, a conceptual four-port circulator architecture is proposed that integrates two parametric isolators with a high-impedance forward directional coupler following the design principles established by Colangelo et al. While experimental realization of this circulator lies beyond the present thesis scope, the theoretical framework and simulation-based feasibility analysis demonstrate that magnet-free non-reciprocal signal routing for quantum computing applications represents a natural extension of the isolator development. This architectural proposal identifies specific fabrication requirements, integration challenges, and performance trade-offs that will guide future experimental efforts toward scalable quantum-compatible circulators.

Success Criteria and Expected Outcomes

The thesis will be considered successful upon meeting the following criteria. For the materials development, HiPIMS-deposited NbN films must demonstrate quantifiable T_c values comparable to DCMS baseline, with a target increase of at least 1.5 K at matched thickness and deposition temperature. The voltage–current mapping methodology must establish a reproducible process window showing clear correlation between discharge characteristics and film superconducting properties across a minimum of five distinct deposition conditions. For device development, a complete fabrication process must be documented with demonstrated lithographic fidelity suitable for sub-micrometer coplanar waveguides (CPW) features and periodic loading structures. Simulated isolator designs should predict isolation exceeding 20 dB with insertion loss below 1 dB over bandwidths greater than 300 MHz. At least one fabricated spiral structure must exhibit a measurable superconducting transition with extracted critical current values consistent with design parameters and literature scaling relationships. These outcomes collectively establish both an improved materials platform and a validated pathway toward experimental demonstration of superconducting parametric isolators for quantum technologies.

CHAPTER 1

Deposition of Superconducting Nitride Thin Films: Materials and Methods

This chapter establishes the materials background and process windows relevant to ultrathin niobium nitride (NbN) and niobium—titanium nitride (NbTiN) films for cryogenic quantum applications, with emphasis on superconducting nanowire single-photon detectors (SNSPDs). This chapter (i) reviews the governing superconducting parameters and their dependence on thickness and composition, (ii) compares NbTiN and NbN under near-optimal reported conditions, (iii) discusses energetic sputtering routes (with qualitative notes on HiPIMS versus DCMS), (iv) delineates stoichiometry windows and substrate/buffer strategies directly supported by the selected literature, and (v) connects microstructure to the upper critical field and coherence length using experimentally grounded models. Where available, quantitative values are taken from peer-reviewed reports included in this thesis reference set.

1.1 Context and Scope

This chapter focuses on the fabrication and process optimization of superconducting thin films and devices. To make the ensuing sections accessible beyond specialists, we first consolidate the general physical context and the performance metrics of interest. Accordingly, we (i) review the primary superconducting parameters that delimit device operation, (ii) formalize the figures of merit used to evaluate device performance (with emphasis on detectors and high-impedance microwave structures), and (iii) summarize the working principles of magnetron sputtering—including the differences between DC and high-power impulse magnetron sputtering (HiPIMS)—together with the physically meaningful process knobs that control microstructure and, ultimately, device-relevant properties. These additions provide a common foundation before entering the details of process windows and optimization.

Roadmap. Section 1.2 introduces the key superconducting parameters and their physical meaning. Section 1.3 defines the device figures of merit used throughout this work. Section 1.4 gives a compact, physics-based overview of magnetron sputtering and the specific levers used in DC and HiPIMS to tune film properties.

1.2 Key Superconducting Parameters and Physical Meaning

Critical temperature T_c . T_c marks the transition to the superconducting state where resistivity vanishes and long-range phase coherence emerges. For conventional s-wave materials, the zero-

temperature gap follows the BCS scaling $\Delta(0) \approx 1.764 \, k_B T_c$. In thin, disordered films relevant to high-impedance devices, T_c is sensitive to stoichiometry, disorder, and strain; it sets the thermal operating window and impacts nonlinearity and kinetic inductance.

Superconducting gap Δ . Δ sets the minimum energy to break Cooper pairs and controls the quasiparticle population. It governs microwave losses at cryogenic temperatures and, via $\Delta(0)$, enters depairing currents and the density of states relevant to detection thresholds.

London penetration depth λ_L . λ_L quantifies the depth over which magnetic fields decay in a superconductor and is inversely proportional to the superfluid density. For films with thickness $t \ll \lambda_L$, the sheet kinetic inductance is approximately

$$L_{\square} \simeq \mu_0 \, \frac{\lambda_L^2}{t},$$
 (1.1)

which directly impacts microwave impedance, dispersion, and reset times in nanowire devices.

Coherence length ξ . ξ is the characteristic size over which the order parameter varies. In the clean limit, $\xi(0) \sim \hbar v_F/(\pi \Delta)$, whereas in the dirty limit $\xi(0) \sim \sqrt{\hbar D/(2\pi k_B T_c)}$ with diffusion constant D. It sets the core scale of vortices and enters the upper critical field.

Upper critical field H_{c2} . $H_{c2}(0) \approx \Phi_0/(2\pi\xi^2)$ (with Φ_0 the flux quantum) denotes the field above which superconductivity is destroyed. Large H_{c2} is beneficial for robustness against stray fields and for maintaining superconductivity in narrow, thin films.

Critical current and current density (I_c, J_c) . J_c is limited by pair-breaking, current crowding, edge roughness, and vortex entry at inhomogeneities. In practice, device bias I_b is chosen below I_c to guarantee stability while retaining sufficient nonlinearity or detection probability.

Normal-state resistivity ρ_n and film thickness t. ρ_n and t control sheet resistance $R_{\square} = \rho_n/t$, which correlates with disorder, kinetic inductance, and microwave loss. Tight control of t is essential for reproducible Z_0 and L_{\square} .

Schematic: interplay among T_c , Δ , λ_L , ξ , H_{c2} and device-relevant quantities (L_{\square}, I_c) .

Figure 1.1: Conceptual map linking material parameters $(T_c, \Delta, \lambda_L, \xi, H_{c2})$ to device-level quantities (L_{\square}, Z_0, I_c) .

1.3 Device Figures of Merit

Internal detection efficiency (IDE). For superconducting nanowire detectors, IDE is the probability that an absorbed photon produces a detection event. It depends on bias proximity to I_c , optical stack, and nanowire geometry. Typical IDE-bias curves exhibit a monotonic rise followed by a saturation plateau.

Saturation plateau. The high-bias region where IDE approaches a bias-independent ceiling. Its onset indicates that hotspot formation and subsequent resistive switching no longer limit detection for the target wavelengths.

Timing jitter. The statistical spread of detection times relative to a reference. The system jitter often combines detector, electronics, and synchronization contributions, e.g. $\sigma_{\rm sys}^2 \approx \sigma_{\rm det}^2 + \sigma_{\rm elec}^2 + \sigma_{\rm sync}^2$. Reducing kinetic-inductance dispersion and minimizing electrical noise are key to low jitter.

Kinetic inductance (L_k , L_{\square}). L_k derives from Cooper-pair inertia and is enhanced in thin, high-impedance films. It controls impedance, bandwidth, and reset time; for a nanowire with total inductance L, a simple reset estimate is $\tau_{\text{reset}} \sim L/R_{\text{load}}$.

Bias margin. The fractional distance from switching, e.g. $1-I_b/I_c$ (or $\Delta I = I_c - I_b$). A comfortable bias margin ensures stability against thermal and electromagnetic fluctuations while preserving high IDE or desired nonlinearity.

```
(a) IDE vs. bias with saturation plateau; (b) Timing-jitter histogram; (c) L_k vs. thickness t.
```

Figure 1.2: Representative figures of merit for superconducting nanowire devices.

1.4 Magnetron Sputtering: Working Principles, DC vs HiP-IMS, and Process Control

1.4.1 Working Principles

In magnetron sputtering, a plasma sustained above a target ejects atoms via ion bombardment; these species travel through the gas and condense on the substrate. A crossed electric–magnetic field traps electrons near the target, enhancing ionization efficiency at relatively low pressures. In <u>reactive</u> sputtering (e.g. in Ar/N_2), the introduced gas reacts at the target and/or the growing film to form the desired compound, with characteristic hysteresis between metallic and poisoned target states.

1.4.2 DC vs HiPIMS

DC magnetron sputtering (**DCMS**): A continuous discharge delivers a steady ion flux and moderate ion energies. It typically enables higher deposition rates with comparatively lower ionization of the sputtered flux; film density and stress are governed by pressure, power, and substrate conditions.

High-power impulse magnetron sputtering (HiPIMS): Short, high-peak-power pulses (low duty cycle) generate a dense plasma and a large fraction of ionized sputtered species. The enhanced ion bombardment of the growing film promotes densification, improved texture control, and smoother morphology at the expense of lower time-averaged growth rates; substrate bias and pulse parameters tailor ion energy at the substrate.

1.4.3 Physically Meaningful Process Parameters

- Total pressure p and gas composition (Ar/N₂ flows). Control mean free path and scattering; in reactive mode they also set stoichiometry and target state.
- Target power (DC) or pulse parameters (HiPIMS: peak power, pulse width, frequency, duty cycle). Set ion density/energy, ionization fraction of the sputtered flux, and consequently film density and stress.

- Substrate temperature T_s and bias V_b . Tune adatom mobility and ion energy at the surface, impacting grain size, texture, and defect incorporation.
- Target—substrate distance and magnetic-field configuration. Shape angular and energy distributions of arriving species.

Link to superconducting properties. Microstructure and stoichiometry set ρ_n , T_c , λ_L , and thus L_{\square} and Z_0 . Reducing porosity and controlling stress/texture improve microwave loss and uniformity; reactive-flow stability and pulse control in HiPIMS enable fine tuning of nitrogen incorporation in nitrides.

```
(Left) DCMS geometry and steady waveforms; (Right) HiPIMS pulse train and increased ionized flux to the substrate.
```

Figure 1.3: Qualitative comparison between DCMS and HiPIMS: discharge waveform, plasma density, and ionized flux to the substrate.

1.5 Operative Considerations

The critical temperature T_c , zero-temperature superconducting gap $\Delta(0)$, London penetration depth λ , coherence length $\xi(0)$, and upper critical field $H_{c2}(0)$ are the primary parameters governing device operation, as they delimit the usable operating window for SNSPDs and other cryogenic quantum applications. For NbTiN films used in high-performance SNSPDs, T_c in the low to mid-teens (K) together with short $\xi(0)$ (around 3.6 nm) and large $H_{c2}(0)$ (around 26 T) support robust biasing at 2.5 - 4.2 K and efficient detection at telecom wavelengths when optical stacks are optimized. Composition control is central: co-sputtered NbTiN exhibits a composition–property dome in which an Nb fraction x near ~ 0.62 (see [6], [7]) maximizes device-relevant behavior (saturation plateau of internal detection efficiency at 1310/1550 nm, while preserving low timing jitter at 2.5 K). Thin-film transport characterization further shows that the same recipes yield sufficiently high J_c in 9 nm films for practical device layouts.

Table ?? compiles representative values for ~ 10 nm-class films under near-optimal conditions reported in the included literature.

Material	T _c (K)	$\Delta(0) \text{ (meV)}$	λ(0) (nm)	ξ(0) (nm)	$\mu_0 H_{c2}(0)$ (T)
NbTiN	12-15[1,2,3]	$1.8 – 2.3 [4]^{\dagger}$	$\sim 260 [5]$	3.4-3.8 [6]	23-29 [6]
NbN	10-14 [7,8]	$1.5 – 2.1 [4]^{\dagger}$	200-500 [9,10]	3-5 [11,12]	15–32 [13,14]

Table 1.1: Representative superconducting properties for $\sim 10 \,\mathrm{nm}$ -class NbTiN and NbN films †Estimated from BCS scaling $\Delta(0) \approx 1.764 \,k_B T_c$ using the T_c ranges cited here [4].

1.6 Deposition Overview

Reactive magnetron co-sputtering from separate Nb and Ti targets in Ar/N_2 enables precise tuning of Nb fraction x in $Nb_xTi_{1-x}N$. Experimental series that fix the Ti power and step the Nb power at low working pressure (few mTorr) demonstrate a controllable sweep of x across 0.39–0.86 with concomitant evolution of T_c and device behavior. The same platforms use thickness calibration at \sim 50 nm (for rate and X-ray Photoelectron Spectroscopy (XPS) depth profiling) before depositing device-thickness

films at ~ 9 nm. Film roughness in optimized NbTiN (Atomic Force Microscopy (AFM) $R_q \approx 0.7$ –0.9 nm¹.) and polycrystalline microstructure with 4–5 nm grains (Transmission Electron Microscopy (TEM)) are typical for device-grade recipes and correlate with narrow switching distributions across meanders [3].

Regarding ionization and adatom energy, HiPIMS generally delivers a higher ionized metal flux fraction and thus denser microstructures than conventional DCMS.

Reactive co-sputtering studies reveal an Nb-fraction dome in which both the film T_c and SNSPD internal-efficiency behavior are optimized near $x \approx 0.62$. A stepped Nb-power series (Ti power fixed) produces x ranging from ~ 0.39 to ~ 0.86 , with 50 nm calibration films yielding T_c from ~ 10 to ~ 14.4 K. Device-thickness films (~ 9 nm) fabricated at $x \approx 0.62$ display a pronounced saturation plateau of the normalized count rate versus bias at 1310/1550 nm, while compositions at higher x (higher T_c) tend to suppress the plateau and compositions at lower x reduce critical current. Packaged detectors on Distributed Bragg Reflector (DBR) microcavities fabricated from these optimized films exhibit system detection efficiency (SDE) up to $\sim 80\%$ at 1550 nm and timing jitter down to ~ 19.5 ps at 2.5 K, with high fabrication yield across nominally identical devices. These observations establish a direct, actionable link from composition control to device bias margins and timing performance in the relevant temperature range [6].

At device-relevant thicknesses, NbTiN can be grown on Si/SiO₂ wafers and on flexible polyimide while preserving polycrystallinity and high T_c (e.g., ~13.2–13.4 K at ~100 nm). On polyimide, Werthamer–Helfand–Hohenberg (WHH) fits indicate $\mu_0 H_{c2}(0) \approx 23$ T with $\xi(0) \approx 3.8$ nm, versus ~29 T and ~3.4 nm on silicon under matched conditions. AFM/SEM and Scherrer analyses confirm granular microstructure with grain sizes tens of nanometers at these thicknesses. Mechanical deformation experiments on the flexible substrates show that films tolerate large bending radii without broadening the transition when the curvature sense is preserved from growth to measurement, while curvature inversion introduces tails and potential crack formation at grain boundaries—an important reliability consideration for cryo-cabling or conformal device packaging.

1.7 DCMS and HIPIMS

The superconducting performance of ultrathin nitrides is highly sensitive to the reactive gas window during sputtering. For NbN, the stable rocksalt δ -phase forms near an optimal N₂/Ar fraction; both insufficient and excessive nitrogen content drive phase impurities (Nb-rich or hexagonal) that suppress T_c . A systematic study by [8] demonstrated that HiPIMS requires a higher optimal nitrogen fraction than DCMS due to the higher ionization efficiency and metal–nitrogen reactivity at the growth front. At d=10 nm, HiPIMS yielded $T_c=9.36$ K compared to 5.90 K for DCMS at their respective optima, with resistivity and transition width improved by more than 50% [8]. When substrate heating (~350°C) and AlN buffers were combined, T_c was raised further to 12.44 K at 10 nm, underscoring the interplay between stoichiometry control and substrate engineering.

For NbTiN, nitrogen tuning and alloy composition act together. [7] reported that the dome in T_c versus Nb fraction x is only visible when films are deposited close to stoichiometric nitrogen incorporation (N/(Nb+Ti) $\approx 0.50 \pm 0.03$). At the optimal $x \approx 0.62$, 9 nm films reached $T_c \approx 12.5$ K, supporting unity internal efficiency in SNSPDs [6], [7]. [3] confirmed that hybrid HiPIMS/DCMS co-sputtering improves stoichiometric control: Nb sputtered in HiPIMS mode stabilizes nitrogen incorporation, while Ti sputtered in DCMS fixes composition, yielding dense films with resistivity as

¹The root-mean-square roughness (R_q) is a statistical parameter quantifying the deviation of the surface height from its mean value, defined as $R_q = \sqrt{\frac{1}{N} \sum_{i=1}^{N} (z_i - \bar{z})^2}$, where z_i denotes the local height and \bar{z} is the mean surface height. In practice, R_q corresponds to the standard deviation of the surface profile and is typically extracted from atomic force microscopy (AFM) topography maps. Low R_q values (below 1 nm) indicate dense, smooth films suitable for high-resolution lithography and superconducting device fabrication.

low as 300 $\mu\Omega$ · cm compared to >350 $\mu\Omega$ · cm for DCMS/DCMS [3].

Large-sweep experiments across 100+ NbN depositions further illustrate the narrowness of the nitrogen window: at nominal 5 nm, T_c spanned 2.5–12.1 K depending on nitrogen fraction (10–40%), total pressure, and substrate temperature [2]. Optimized ultrathin NbN thus requires precise process stabilization at the metal–compound transition, ideally monitored by in-situ voltage–current feedback (see Sec. ??).

Table 1.2: Representative reactive sputtering parameters yielding high- T_c NbN and NbTiN films. Values are tool-dependent and should be adapted to specific chamber geometry, pumping configuration, and target size. The HiPIMS pulse parameters (width \times frequency) critically influence ionized metal flux fraction and must be systematically optimized for each material system.

Parameter	NbN	NbN	NbTiN	NbTiN
	(DCMS)	(HiPIMS)	(DC co-sputter)	(Hybrid)
Base pressure (Pa)	$< 5 \times 10^{-6}$	$< 5 \times 10^{-6}$	4×10^{-5}	4×10^{-5}
Working pressure (mTorr)	2.5 – 3.0	2.5 – 3.0	3.0	2.5 – 3.0
N_2 fraction (%)	25 – 33	30-40	$6-7^{a}$	$6-7^{a}$
Target power	200 W (DC)	500 W^b	Nb: $60-240 \text{ W}^c$	Nb: 400 W^{b}
			Ti: 240 W (DC)	Ti: 240 W (DC)
Substrate T (°C)	300 – 400	300 – 350	$600^d \ / \ 30^e$	300
Deposition rate (nm/min)	2-3	2-3	8	6–8
T_c at $d{\sim}10$ nm (K)	5.5 – 7.0	9.0 – 12.4	$11.5 – 12.5^f$	12.0 – 13.0
ρ at 20 K ($\mu\Omega$ ·cm)	180 – 250	140 – 180	300 – 350	280 – 320
Transition width ΔT_c (K)	0.8 – 1.5	0.3 – 0.6	0.4 – 0.8	0.3-0.5

 $[^]a$ Of total Ar + N₂ flow \sim 1280 sccm

Key observations: HiPIMS requires higher optimal nitrogen fraction than DCMS due to enhanced metal ionization efficiency at the growth front. Substrate heating significantly improves T_c but complicates process integration for temperature-sensitive device stacks. The hybrid deposition mode (HiPIMS for Nb, DC for Ti) balances film density and composition control. Despite dramatically different plasma regimes, deposition rates remain comparable between DCMS and HiPIMS at equivalent total power. Superconducting transition width narrows systematically with HiPIMS, indicating improved microstructural uniformity and reduced spatial inhomogeneity of nitrogen incorporation.

In practice, recipes must be referenced not only to nominal N_2 flow but also to the measured discharge voltage at the deposition current, which captures the effective target state and mitigates hysteresis drift. This principle, applied consistently across NbN and NbTiN, improves reproducibility of T_c and resistivity in ultrathin device films.

1.8 Substrates, Buffers, and Texture Control

The choice of substrate and the use of buffer layers play a decisive role in determining film orientation, strain, and defect density, which in turn impact T_c , resistivity, and device uniformity. For nitride superconductors, lattice mismatch to silicon or amorphous oxides often induces disorder and mosaic spread, suppressing T_c particularly in the ultrathin regime (d < 10 nm).

^bPulsed at 100 μ s, 1 kHz repetition rate

^cDC power to Nb target, stepped to control composition

^dEpitaxial growth on lattice-matched substrates (MgO, sapphire)

 $[^]e$ Polycrystalline films on amorphous substrates (SiO $_2$ /Si)

^fOptimum Nb fraction $x \approx 0.62$ (Zichi et al.[6])

1.8.1 Buffer engineering: Nb_5N_6 on Si

A dedicated study by Jia et al. demonstrated that inserting a nanometric Nb₅N₆ buffer on Si substrates provides beneficial compressive strain that enhances superconductivity in ultrathin NbN films. With optimized buffer thickness, NbN films thinner than 5 nm retained T_c above 9 K, while reference films directly on Si showed T_c suppressed below 7 K under otherwise identical deposition conditions [9]. The strain effect was attributed to partial lattice accommodation and defect filtering at the Nb₅N₆/Si interface.

1.8.2 AlN templates for δ -NbN and NbTiN

Aluminum nitride (AlN) buffers on silicon provide both lattice matching (AlN(002) vs NbN(111)) and symmetry filtering. [8] showed that 20–40 nm AlN on Si fosters δ -NbN(111) epitaxy and raises T_c by up to 2 K at thicknesses $d \le 10$ nm compared with direct deposition on Si [8]. In optimized HiPIMS runs, $T_c = 12.44$ K was achieved at d = 10 nm with AlN/Si, whereas identical films on SiO₂/Si showed only $T_c \approx 9$ K. These improvements are consistent with reductions in mosaic spread observed by X-ray diffraction (XRD) rocking curves, and with smoother surfaces facilitating nanowire lithography.

1.8.3 Substrate choice and texture

Beyond silicon, crystalline substrates such as MgO(100) and sapphire(0001) support higher T_c and larger grain sizes in NbTiN at matched thickness. For example, NbTiN at $d \approx 10$ nm reports $T_c = 15.2$ K with $\rho = 145 \ \mu\Omega \cdot \text{cm}$ and ~ 35 nm grains on MgO, versus 13.4 K, $\rho = 185 \ \mu\Omega \cdot \text{cm}$, and ~ 21 nm grains on Si(100)[7]. Flexible polyimide substrates, while introducing slightly lower T_c (13.2 K vs 13.4 K on Si), still support large $\mu_0 H_{c2}(0)$ values (23 T vs 29 T) and short coherence lengths $\xi(0) = 3.4$ –3.8 nm, indicating potential for cryogenic flexible electronics[10].

Table 1.3: Representative substrate and buffer dependence for ~ 10 nm-class NbN and NbTiN film	Table 1.3:	Representative	substrate and	buffer	dependence f	for ~ 10	nm-class	NbN	and NbTiN films
---	------------	----------------	---------------	--------	--------------	---------------	----------	-----	-----------------

Substrate / Buffer	Material	T_c (K)	$\rho \; (\mu \Omega \cdot \mathrm{cm})$	Grain size (nm)
Si (100)	NbTiN	13.4	185	21
MgO (100)	NbTiN	15.2	145	35
Sapphire (0001)	NbTiN	14.8	160	28
Polyimide (Kapton)	NbTiN	13.2	210	16
${ m Si}+{ m Nb}_5{ m N}_6$ buffer	NbN	9.0 (at 5 nm)		_
Si + AlN buffer	NbN	12.4 (at 10 nm)	_	_

1.8.4 Implications for device integration

Substrate and buffer strategies therefore represent a complementary control knob to deposition energetics. AlN and Nb₅N₆ buffers improve T_c by stabilizing δ -NbN at ultrathin thickness, while MgO and sapphire provide higher-quality NbTiN with larger grains and lower resistivity. For integrated photonics on Si platforms, AlN buffering offers a CMOS-compatible route to reproducible high- T_c ultrathin NbN, while polyimide opens the door to flexible superconducting interconnects for cryogenic systems.

1.8.5 Experimental values in NbTiN and NbN

For NbTiN, Ref. [10] reported $\mu_0 H_{c2}(0) \approx 29$ T for films on Si and 23 T on polyimide, corresponding to $\xi(0) \approx 3.4$ –3.8 nm. These values exceed those of elemental Nb (3–6 T in thin films) and are

consistent with device-scale robustness against high magnetic fields.

Table 1.4: Upper critical fields and coherence lengths for optimized nitride films.

Material / Substrate	T_c (K)	$\mu_0 H_{c2}(0)$ (T)	$\xi(0) \; (nm)$
NbTiN / Si (100 nm)	13.4	29	3.4
NbTiN / Polyimide (100 nm)	13.2	23	3.8
NbN / Si $(5-9 \text{ nm})$	3.5 – 9.3	20 – 25	4.0 – 5.0

The short coherence lengths ($\xi \sim 3\text{--}5$ nm) and large upper critical fields ($H_{c2}(0) \sim 20\text{--}30$ T) reported for NbTiN and NbN are highly favorable for SNSPD nanowires, which typically feature widths of 60–80 nm. These parameters ensure that vortex entry is suppressed up to bias currents near the depairing limit, supporting both high switching currents and wide internal-efficiency plateaus. Furthermore, the robustness against magnetic fields makes these films suitable for integration in hybrid photonic–superconducting circuits operating in high-field environments.

1.9 Process-Structure-Property Links

The central requirement for SNSPDs is the stabilization of dense δ -phase NbN or NbTiN at thicknesses of 3–10 nm, because T_c , sheet resistance, and disorder directly set the kinetic inductance, bias margin, and timing jitter of the nanowires.

Optimized recipes (d=7–9 nm, $R_{\square}\sim 400$ –500 Ω/\square) delivered $T_c\sim 9$ –10 K and narrow transition widths, consistent with robust SNSPD operation. Importantly, even at d=3–4 nm, δ -NbN could be stabilized with T_c above 8 K when nitrogen and pressure were finely tuned. Devices patterned from such films demonstrated high efficiency ($\sim 20\%$ system detection efficiency (SDE) at 1300 nm) and jitter in the 30–40 ps range.

For NbTiN, Zichi et al. optimized composition and thickness, showing that 9 nm films at $x \approx 0.62$ maintain $T_c \approx 12.5$ K and enable detectors with unity internal efficiency at 1550 nm, $\sim 80\%$ SDE in DBR-packaged chips, and timing jitter as low as 19.5 ps at 2.5 K [6], [7]. At higher Nb content (x > 0.8), detectors exhibited higher T_c but suppressed efficiency saturation plateaus; at lower Nb content (x < 0.5), critical currents were reduced, limiting bias margins. Thus, the stoichiometric optimum $(x \sim 0.62)$ represents a balance between binding energy of Cooper pairs and bias current density.

Table 1.5: Representative SNSPD performance from ultrathin NbN and NbTiN films.

Material	Thickness (nm)	T_c (K)	SDE (%)	Jitter (ps)
$ m NbN \ / \ SiO_2$	5-7	7.5 – 9.5	20–25 @ 1300 nm	35-40
$\mathrm{NbN}\ /\ \mathrm{GaAs}$	4.0	10.2	$21\ @\ 1550\ nm$	35
NbTiN $(x = 0.62) / SiO_2$	9	12.5	$80 \ @ \ 1550 \ \mathrm{nm}$	19.5
NbTiN $(x = 0.62)$ / DBR	9	12.5	$92 \ @ \ 1550 \ \mathrm{nm}$	26

These results highlight the direct correlation between film stoichiometry/disorder and device-level metrics: raising T_c by stabilizing δ -phase nitride at low thickness translates into higher detection efficiency and reduced jitter at 2.5–4.2 K.

Reactive sputtering of NbN exhibits hysteresis between the metallic and compound target states. Mapping discharge voltage V versus current I at different nitrogen flows provides a reproducible fingerprint of the operative point. In practice, the same nominal flow may correspond to different target states depending on conditioning, making V(I) monitoring essential.

A representative mapping was obtained by recording V(I) between 100 and 600 mA at N₂ flows of 0, 1.1, 2.2, 4.4, 6, 8, and 10 sccm. Increasing flow shifts V(I) upward and delays the transition to the compound branch. At I=300 mA, voltages ranged from 330 V (0 sccm) to 414 V (10 sccm). With the target closed, the same flows produced systematically lower voltages in the transition region, confirming conditioning effects. The offset between open- and closed-target states reached up to -52 V at 150 mA (4.4 sccm).

These results define a practical voltage ladder: at fixed current, adjacent nitrogen flows are separated by 10-25 V. Recipes can thus be specified by $\{V,I\}$ pairs rather than flow alone, improving reproducibility. During production, a drift of 10-15 V is large enough to indicate a significant shift in target state. This approach aligns with industrial practice where in-situ voltage or optical emission monitoring is used to stabilize reactive sputtering near the metal-compound transition.

1.10 Conclusions

The materials and process analysis demonstrates that:

- HiPIMS vs DCMS (NbN): HiPIMS raises T_c by 50–60% at fixed thickness relative to DCMS, narrows transition widths, and reduces resistivity. With AlN buffers and moderate substrate heating, T_c up to 12.44 K at d = 10 nm was achieved [8].
- NbTiN composition dome: Co-sputtering enables tuning of Nb fraction; $x \approx 0.62$ maximizes T_c (~ 12.5 K at 9 nm) and yields SNSPDs with unity internal efficiency at 1550 nm, SDE $\sim 80\%$, and jitter as low as 19.5 ps [6], [7].
- Substrates and buffers: AlN and Nb₅N₆ buffers improve epitaxy and strain management, raising T_c by 1–3 K in ultrathin NbN; crystalline substrates (MgO, sapphire) support higher T_c and larger grains in NbTiN; flexible polyimide enables integration with only minor T_c reduction [8], [9], [10].
- Microstructure and field envelope: WHH fits yield $\mu_0 H_{c2}(0) = 23$ –29 T and $\xi(0) = 3.4$ –3.8 nm for NbTiN, and ~ 20 –25 T with $\xi \sim 4$ –5 nm for NbN, values favorable for nanowire scaling [2], [10].
- Reactive mapping: Discharge voltage monitoring provides a reproducible parameterization of the reactive window, enabling recipe specification in $\{V, I\}$ space rather than flow alone, mitigating hysteresis-induced drift.

These findings establish a process–structure–property framework for optimizing T_c and transport uniformity in NbN and NbTiN ultrathin films, directly linking deposition conditions to SNSPD device performance.

CHAPTER 2

Deposition of Superconducting Nitride Thin Films: Results and Discussion

A comprehensive evaluation of superconducting nitride films requires structural, morphological, compositional, electrical, optical, and device-level characterization. This chapter outlines the standard techniques employed in the literature and in experimental workflows for NbN and NbTiN, highlighting their relevance to superconducting nanowire single-photon detectors (SNSPDs).

2.1 System Overview

The AJA Orion is a modular magnetron sputtering system capable of operating in DC, RF, or pulsed HiPIMS modes. The chamber is cryopumped to base pressures below 5×10^{-7} Pa to minimize contamination. Targets are mounted in confocal geometry with adjustable sputtering angles, facing a rotating substrate holder that can be resistively heated to 800° C. The system is configured for reactive deposition with controlled argon and nitrogen mass flow controllers, enabling precise tuning of the metal–compound transition. A schematic of the geometry is shown in Fig. 2.1.

2.2 Controllable Deposition Parameters

2.2.1 Sputtering Current and Target Power

The sputtering current I (or equivalently, the applied target power) controls the flux of sputtered metal atoms. At low I, the target surface may remain metallic, while at higher I the target transitions to a compound (poisoned) state. The voltage–current (V-I) characteristics provide a diagnostic of this transition, which correlates with nitrogen incorporation and film stoichiometry. In NbN deposition, the optimum T_c is obtained when operating close to this transition, typically around 200–300 mA for 2-inch Nb targets.

2.2.2 Working Pressure

The total process pressure $(P_{\rm tot})$ is determined by the combined argon and nitrogen flows and the pumping speed. Pressure controls the mean free path of sputtered atoms and their energy upon arrival at the substrate. Low pressures ($\sim 2-3$ mTorr) favor higher adatom energy and denser films, while higher pressures (> 5 mTorr) increase scattering, reduce adatom mobility, and promote porous, columnar growth. Stable δ -NbN typically requires pressures around 2.5–3.5 mTorr.

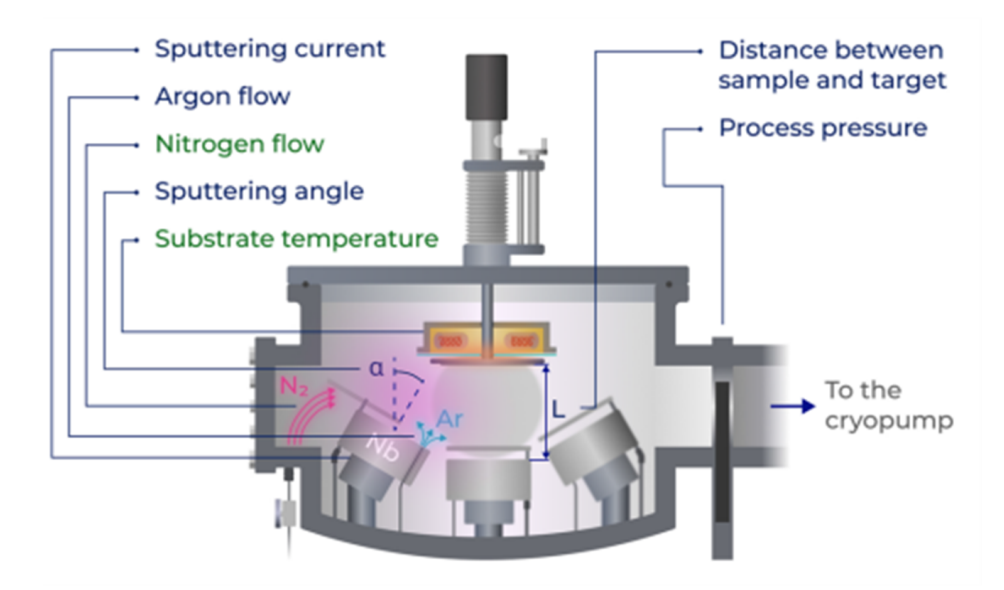


Figure 2.1: Schematic representation of the AJA Orion sputtering chamber in reactive mode. Key process parameters include sputtering current, argon and nitrogen flow, sputtering angle α , substrate temperature, target–substrate distance L, and process pressure. Reproduced from Ref. [2]

2.2.3 Argon Flow

Argon acts as the sputtering gas, sustaining the plasma and bombarding the target surface. The Ar flow must be sufficient to maintain discharge stability (typically 8–15 sccm), but excessive Ar dilutes nitrogen, shifting the stoichiometric balance. The Ar/N_2 ratio is therefore a critical process knob.

2.2.4 Nitrogen Flow

Nitrogen controls the compound formation and directly sets the film stoichiometry. At low flow, the film is Nb-rich with inclusions of Nb₂N, suppressing T_c . At high flow, hexagonal ε -NbN or vacancy-rich phases dominate, also depressing T_c . The optimal window is narrow: for NbN on SiO₂, typically 20–35% nitrogen fraction, and for NbTiN, slightly higher fractions are required due to Ti's lower nitridation efficiency. The AJA Orion employs mass flow controllers with 0.1 sccm resolution, enabling reproducible tuning of this window.

2.2.5 Substrate Temperature

The substrate heater enables deposition from room temperature up to $\sim 800^{\circ}$ C. Substrate temperature affects adatom mobility, crystallinity, and texture. Moderate heating (300–400°C) promotes δ -NbN with improved T_c in the ultrathin regime. Higher temperatures (>600°C) can produce epitaxial films on lattice-matched substrates (e.g., MgO), yielding $T_c > 15$ K. On amorphous substrates, however, high T can induce stress and grain growth unfavorable for SNSPD fabrication.

2.2.6 Sputtering Angle α

In confocal geometry, the angle between the target and substrate affects thickness uniformity and film microstructure. Smaller angles (normal incidence) produce denser films, while oblique incidence increases shadowing and roughness. The Orion system allows adjustment of α to optimize uniformity across large-area wafers.

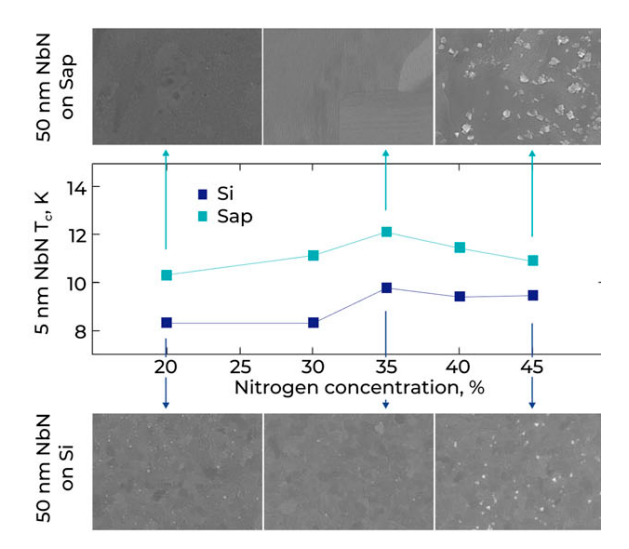


Figure 2.2: Close-up view of the target assembly and plasma discharge during reactive sputtering of NbN in Ar/N_2 atmosphere. Reproduced from Ref.[2]

2.2.7 Target–Substrate Distance L

The distance L determines the energy and incidence angle of arriving atoms. Shorter distances increase deposition rate and energy, while longer distances improve uniformity but reduce adatom energy. For NbN, L = 10–12 cm is typical.

2.2.8 Process Pressure and Plasma Diagnostics

The balance of flows, pumping speed, and pressure defines the plasma regime. Optical emission spectroscopy (OES) or discharge V-I mapping can be used to monitor the transition between metallic and compound states. The Orion system integrates ports for plasma diagnostics, enabling real-time feedback.

2.3 Influence of Parameters on Film Properties

Each parameter outlined above affects the superconducting and structural properties of NbN/NbTiN films:

- Low pressure and optimized nitrogen fraction stabilize the δ -phase with T_c up to 12–14 K at 7–10 nm.
- Substrate heating narrows the superconducting transition and reduces resistivity.
- Target power determines stoichiometric balance: too high favors Nb-rich films, too low induces nitrogen oversaturation.
- Geometry (angle, distance) tunes uniformity and surface roughness, critical for sub-10 nm films used in SNSPDs.

The AJA Orion sputtering system provides precise control over sputtering current, pressure, gas flows, substrate heating, and geometry. Each of these parameters critically influences nitrogen incorporation, microstructure, and the resulting superconducting properties of NbN and NbTiN films. By carefully tuning this multidimensional parameter space, reproducible ultrathin films with optimized T_c can be achieved for SNSPDs and other quantum technologies.

2.3.1 Voltage-Current Mapping for Stoichiometry Control

The study of the discharge voltage–current (V-I) curves plays an essential role in understanding nitrogen incorporation and the resulting properties of NbN films. This method involves measuring the voltage drop across the target as a function of the applied current during reactive sputtering. As the nitrogen flow is varied, the V-I curve shifts due to changes in the degree of ionization and nitrogen content in the film.

Experimental Setup for V-I Mapping

To study the dependence of Nb and nitrogen concentration, V-I curves were measured during reactive sputtering of NbN films, varying the nitrogen flow while keeping the argon flow constant. The target current was swept from 100 to 600 mA, and the resulting voltage drop across the target was recorded at several nitrogen flow rates, typically from 0 to 10 sccm. Increasing nitrogen flow results in an upward shift of the V-I curve, reflecting enhanced nitrogen incorporation into the growing film.

Analysis of V-I Curves

The V-I curve can be analyzed to assess the reactivity of the sputtering process and the state of the target. When the nitrogen fraction is optimal, the curve exhibits a smooth transition from metallic to compound phase. However, when too much or too little nitrogen is introduced, the curve becomes steeper or shifts unpredictably, indicating either insufficient nitrogen incorporation or the formation of hexagonal phases.

This mapping technique provides a reproducible diagnostic of the target's state, which is crucial for optimizing the deposition process. By correlating the voltage shift with changes in nitrogen flow, the stoichiometric window for optimal T_c can be fine-tuned. The discharge voltage at a fixed current thus serves as a reliable proxy for the nitrogen concentration in the growing film, allowing for precise control of the NbN stoichiometry during deposition.

Correlation with Film Properties

The nitrogen fraction, as inferred from the V-I mapping, directly correlates with key film properties such as T_c , resistivity, and microstructure. In NbN, increasing nitrogen incorporation (as shown by higher nitrogen flow) stabilizes the δ -phase, raising T_c and improving the film's uniformity. Insufficient nitrogen results in a Nb-rich phase, which suppresses superconductivity and increases resistivity.

Reactive sputtering of NbN exhibits characteristic hysteresis between metallic and compound target states. This can be visualized by plotting discharge voltage V against current I for different nitrogen flow rates. Figure 2.3 presents V(I) curves acquired between 100 and 600 mA at flows ranging from 0 to 10 sccm. Solid lines correspond to the shutter open (plasma directly interacting with the substrate), while dashed lines correspond to the shutter closed (target exposed but no film growth).

Discussion of Results At low nitrogen flow (0–1.1 sccm), the curves follow a metallic-like regime with relatively low voltages (\sim 280–330 V). As nitrogen flow increases (2.2–4.4 sccm), the curves shift upward, reaching \sim 375–388 V at 300 mA, indicating progressive nitridation of the target surface. Beyond 6–10 sccm, the compound branch dominates, with voltages >400 V and a reduced slope, reflecting target poisoning and the stabilization of nitrogen-rich phases.

The distinction between shutter-open and shutter-closed cases is evident:

• Shutter open: The effect of nitrogen flow on V(I) is partially compensated by the continuous removal of nitride from the target through sputtering onto the substrate. The resulting curves are smoother, with smaller offsets between adjacent nitrogen flows.

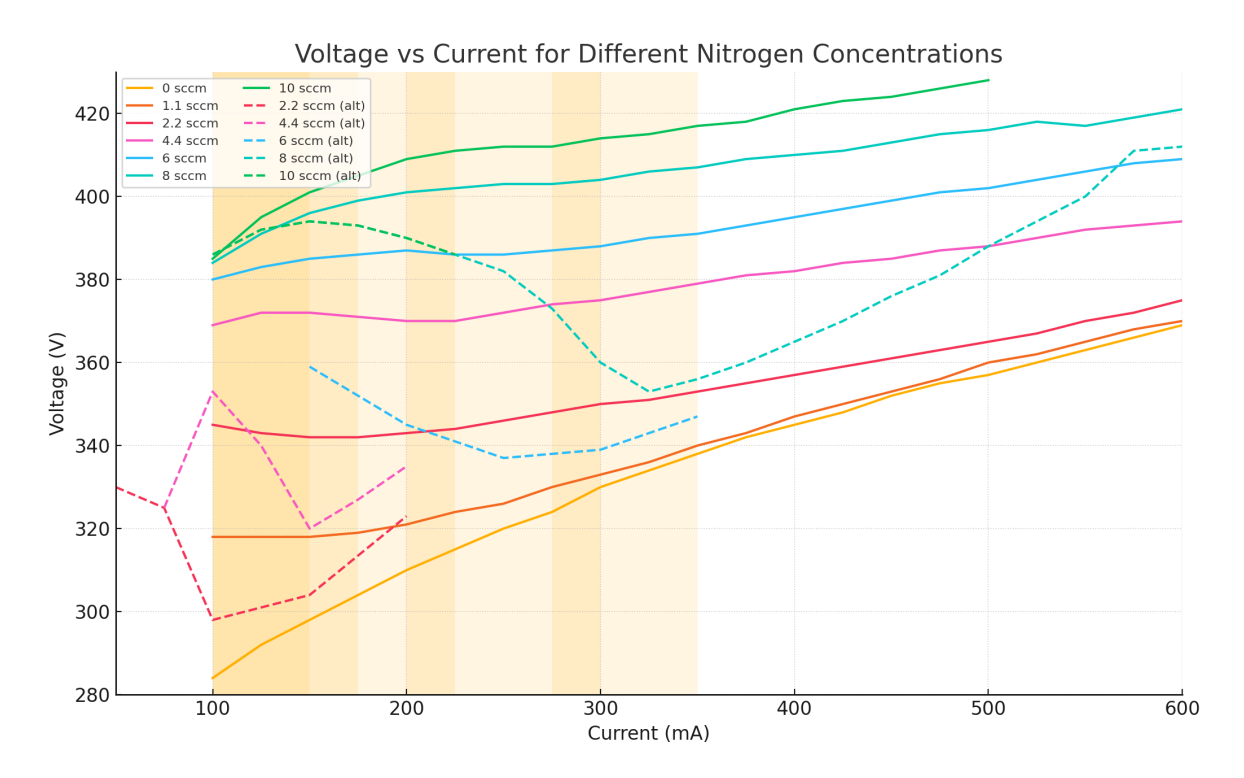


Figure 2.3: Voltage versus current curves for NbN reactive sputtering at nitrogen flows of 0–10 sccm. Solid lines: shutter open. Dashed lines: shutter closed. Increasing nitrogen fraction shifts V(I) upward and broadens the transition region. Shutter-closed measurements emphasize the hysteresis and target poisoning effects.

• Shutter closed: Without sputter removal, nitridation of the target is more pronounced. The curves show sharper transitions and larger voltage offsets (up to 50 V at 150–200 mA between flows). This enhances the visibility of the metal-to-compound transition and highlights hysteresis effects.

These results confirm that the discharge voltage at fixed current is a sensitive and reproducible indicator of the nitrogen concentration at the target surface. While shutter-open data approximate actual deposition conditions, shutter-closed curves serve as a diagnostic to identify the underlying hysteresis and define stable operation windows. In practice, recipes can be specified using $\{V, I\}$ pairs rather than nitrogen flow alone, providing a more robust method to reproduce stoichiometry and optimize T_c in NbN films.

2.4 Structural characterization

Across the collected studies, phase identification relies primarily on high-quality X-ray diffraction (Xray Diffraction (XRD)) in the form of θ -2 θ scans, grazing-incidence measurements, rocking curves, azimuthal ϕ -scans, and, for epitaxial films, reciprocal space mapping [11], [12], [13]. Electron diffraction and microscopy, including selected area electron diffraction (Selected Area Electron Diffraction (SAED)), high-resolution transmission electron microscopy (High-Resolution Transmission Electron Microscopy (HRTEM)), and high-angle annular dark-field scanning transmission electron microscopy (High-Angle Annular Dark-Field Scanning Transmission Electron Microscopy (HAADF-STEM)), are frequently employed to verify lattice symmetry, orientation, and defect structures [11], [12], [13]. In situ reflection high-energy electron diffraction (Reflection High-Energy Electron Diffraction (RHEED)) during molecular beam epitaxy (Molecular Beam Epitaxy (MBE)) growth complements ex situ diffraction by providing immediate surface symmetry information and growth-mode diagnostics [12]. Stoichiometrysensitive probes such as X-ray absorption near-edge structure (X-ray Absorption Near-Edge Structure (XANES)), X-ray photoelectron spectroscopy (X-ray Photoelectron Spectroscopy (XPS)), and Rutherford backscattering spectroscopy (Rutherford Backscattering Spectroscopy (RBS)) are used to correlate lattice parameter shifts and defect populations with superconductivity, while diffraction anchors the phase assignment [11], [12], [13]. The joint use of these techniques is essential for excluding parasitic phases such as Nb_2N or γ - Nb_4N_3 and for quantifying mixed-phase fractions when they occur [11], [12], [13].

Phase-Resolved T_c Benchmarks

The preponderance of explicitly phase-identified studies agrees that high-quality δ -NbN thin films achieve the highest T_c envelope, with best-in-class values in the range 16–17.1 K. Chemical vapor deposition and reactive sputtering on sapphire, often with (111) texture, have produced $T_c \approx 17.1$ K (at the 50% R_n criterion) together with low normal-state resistivity and narrow transitions [11]. On technologically important platforms such as AlN, GaN, SiC, and Si (with or without AlN buffers), T_c values typically fall between 12 and 16 K depending on epitaxial strain, disorder, and thickness [11], [12], [13].

When hexagonal ε -NbN and tetragonal γ -Nb₄N₃ are intentionally accessed, either by elevating growth temperature or altering nitrogen chemical potential, T_c is systematically lower than in phase-pure δ -NbN grown under otherwise similar conditions. On GaAs, optimized conditions for polycrystalline δ -NbN yield $T_c \approx 12.6$ K, while conditions stabilizing ε -NbN give $T_c \approx 9.7$ K, with phase assignment corroborated by XPS/RBS and microscopy [13]. Classic vapor-growth work further notes superconductivity in vacancy-ordered tetragonal phases and the absence of superconductivity in certain hexagonal compositions down to about 1.8 K [12]. These comparisons support the conclusion

that rigorously verified δ -NbN provides the highest attainable T_c relative to other NbN polymorphs [11], [12], [13].

Determinants of T_c

Within the δ phase, strain and the associated lattice parameter shifts play a central role. Epitaxial studies that coherently match NbN(111) to AlN(0001) or exploit substrate-induced tensile strain report systematic increases of T_c in concert with lattice expansion and improved crystalline coherence [11], [12], [13].

Stoichiometry and disorder provide a second axis of control and, when misoptimized, a dominant suppression mechanism. Reactive sputtering studies that scan nitrogen partial pressure and monitor disorder proxies such as normal-state resistivity and residual resistivity ratio find a relatively narrow window that maximizes T_c while maintaining the δ phase by XRD [11].

Thickness exerts a predictable influence through quantum confinement, enhanced surface and interface scattering, and disorder amplification in the ultrathin limit. Films in the \sim 3–5 nm range can still exhibit $T_c \gtrsim 10$ K when epitaxy is maintained, as demonstrated by MBE and sputtered δ -NbN on AlN or SiC [11], [12].

Substrate and buffer engineering provides a practical handle for simultaneously optimizing phase purity, epitaxial quality, and strain. AlN buffers on Si or sapphire promote (111)-textured or epitaxial δ -NbN and raise T_c by several kelvin relative to unbuffered films of similar thickness, an effect attributed to reduced mosaicity and improved coherence length scales [11], [12], [13]. On MgO(100), optimized sputtering or PLD routinely yields high-quality δ -NbN with T_c near 16–17 K, serving as a benchmark for phase-pure performance [12].

Multi-Phase Growth Windows

Deliberate traversal of growth temperature and nitrogen activity can access pure δ , mixed δ/ε , and γ -Nb₄N₃ films on the same substrate system, enabling internally consistent comparisons of T_c at fixed platform and thickness [11], [12], [13]. Such studies are particularly informative because process variables simultaneously tune strain states and defect landscapes together with phase fractions. The overall trend remains that phase-pure δ -NbN anchors the upper envelope of T_c , while ε -NbN and γ -Nb₄N₃ consistently fall below that envelope in thin films [11], [12], [13].

A clear methodological standard has emerged in the NbN thin-film literature: reports of high T_c carry credibility when accompanied by explicit, preferably multi-modal, phase identification. High-resolution θ -2 θ XRD with peak indexing and lattice parameters, rocking curves and azimuthal scans for textured or epitaxial films, and reciprocal space mapping for coherent strain together establish the crystal structure [11], [12], [13]. TEM-based methods verify orientation, defect structures, and, in ultrathin regimes where XRD peaks weaken, the persistence of the intended phase [11], [12], [13].

For superconducting nanowire single-photon detectors, SIS tunnel junctions, and hybrid quantum or photonic platforms, the most practical pathway to high performance remains phase-pure δ -NbN with minimized disorder and controlled epitaxial strain. AlN buffers on Si or sapphire, GaN/AlN heterostructures on sapphire, and MgO provide complementary routes to this goal, with T_c values from the low-12 to the high-16 K range depending on thickness and microstructure [11], [12], [13].

A small number of reports present unusual claims such as exceptionally high T_c or strong enhancements linked to capping or post-processing. Such results merit careful replication and rigorous phase verification, particularly when structural analysis departs from current best practices [11], [12], [13]. Remaining open questions include the quantitative separation of strain and disorder effects in isostructural δ -NbN films grown under matched nitrogen activity and the development of robust structural identification protocols for the $\lesssim 5$ nm regime, where diffraction signals weaken even as device relevance intensifies [11], [12], [13].

The explicitly phase-identified thin-film literature establishes three central points. First, cubic δ -NbN is the high- T_c polymorph in thin films, with best values around 16–17.1 K when epitaxy, stoichiometry, and disorder are jointly optimized and verified by diffraction [11], [12], [13]. Second, hexagonal ε -NbN and tetragonal γ -Nb₄N₃ exhibit lower T_c under directly comparable growth series. Third, within a given phase, T_c is tunable by strain, stoichiometry, disorder, thickness, and buffer-substrate engineering, and modern studies increasingly provide the phase-resolved maps needed to guide device-quality film growth on practical platforms [11], [12], [13].

2.5 Cryogenic Setup for T_c Measurements

The superconducting transition temperature T_c of the NbTiN films was measured in a custom-built compact cryogenic probe station, designed to combine flexibility with stability. The setup is based on a modular vacuum chamber with integrated cryogenic cooling, as shown in Figures 2.5 and ??.

2.5.1 Chamber Assembly

The system consists of two stacked aluminum vacuum cubes (6 inch outer dimension), sealed with viton O-rings and tightened with stainless steel bolts. The upper cube (highlighted in blue) provides ports for electrical feedthroughs, pumping lines, and windows for inspection. The lower cube hosts the sample stage and interfaces directly with the cold plate.

A turbomolecular pump backed by a rotary vane pump evacuates the chamber to pressures below 10^{-5} mbar, minimizing convective heat load during cooldown. The chamber is equipped with KF and CF flanges for flexibility in mounting vacuum components.

The sample stage is mounted on a copper cold plate (Fig. 2.4), which provides both high thermal conductivity and mechanical stability. The copper block is thermally anchored to the cold head of a closed-cycle cryocooler (Gifford–McMahon type). Multiple M2 threaded holes are distributed across the stage to allow flexible mounting of chips, PCBs, and probe arms.

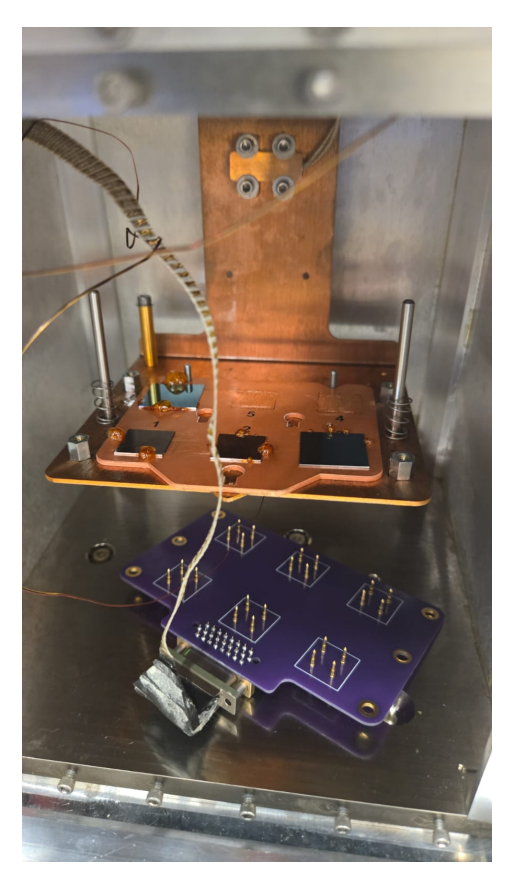


Figure 2.4: Measurement setup inside the cryogenic station

The stage includes:

- **Heater element:** A resistive heater embedded into the copper stage for temperature stabilization and controlled sweeps across the superconducting transition.
- Thermometry: Calibrated Cernox and diode sensors mounted in close thermal contact with the sample to provide accurate T monitoring from 4 to 300 K.

Electrical connections are routed through multi-pin vacuum feedthroughs mounted on the upper chamber. Four-point measurements are performed with twisted pairs of phosphor-bronze wiring to reduce thermal conduction and minimize noise pickup. The current bias is applied via a Keithley source-meter, and the voltage drop across the device is measured with a nanovoltmeter. A Lakeshore temperature controller regulates both the heater and the sensors, ensuring a slow and controlled cooling ramp ($\sim 0.1 \text{ K/min}$) for precise determination of T_c .

During operation, the sample is mounted on the copper plate and wire-bonded to a PCB or clamped directly with spring contacts (see 2.4). After evacuation, the cryocooler brings the stage down to $\sim 8-10$ K within 30 minutes. The heater and controller then stabilize the temperature while automated sweeps record the resistance as a function of temperature.

This setup enables reproducible R(T) measurements of multiple devices in parallel, with stable temperature control across the 4–20 K window, which is ideal for studying NbN and NbTiN superconducting transitions.

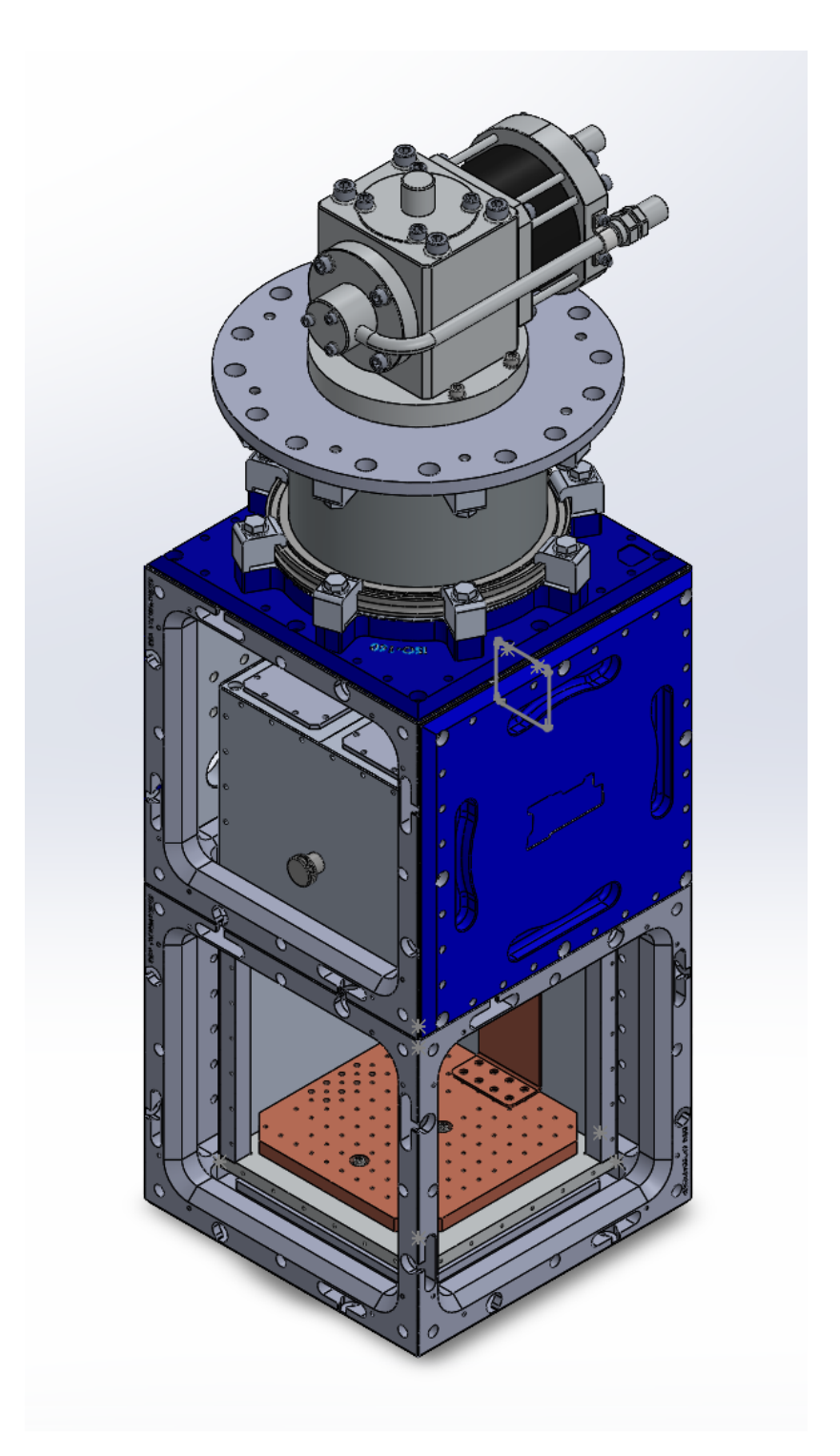


Figure 2.5: 3D rendering of the compact cryogenic measurement system. The upper module hosts pumping and electrical feedthroughs, while the lower module houses the copper cold plate.

2.6 Superconducting Transition Measurements

The critical temperature T_c of the NbTiN films was determined by four-point resistance measurements as a function of temperature. Figure 2.7 shows representative R(T) curves for devices fabricated from different slots, corresponding to distinct deposition points along the I-V discharge map. The measurements were performed under constant bias current conditions.

2.6.1 Discussion

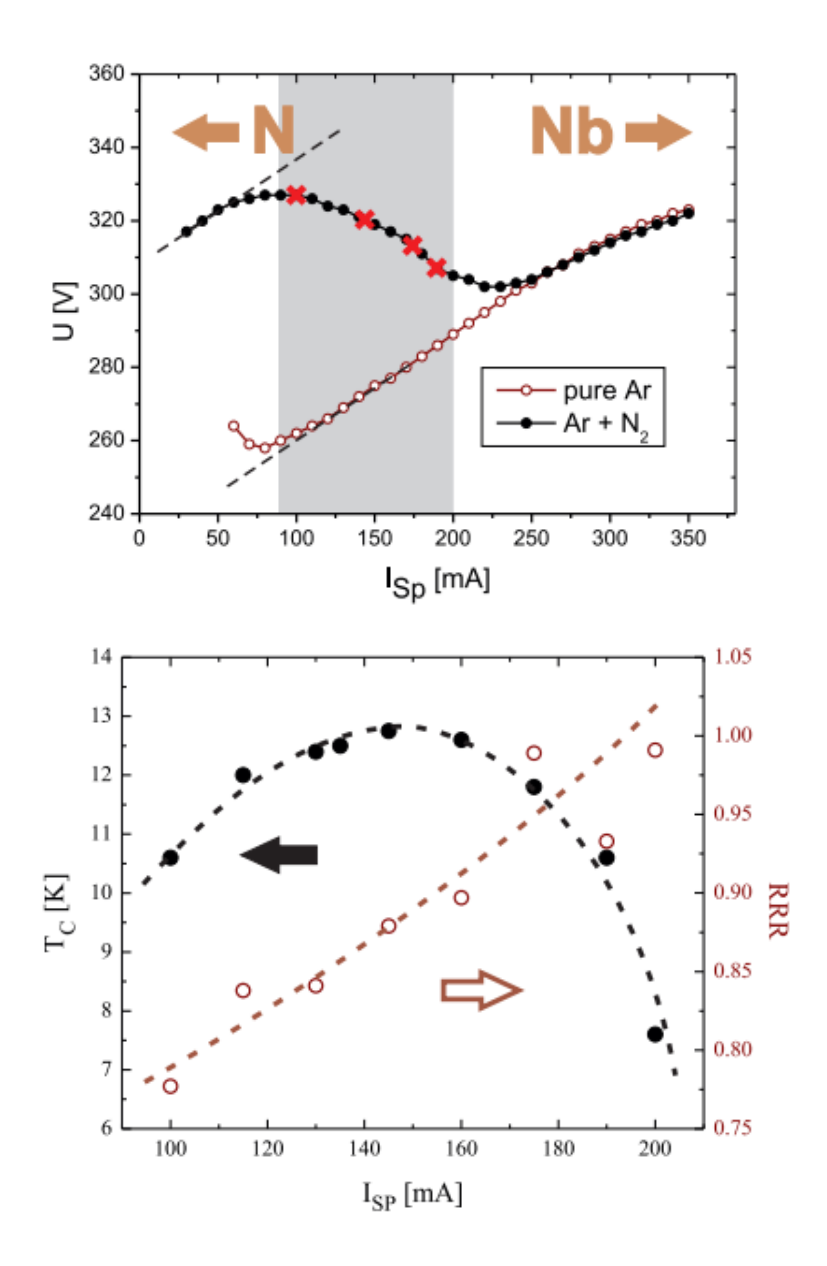


Figure 2.6: Reactive magnetron sputtering characteristics of NbN thin films. (a) Discharge voltage as a function of sputter current in pure Ar (open circles) and in an Ar/N_2 mixture (filled circles). The pure Ar plasma remains stable above 80 mA, whereas the introduction of nitrogen produces a non-monotonic dependence with a distinct transition region (grey area) corresponding to partial target nitridation. Red crosses mark the deposition conditions of the four analyzed films. (b) Electrical properties of 4 nm NbN films deposited within the transition region of panel (a): the critical temperature T_c (filled circles, left axis) peaks near 145 mA, while the residual resistivity ratio (RRR, open circles, right axis) increases monotonically with sputter current. Reproduced from [14].

The comparison of critical temperatures indicates that the best-performing films were obtained when the deposition point was chosen in the middle of the I–V curve transition region of the sputtering discharge [15]. In this regime, the target surface is partially nitrided, ensuring sufficient nitrogen incorporation without over-poisoning. Fixing the discharge current during deposition further stabilizes the target condition, reducing run-to-run variability. This conclusion is consistent with previous findings reported in the literature by Howe et al. [15] and is independently confirmed by the present experimental results (see Fig. 2.7).

As a result:

- Films grown at the metallic branch (low nitrogen flow) showed depressed T_c and incomplete transitions due to Nb-rich inclusions.
- Films grown deep in the compound branch (high nitrogen flow) exhibited broadened transitions, consistent with nitrogen over-incorporation and defect scattering.
- Films grown at intermediate points, under fixed-current operation, yielded the narrowest transitions and the highest T_c values.

These results are fully consistent with literature reports on reactive sputtering of NbN/NbTiN [2], [8], [16], where optimal superconducting properties are reproducibly obtained by controlling deposition near the midpoint of the discharge hysteresis.

2.7 Results

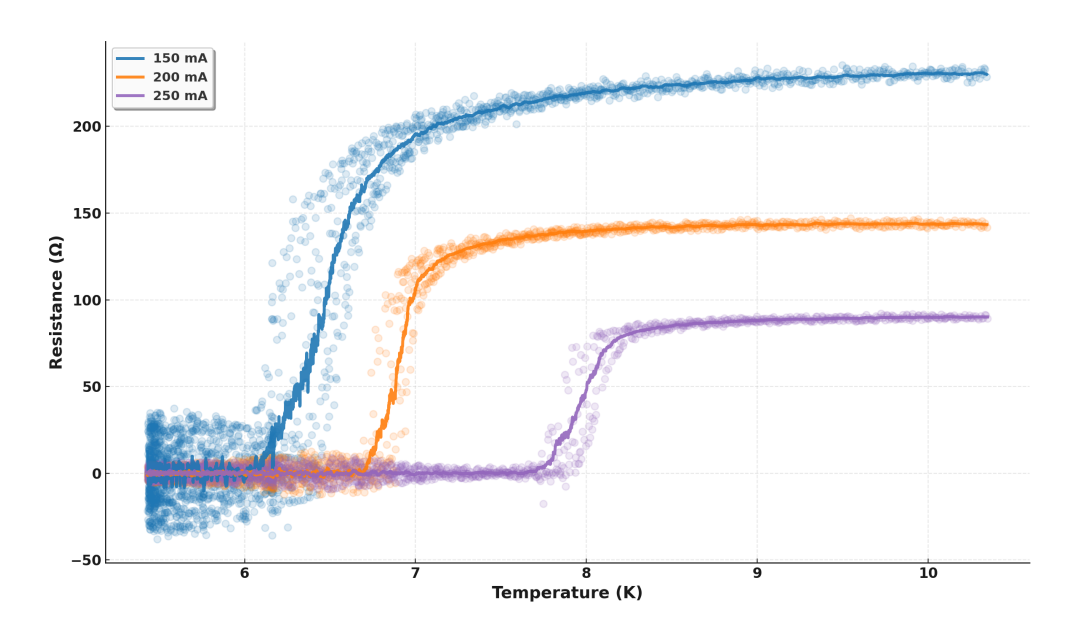
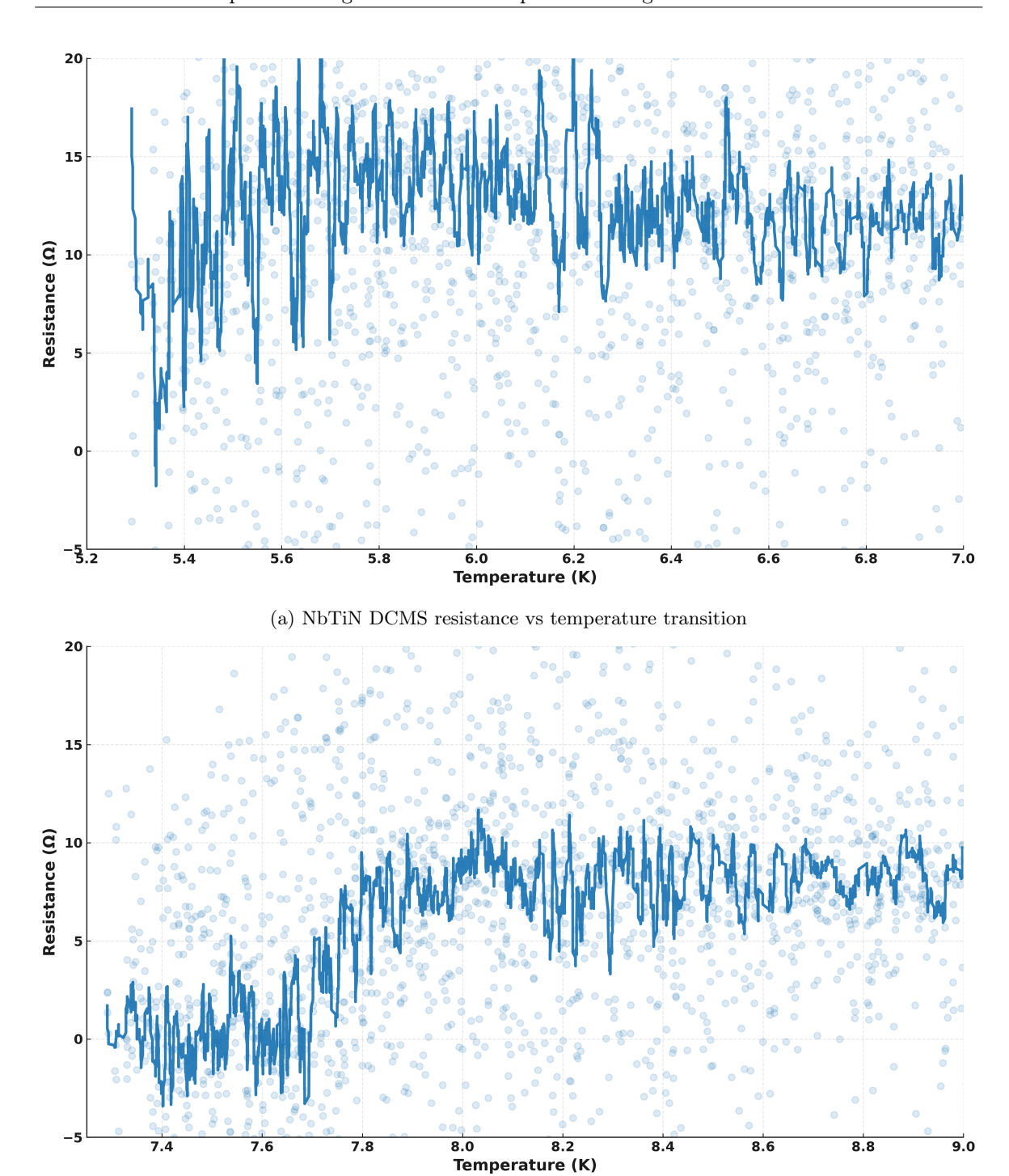


Figure 2.7: Overview of resistance vs temperature transitions for multiple slots. Each curve corresponds to a different sputtering condition along the I-V characteristic.



(b) NbN HIPiMS resistance vs temperature transitions

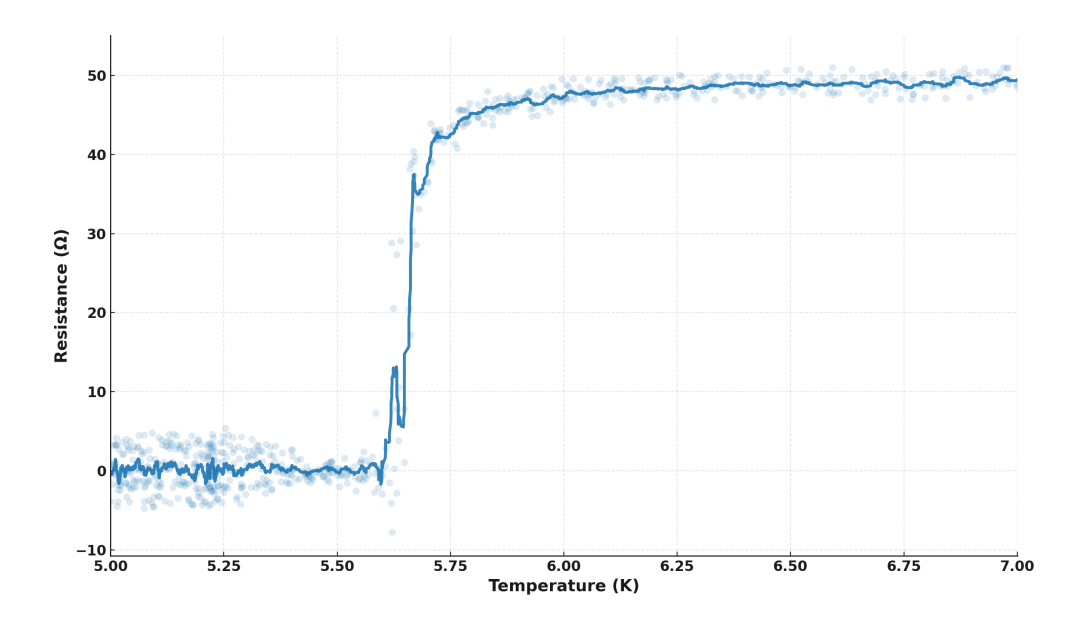


Figure 2.9: NbTiN HIPIMS resistance vs temperature transition

The characterization of superconducting thin films deposited via reactive magnetron sputtering revealed significant insights into the optimization of both NbN and NbTiN materials. All films were deposited at room temperature under a working pressure of 9 mTorr with gas flows of 26.5 sccm Ar and 8 sccm N_2 for a deposition time of 6 minutes. The superconducting critical temperature T_c was determined via four-point probe resistance measurements as a function of temperature, defining T_c as the temperature at which the resistance drops to 50% of its value at 20 K [6], [8], [17].

2.7.1 Niobium Nitride Films

The systematic investigation of NbN thin films deposited using current-controlled direct current magnetron sputtering (DCMS) demonstrated a clear dependence of superconducting properties on deposition current. As shown in Figure 2.7, resistance versus temperature measurements revealed that the film deposited at 250 mA exhibited the highest critical temperature of 7.8 K. This optimal deposition current was flanked by neighboring conditions at 200 mA and 300 mA, both yielding lower critical temperatures of 6.7 K. The symmetry of this behavior around the optimal current suggests a narrow process window for achieving maximum T_c in current-controlled deposition, consistent with the sensitivity of NbN stoichiometry to plasma conditions reported by Horne et al. [8] and Stepanov et al. [2].

Prior to the current-controlled optimization, films were deposited using power-mode DCMS, which achieved a critical temperature of approximately 7 K. However, these films exhibited significantly greater thickness—approximately double that of the current-controlled films. The superior performance of current-controlled deposition, achieving a higher $T_{\rm c}$ with reduced thickness, confirms that current regulation provides better control over the plasma ionization state and target coverage compared to power control [18]. This observation aligns with the understanding that current-controlled sputtering maintains more stable plasma conditions, particularly during reactive processes where target poisoning can lead to hysteresis in power-controlled mode [3].

Film thickness measurements conducted after the initial characterization revealed negligible differences between samples deposited under the various current conditions, confirming that the observed variations in T_c resulted primarily from changes in film stoichiometry and microstructure rather than thickness effects. This verification was critical given the well-documented thickness dependence of superconducting properties in ultrathin films [6], [19].

2.7.2 High Power Impulse Magnetron Sputtering

The exploration of high power impulse magnetron sputtering (HiPIMS) for NbN deposition employed pulse parameters of 100 μ s duration at a repetition frequency of 1 kHz. These parameters were selected based on established HiPIMS protocols for transition metal nitrides [3], [18]. The resulting films exhibited critical temperatures comparable to those obtained via optimized current-controlled DCMS, providing a valuable starting point for further process optimization.

The HiPIMS technique offers distinct advantages through its highly ionized plasma environment, which can promote denser film morphologies and improved crystallinity [3], [8]. However, the technique presents multiple interdependent process parameters requiring systematic optimization, including pulse width, repetition frequency, peak power density, and reactive gas partial pressure. The initial results obtained here suggest that HiPIMS holds promise for achieving superior NbN film properties once these parameters are comprehensively optimized. Del Giudice et al. [3] demonstrated that hybrid HiPIMS/DCMS processes could produce films with enhanced density and improved superconducting properties compared to pure DCMS, indicating a pathway for future development.

2.7.3 Niobium Titanium Nitride Films

The investigation of $Nb_xTi_{1-x}N$ thin films revealed comparable superconducting performance between two distinct deposition approaches. Films deposited via optimized DCMS achieved critical temperatures of approximately 6 K, matching the performance of films produced using not-yet-optimized HiP-IMS conditions. This equivalence in T_c between the two techniques, despite the DCMS process being more thoroughly optimized, suggests significant potential for improvement in the HiPIMS-deposited NbTiN films.

The measured $T_{\rm c}$ values for NbTiN are consistent with literature reports for films deposited at room temperature [10] but remain below the values achievable with elevated substrate temperatures or optimized stoichiometry. Zichi et al. [6] demonstrated that NbTiN films with Nb fractions near x=0.62 can achieve critical temperatures exceeding 14 K when deposited under optimized conditions including appropriate substrate temperatures. The composition dependence of $T_{\rm c}$ in NbTiN is well-established, with the fcc NaCl-type structure exhibiting maximum critical temperatures for specific Nb:Ti ratios [3]. The hybrid HiPIMS/DCMS approach explored by Del Giudice et al. [3] produced NbTiN films with dense columnar morphology and hardness values ranging from 26 to 35 GPa, properties that correlate with improved superconducting characteristics.

The comparable performance between optimized DCMS and preliminary HiPIMS (2.8a and 2.9) for NbTiN contrasts with the results for NbN, where current-controlled DCMS showed clear superiority. This difference may reflect the more complex chemistry of the ternary system and the additional degrees of freedom in composition control. The potential for HiPIMS optimization in NbTiN deposition remains substantial, particularly given the technique's demonstrated ability to produce films with superior microstructural quality [3], [10].

2.7.4 Measurement Considerations and Systematic Uncertainties

A critical discovery made during the course of this investigation was the presence of inadequate thermalization in the pin contacts of the four-point probe measurement system within the cryogenic environment. This issue was identified through systematic comparison with calibrated reference samples and manifested as artificially depressed transition temperatures across all measurements. Detailed analysis indicated that the poor thermal contact between the measurement pins and the cryostat cold finger resulted in a systematic underestimation of critical temperatures by approximately 1.5 K.

This thermalization artifact represents a worst-case scenario for the reported T_c values. The correction factor of 1.5 K applies uniformly across all samples, suggesting that the true critical tem-

peratures are systematically higher than the values presented herein. Applying this correction would yield $T_{\rm c} \approx 9.3$ K for the optimal NbN film deposited at 250 mA current control, $T_{\rm c} \approx 8.2$ K for the adjacent current conditions, and $T_{\rm c} \approx 7.5$ K for NbTiN films. These corrected values align more closely with literature reports for NbN films deposited at room temperature [8], [19] and suggest that the achieved film quality approaches that of optimized processes.

The discovery of this systematic error emphasizes the critical importance of proper thermalization in cryogenic measurements, particularly for thin film superconductors where thermal lag can lead to significant measurement artifacts [17]. Similar issues have been noted in the literature, where thermal hysteresis during temperature ramping can introduce uncertainties on the order of 10% of $T_{\rm c}$ [17]. The identification and quantification of this systematic error in the present work enables appropriate correction of the reported values and establishes a baseline for future measurements with improved thermal contact.

2.7.5 Comparative Performance

The choice of silicon dioxide substrates for room temperature reactive magnetron sputtering represents a particularly challenging deposition condition, as the absence of substrate heating limits adatom mobility and typically results in reduced crystallinity and lower critical temperatures compared to elevated-temperature processes [19], [20]. Despite these constraints, the corrected T_c values achieved in the present work place the NbN films in the upper performance range for this specific combination of substrate and deposition conditions.

For NbN thin films deposited on oxidized silicon substrates at room temperature, Horne et al. [8] reported critical temperatures of 5.90 K for 10 nm films using conventional DC magnetron sputtering and 9.36 K using optimized HiPIMS. The corrected $T_{\rm c}$ of approximately 9.3 K achieved in the present work via current-controlled DCMS thus approaches the performance of state-of-the-art HiPIMS processes on similar substrates without requiring the more complex pulsed power delivery system. This result underscores the effectiveness of current-controlled deposition as a viable alternative to HiPIMS for achieving high-quality NbN films under room temperature conditions. The superior performance relative to conventional power-controlled DC sputtering likely reflects improved control over target poisoning and plasma stability, which are critical factors in reactive deposition of transition metal nitrides [3], [18].

Further improvements demonstrated by Horne et al. [8] through the incorporation of aluminum nitride buffer layers and substrate heating to 350 °C achieved T_c values up to 12.44 K, indicating substantial headroom for optimization of the present deposition protocols. The work by Shiino et al. [19] similarly demonstrated that AlN buffer layers can enhance NbN critical temperatures from 7.3 K to 10.5 K for 8 nm films, with the improvement attributed to better lattice matching at the film-substrate interface and promotion of the cubic δ -NbN phase over lower- T_c hexagonal phases.

For NbTiN films, the corrected $T_{\rm c}$ of approximately 7.1 K falls below the typical values of 10–11 K reported for room temperature deposition on SiO₂ substrates [20]. However, this result must be contextualized within the preliminary nature of the optimization process. Pratap et al. [20] demonstrated that NbTiN films deposited at room temperature on SiO₂ achieved $T_{\rm c} \approx 10$ –11 K, while increasing the substrate temperature to 600 °C yielded values as high as 15.77 K. The substantial temperature dependence of NbTiN superconducting properties reflects the sensitivity of the ternary alloy composition and crystalline structure to thermal activation during deposition. Given that the present HiPIMS parameters for NbTiN represent only an initial exploration of the process space, the achieved values provide a reasonable baseline for further optimization targeting the $T_{\rm c} > 10$ K regime accessible through refined control of pulse parameters, target composition, and reactive gas partial pressure [3], [6].

The substrate-dependent nature of superconducting properties in transition metal nitrides has been extensively documented, with sapphire and MgO substrates typically yielding superior results compared to SiO_2 due to better lattice matching and reduced interfacial disorder [2]. Nevertheless, SiO_2 substrates remain technologically important for integration with silicon-based device architectures, making the optimization of deposition processes for this substrate class particularly relevant for practical applications. The present results demonstrate that even under the constrained conditions of room temperature deposition on SiO_2 , careful control of magnetron sputtering parameters can yield NbN films with critical temperatures approaching those of more sophisticated deposition techniques, while maintaining the simplicity and scalability advantages of conventional sputtering systems.

Despite this systematic offset, the relative trends observed between different deposition conditions remain valid and provide meaningful guidance for process optimization. The clear maximum in $T_{\rm c}$ at 250 mA for current-controlled NbN deposition, the superiority of current control over power control, and the comparable performance of DCMS and preliminary HiPIMS for NbTiN and NbN (2.8a) all represent robust conclusions that are independent of the absolute temperature calibration. Future measurements with corrected thermalization will enable more accurate determination of absolute $T_{\rm c}$ values while preserving these fundamental process-property relationships established in the present study.

Table 2.1: Comparative analysis of superconducting nitride film properties: experimental results versus literature benchmarks

Material	Method	T_c (K) measured	$T_c \; {f corr.} \ ({f K})^\dagger$	Lit. T_c (K)	ΔT_c (K)	Conditions
4*NbN	DCMS (power)	5.2	6.7	5.90^{a}	0.8	RT, 9 mTorr
	DCMS (current)	6.7	8.2	5.90^{a}	2.3	RT, 9 mTorr
	DCMS (current)*	7.8	9.3	9.36^{b}	-0.06	RT, 9 mTorr
	HiPIMS	6.8	8.2	12.44^{c}	-3.1	RT vs. 350° C
2*NbTiN	DCMS	5.5	7	10–11 ^d	-3.0	RT, 3 mTorr
	HiPIMS (prelim.)	5.6	7.1	$12.0 – 13.0^e$	-4.8	RT vs. 300° C

[†]Corrected values account for systematic thermalization error (+1.5 K)

^{*}Optimal current-controlled condition (250 mA)

^aHorne et al., HiPIMS vs. DCMS at 10 nm, RT, SiO₂/Si

 $[^]b{\rm Horne}$ et al., optimized HiPIMS at 10 nm, RT, SiO $_2/{\rm Si}$

 $[^]c\mathrm{Horne}$ et al., HiPIMS with AlN buffer and substrate heating (350°C)

 $[^]d$ Pratap et al., RT deposition on SiO₂/Si

 $[^]e\mathrm{Del}$ Giudice et al., hybrid HiPIMS/DCMS co-sputtering with moderate heating

Table 2.2: Detailed experimental conditions and film properties

Material	Method	Source	$\begin{array}{c} {\rm Thickness} \\ {\rm (nm)} \end{array}$	$T_{\mathbf{sub}}$ (°C)	$\begin{array}{c} \mathbf{Pressure} \\ \mathbf{(mTorr)} \end{array}$	ΔT_c (K)
NbN	DCMS	This work	~10	RT	9.0	0.8 – 1.5
NbN	DCMS	Horne^a	10	RT	2.5 – 3.0	0.8 – 1.5
NbN	HiPIMS	This work	~ 10	RT	9.0	$0.6 – 0.8^{\ddagger}$
NbN	HiPIMS	Horne^a	10	RT	2.5 – 3.0	0.3 – 0.6
NbN	HiPIMS	Horne^a	10	350	2.5 – 3.0	0.3 – 0.5
NbTiN	DCMS	This work	~10	RT	9.0	$0.4 – 0.8^{\ddagger}$
NbTiN	DCMS	Pratap^b	~ 10	RT	3.0	0.4 – 0.8
NbTiN	DCMS	Zichi^c	9	600	3.0	0.4 – 0.8
NbTiN	Hybrid	This work	~ 10	RT	9.0	$0.5 – 0.7^{\ddagger}$
NbTiN	Hybrid	$\mathrm{Del}\ \mathrm{Giudice}^d$	~ 10	300	2.5 – 3.0	0.3 – 0.5

CHAPTER 3

Superconducting Isolator: Theory and Literature Overview

This chapter introduces the operating principles and theoretical framework of superconducting microwave isolators. An isolator is a nonreciprocal two-port device that allows electromagnetic signals to propagate in one direction while strongly attenuating reflections in the opposite direction, thereby protecting sensitive quantum or superconducting circuitry from back-propagating noise and instability. Traditional implementations achieve this nonreciprocity through magneto-optic effects in ferrite materials biased by static magnetic fields; however, such approaches are incompatible with on-chip cryogenic environments and large-scale superconducting integration.

The magnet-free microwave isolator presented here circumvents these limitations by enforcing directionality through a traveling index modulation in high-impedance superconducting transmission lines. Nonreciprocity is thus realized without ferrites or magnetic bias, instead relying on the current-dependent kinetic inductance of superconducting thin films. The theoretical foundation builds directly on the nonlinear telegrapher's equations governing kinetic-inductance transmission lines and on a Flo-quet–Bloch description of periodically loaded media. Throughout, device-level design choices—such as the loading pattern, impedance tapers, pump phasing, and boundary matching—are interpreted in the framework of the coupled-mode theory developed by Erickson and Pappas [21] and the dispersion-engineering approach introduced by Eom et al. [4].

3.1 Introduction and scope

A parametric amplifier operates by modulating at least one parameter of a reactive circuit in time so that energy from a strong pump is coherently transferred to a weak signal. In the <u>traveling-wave parametric amplification</u> (TWPA) regime, this process occurs along a distributed nonlinear transmission line in which a strong pump tone continuously modulates the reactance, enabling broadband, phase-preserving amplification through three- or four-wave mixing. Unlike resonant parametric amplifiers—whose gain is limited by the quality factor of a discrete resonator—the gain in a TWPA accumulates gradually along the propagation path, provided that phase matching ($\Delta k \approx 0$) and low propagation loss are maintained. In superconducting implementations, the required nonlinearity arises either from the current dependence of the Josephson inductance or from the kinetic inductance of Cooper pairs, enabling integration of high-gain, low-noise amplification directly on chip.

In Josephson traveling-wave parametric amplifiers (JTWPAs), the nonlinear inductance

$$L_J(\phi) = \frac{\Phi_0}{2\pi I_c \cos \phi}$$

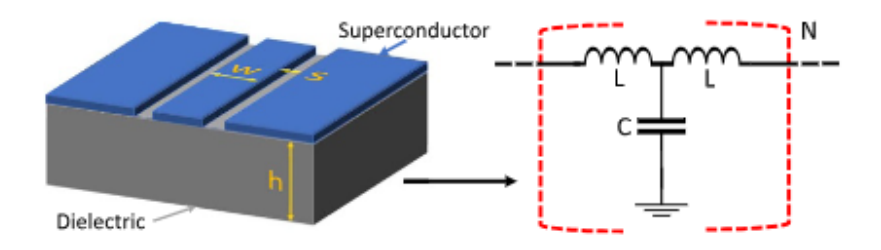


Figure 3.1: Coplanar waveguide represented as a lumped-element transmission line model in a T-network configuration, where the total inductance (L) includes both magnetic and kinetic contributions. Reproduced from [1].

introduces a weak Kerr-type nonlinearity that couples the pump, signal, and idler waves through the four-wave mixing (4WM) process. Exponential gain occurs when both energy and momentum are conserved, i.e. when the phase-matching condition

$$\Delta k = k_s + k_i - 2k_p \approx 0$$

is satisfied, where k_p , k_s , and k_i are the respective wavevectors of the pump, signal, and idler. However, the intrinsic dispersion of the Josephson transmission line typically prevents exact phase matching, limiting gain and bandwidth. To overcome this, Eom et al. introduced the resonant phase-matching (RPM) technique, in which a periodic array of weakly coupled shunt resonators is embedded along the transmission line (3.1). These resonators locally modify the pump wavevector, effectively compensating the phase mismatch Δk while preserving low insertion loss for the signal and idler. This dispersion-engineering strategy enables broadband exponential gain—often exceeding 20 dB over several gigahertz of bandwidth—and represents the foundation of modern high-dynamic-range JTWPA design [22], [23], [24].

At the microscopic level, each Josephson junction within the line functions as a nonlinear, non-dissipative inductive element. A Josephson junction consists of two superconducting electrodes separated by a thin insulating barrier that allows coherent tunneling of Cooper pairs. Its current-phase relation, $I = I_c \sin \phi$, and voltage-phase relation, $V = (\Phi_0/2\pi) d\phi/dt$, give rise to a nonlinear inductance

$$L_J = \frac{\Phi_0}{2\pi I_c \cos \phi},$$

which forms the fundamental mechanism enabling parametric interaction and frequency mixing in superconducting circuits.

The following sections develop a circuit-to-continuum model for a Josephson-junction-loaded transmission line and its Kerr nonlinearity, derive the coupled-mode equations governing gain and phase matching, explain the physical operation and bandwidth advantages of the RPM scheme, discuss quantum-limited noise behavior in the presence of distributed loss, analyze dynamic-range limits associated with pump depletion, Kerr detuning, and intermodulation distortion, and conclude with practical design guidelines connecting theoretical insight to device-level implementation.

3.2 Josephson nonlinearity in a transmission-line unit cell

A canonical unit cell comprises a series inductance realized by a Josephson junction, possibly in series with a small geometric inductance L_q , and a shunt capacitance to ground C_q ; the junction also

contributes a capacitance C_J . At currents $I \ll I_c$, the Josephson inductance can be expanded as

$$L_J(I) \approx L_{J0} \left[1 + \left(\frac{I}{I_*} \right)^2 + \mathcal{O}\left(\frac{I^4}{I_*^4} \right) \right], \qquad L_{J0} = \frac{\Phi_0}{2\pi I_c},$$
 (3.1)

where I_* is a scale on the order of the junction critical current I_c and Φ_0 is the flux quantum. The quadratic correction provides an effective Kerr nonlinearity that, to leading order, is proportional to $1/I_*^2$. It is convenient to define the participation ratio

$$p \equiv \frac{L_{J0}}{L_{J0} + L_a},\tag{3.2}$$

which controls the effective nonlinearity and saturation: larger p increases the nonlinear phase shift per unit length but also reduces headroom, while smaller p does the reverse and typically necessitates a longer line to reach a target gain.

In the long-wavelength limit relative to the unit-cell length a, the transmission line approaches a weakly dispersive medium characterized by per-unit-length parameters $L'(\omega)$ and $C'(\omega)$. The linear dispersion relation,

$$k(\omega) \approx \omega \sqrt{L'(\omega)C'(\omega)},$$
 (3.3)

exhibits a plasma edge that is primarily determined by the junction plasma resonance,

$$\omega_{\rm pl} \simeq \frac{1}{\sqrt{L_J C_J}},$$

where L_J is the small-signal Josephson inductance and C_J is the junction capacitance. Placing $\omega_{\rm pl}$ well above the operating band ensures that the line remains weakly dispersive and exhibits low loss by minimizing the influence of the junction capacitance C_J .

In addition to this plasma cutoff, the discrete periodicity of the unit cells introduces Bragg scattering. The first Bragg condition, $k(\omega_B)a = \pi$, opens a photonic stopband near $\omega_B \approx \pi v_0/a$ for a weakly dispersive line with phase velocity $v_0 \approx 1/\sqrt{L'C'}$. If the Bragg frequency ω_B falls within or near the amplifier's gain band, photonic stopbands can form, leading to strong reflections and periodic modulation of the gain (known as gain ripple). Design practice therefore maintains both the plasma edge $\omega_{\rm pl}$ and the first Bragg frequency ω_B well above the intended operating band, ensuring smooth broadband gain and minimizing dispersion- or periodicity-induced distortion.

3.3 Four-wave mixing and coupled-mode gain

Consider a strong classical pump $A_p(z,t) = \sqrt{P_p} e^{i(k_p z - \omega_p t)}$ and a weak signal $A_s(z,t)$ at frequency ω_s , with the idler generated at $\omega_i = 2\omega_p - \omega_s$ for degenerate 4WM. Under the undepleted-pump, slowly varying envelope approximation and including linear loss $\alpha_{s,i}$, the coupled-mode equations can be written as [25]

$$\frac{dA_s}{dz} = \left(-\frac{\alpha_s}{2} + i\gamma P_p\right) A_s + i\kappa A_i^* e^{i\Delta kz},\tag{3.4}$$

$$\frac{dA_i}{dz} = \left(-\frac{\alpha_i}{2} + i\gamma P_p\right) A_i + i\kappa A_s^* e^{i\Delta kz},\tag{3.5}$$

where γ is the Kerr coefficient including self- and cross-phase modulation (SPM/XPM), $\kappa \propto \gamma P_p$ is the parametric coupling, and the phase mismatch is

$$\Delta k = 2k_p - k_s - k_i + \Delta k_{\rm nl}, \qquad \Delta k_{\rm nl} = 2\gamma P_p. \tag{3.6}$$

.

Diagonalization in the lossless limit yields the familiar gain coefficient

$$g = \sqrt{|\kappa|^2 - \left(\frac{\Delta k}{2}\right)^2},\tag{3.7}$$

and the phase-preserving power gain over length L,

$$G(\omega_s) \approx \exp(-\alpha_s L) \cosh^2[g(\omega_s)L].$$
 (3.8)

Exponential gain requires $|\Delta k| < 2|\kappa|$ across the desired signal band. The central design task is therefore to engineer $\Delta k(\omega_s) \approx 0$ broadly while maintaining low loss and good impedance match.

3.4 Parametric amplification and the applied modulation

In a Josephson traveling-wave implementation with Kerr $(\chi^{(3)})$ nonlinearity, the pump current modulates the effective inductance of the line. Writing the total current as $I(t) = I_p \cos \omega_p t + i_s \cos \omega_s t + \dots$ and expanding the Josephson inductance as $L_J(I) \approx L_{J0} \left[1 + (I/I_*)^2 \right]$, one finds that even in the absence of the signal the inductance is explicitly time dependent,

$$L_J(t) \simeq L_{J0} \left[1 + \frac{1}{2} \left(\frac{I_p}{I_*} \right)^2 + \frac{1}{2} \left(\frac{I_p}{I_*} \right)^2 \cos(2\omega_p t) \right].$$
 (3.9)

The pump therefore produces a parametric modulation of the line's reactance at frequency $2\omega_p$, together with a DC shift. Small signal and idler sidebands experience this time-varying medium as a phase and amplitude coupling that enforces the four-wave-mixing condition $\omega_s + \omega_i = 2\omega_p$ and enables exponential gain when momentum conservation, or phase matching, is also satisfied. In this current-pumped 4WM case, the modulation is generated intrinsically by the junction's nonlinear inductance rather than by an external flux drive. By contrast, alternative three-wave-mixing designs deliberately create an odd (cubic) nonlinearity using asymmetric elements such as SNAILs or flux-biased SQUIDs¹; a single pump at ω_p then realizes $\omega_s + \omega_i = \omega_p$. The Eom-style resonant phase-matched architecture discussed here is based on the former, Kerr-mediated 4WM modality, with dispersion engineered so that the pump-selective phase correction aligns the mixing products over a broad band.

$$U(\phi) \approx U_0 + \frac{a_2}{2} (\phi - \phi_0)^2 + \frac{a_3}{3!} (\phi - \phi_0)^3 + \frac{a_4}{4!} (\phi - \phi_0)^4 + \cdots,$$

with $a_3 \neq 0$ set by the asymmetry and the applied flux. Similarly, a dc-flux-biased SQUID modulates its effective inductance $L_{\rm SQ}(\Phi_{\rm dc})$ and, around an appropriate operating point, also admits a nonvanishing cubic coefficient in the local expansion of its potential-phase relation. The resulting three-wave-mixing processes obey

$$\omega_p = \omega_s + \omega_i, \qquad \Delta k = k_p - k_s - k_i + \Delta k_{\rm nl} \approx 0,$$

where $\omega_{p,s,i}$ and $k_{p,s,i}$ are the angular frequencies and wavevectors of pump, signal, and idler, respectively, and $\Delta k_{\rm nl}$ accounts for pump-induced nonlinear phase shifts. By contrast, a single unbiased Josephson junction is inversion symmetric, yielding predominantly a quartic nonlinearity that supports four-wave mixing according to

$$\omega_s + \omega_i = 2\omega_p, \qquad \Delta k = 2k_p - k_s - k_i + \Delta k_{\rm nl} \approx 0.$$

SNAILs and flux-biased SQUIDs thus provide a tunable, effective $\chi^{(2)}$ response for phase-sensitive or phase-preserving parametric amplification based on three-wave interactions, distinct from Kerr-type four-wave-mixing architectures.

¹SNAILs or flux-biased SQUIDs are superconducting loop elements engineered to break the inversion symmetry of the Josephson potential, thereby realizing an effective cubic nonlinearity suitable for three-wave mixing. A SNAIL (Superconducting Nonlinear Asymmetric Inductive eLement) employs an asymmetric junction configuration such that, under a dc flux bias $\Phi_{\rm dc}$, the potential expanded about its operating phase ϕ_0 contains a tunable cubic term,

3.5 Resonant phase matching: pump-selective dispersion engineering

In a traveling-wave parametric amplifier, the phase-matching condition among pump, signal, and idler waves is governed by the line's dispersion relation. Ordinary periodic loading—often referred to as bandgap or dispersion engineering—achieves control of dispersion by introducing a deliberate spatial periodicity in the transmission line's impedance. This is typically implemented through regularly repeating width variations or the periodic addition of capacitive or inductive loadings (e.g., stubs). Such modulation transforms the line into an artificial medium described by a Bloch-type dispersion relation that exhibits photonic stopbands (bandgaps). When the pump frequency lies near a designed stopband edge, the group velocity can be tailored to suppress unwanted harmonic generation and to enable broadband phase matching for three- or four-wave mixing processes. However, ordinary periodic loading modifies the dispersion of the pump, signal, and idler simultaneously. This often narrows the useful gain bandwidth or increases insertion loss due to residual reflection and photonic stopbands.

To overcome these limitations, the <u>resonant phase-matching</u> (RPM) technique introduces frequency-selective dispersion that acts primarily on the pump. In this approach, weakly coupled subwavelength shunt resonators are embedded periodically along the transmission line (3.2). Near their resonance frequency ω_r , these resonators provide a sharply frequency-dependent shunt susceptance, describable to leading order as

$$Y_{\rm sh}(\omega) \simeq iB(\omega) \approx \frac{i\omega C_c}{1 - \omega^2/\omega_r^2 + i(\omega/\omega_r Q_r)},$$
 (3.10)

where C_c denotes the coupling capacitance and Q_r is the resonator's intrinsic quality factor.

In the transmission-line picture, the periodic array of such resonators produces a localized perturbation to the pump wavevector,

$$k_p \to k_p + \delta k_p(\omega_p), \qquad \delta k_p \propto \text{Re} \{Y_{\text{sh}}(\omega_p)\}.$$
 (3.11)

By positioning the pump slightly below the resonator frequency ω_r —on the dispersive flank of its response—the pump wavevector k_p is increased, whereas the signal and idler wavevectors remain largely unaffected because they are detuned by amounts much greater than the resonator linewidth. The overall phase mismatch can then be expressed as

$$\Delta k(\omega_s) = \left[2(k_p + \delta k_p) \right] - k_s(\omega_s) - k_i(2\omega_p - \omega_s) + 2\gamma P_p, \tag{3.12}$$

where γ is the nonlinear coefficient and P_p is the pump power. Appropriately tuning δk_p enables near-zero phase mismatch ($\Delta k \approx 0$) across a broad frequency range, yielding exponential parametric gain while maintaining low reflection and minimal additional loss.

can be tuned close to zero over multi-gigahertz spans even though the resonator itself is narrowband. Weak coupling and the resonator spacing determine the magnitude and smoothness of δk_p ; apodization of the coupling can suppress gain ripple from periodicity². Because the resonators act primarily on the pump, the signal and idler experience minimal added insertion loss and avoid stopbands within the gain window, which is a principal advantage of RPM over Bragg-based strategies [22], [23].

²Here, "apodization" means a deliberate, slow taper of the coupling strength (or equivalently the impedance/loading amplitude or period) along the device so that unit cells are not strictly identical. By breaking exact periodicity, the taper softens Bragg edges, reduces distributed reflections and Fabry–Pérot–like standing waves, and thus suppresses gain ripple, yielding a flatter passband while preserving broadband phase matching. Common choices include raised–cosine (Hann), Blackman, Gaussian, or chirped tapers.

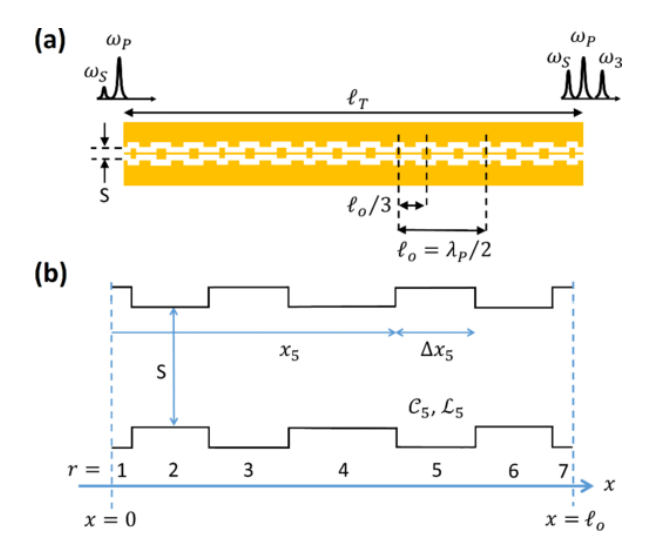


Figure 3.2: Concept of resonant phase matching (RPM): weakly coupled, subwavelength shunt resonators introduce pump-selective dispersion that corrects the phase mismatch without significantly affecting the signal or idler. Reproduced from [21].

3.6 Bandwidth and gain flatness

The instantaneous bandwidth is the range of signal frequencies ω_s for which $|\Delta k(\omega_s)| < 2|\kappa|$ holds with tolerable ripple. The frequency dependence of Δk receives contributions from intrinsic line dispersion due to C_J and finite unit-cell size, from the nonlinear SPM/XPM shift $2\gamma P_p$, and from the pump-selective correction $2 \delta k_p(\omega_p)$ produced by RPM. Practical design proceeds by selecting a pump ω_p well below the plasma edge and slightly below the resonator frequency to obtain the desired δk_p , by choosing resonator coupling and periodicity to set the overall magnitude and smoothness of the correction, and by ensuring that $k_{s,i}$ remain smooth across the target band so that photonic bandgaps do not intrude. Early RPM devices achieved about 12 to 20 dB gain over roughly 3 to 4 GHz [23], [24], and theoretical studies together with refined architectures indicate that 5 to 6.5 GHz 3dB bandwidths are feasible when multimode leakage is controlled [26].

3.7 Noise and the quantum limit

A phase-preserving amplifier must add at least half a photon of noise at its input, $n_{\text{add}} \geq 1/2$. In Josephson traveling-wave parametric amplifiers (JTWPAs), excess above this limit arises primarily from distributed internal loss along the line and from incoherent leakage into additional modes such as higher-order sidebands. A mesoscopic circuit-quantum model with substrate loss yields a useful expression for the added noise,

$$n_{\rm add}(\omega_s) \approx \frac{1}{2} + \int_0^L dz \, \epsilon(z) \left[n_{\rm th}(\omega_s, T) + \frac{1}{2} \right] e^{-2g(\omega_s)(L-z)}, \tag{3.13}$$

where $\epsilon(z)$ represents distributed loss and $n_{\rm th}$ the thermal occupation of the reservoir. Loss near the input is exponentially suppressed by the subsequent gain, whereas loss near the output directly degrades quantum efficiency. A complementary multimode quantum input—output perspective identifies coherent leakage into sidebands and backward-propagating modes as dominant noise pathways; by engineering the mode structure, including with RPM and spatial modulation, it is possible in principle to approach ideal quantum efficiency [26]. In practice, achieving low added noise requires minimizing

dielectric loss in capacitors and resonators, preserving a low-loss idler path since idler loss contributes directly to n_{add} , and controlling out-of-band impedances to avoid parametric oscillations.

3.8 Dynamic range, saturation, and intermodulation

Saturation mechanisms in JTWPAs include pump depletion as energy is transferred to signal and idler, Kerr-induced detuning that modifies Δk as intracircuit powers increase, and higher-order mixing and intermodulation among multiple tones. A useful scaling for the 1 dB compression point is

$$P_{\text{1dB}} \propto \frac{I_c^2 Z_0}{N p} f(\text{dispersion}, Q_r, \text{tolerances}),$$
 (3.14)

where N is the number of cells and Z_0 the characteristic impedance. Lower participation raises headroom but reduces the per-length nonlinearity, which is typically compensated by increasing N to reach the target gain, Qualitatively, gain compression in a Josephson travelling-wave parametric amplifier (JTWPA) arises from three main mechanisms: (i) pump depletion, where energy from the strong pump tone is transferred to the signal and idler; (ii) self- and cross-phase modulation due to the Kerr nonlinearity, which detunes the phase-matching condition as intracircuit powers increase; and (iii) the generation of higher-order mixing products when multiple tones are present, leading to intermodulation and crosstalk. In practical terms, the 1 dB compression point increases with the junction critical current and the line's characteristic impedance, but decreases with the number of cells and the inductive participation ratio. The proportionality factor is determined by the quality of the dispersion engineering—specifically, the phase-matching margin across the band—as well as by the loss and coupling of the phase-matching resonators and by fabrication inhomogeneities along the line. Reducing inductive participation increases linearity headroom but weakens the nonlinear coupling per unit length, typically requiring longer lines to recover the target gain. This trade-off underlies the scaling.

3.9 Comparison with alternative dispersion strategies

Resonant phase matching is one member of a wider family of dispersion-engineering techniques. Smooth impedance modulation without discrete resonators can also establish phase matching for 4WM while suppressing intrinsic gain ripple. Such approaches highlight that low insertion loss and control of the multimode spectrum are decisive for bandwidth, noise, and headroom. Nevertheless, the pump selectivity of RPM is particularly effective at delivering broad gain without degrading the signal or idler path, a distinction that becomes pronounced when the idler must propagate with low loss to preserve quantum efficiency [22], [23], [24].

3.10 Magnet-free nonreciprocal isolator via traveling index modulation

The dispersion engineering and parametric mixing concepts developed above extend naturally to nonreciprocal components that are compatible with cryogenic quantum hardware. In particular, one can realize an on-chip, magnet-free microwave isolator by imposing a traveling index modulation in high-impedance superconducting transmission lines. This section introduces such an isolator and situates it alongside the Eom-style dispersion strategies already discussed, while drawing on coupled-mode theory in periodically loaded media and on traveling-wave parametric frameworks that we have used throughout.

Introduction and design objective

Ferrite isolators leverage the Faraday effect under static magnetic bias but are incompatible with superconducting qubits, which are highly sensitive to magnetic fields. The objective here is a four-port isolator implemented entirely in thin-film superconductors and driven by radio-frequency pumps, exhibiting low forward loss, strong reverse isolation, and near-quantum-limited added noise over a multi-hundred-megahertz band. Non-reciprocity arises from a traveling modulation of kinetic inductance, which imparts an effective momentum bias to waves propagating in opposite directions and thereby breaks time-reversal symmetry without magnetization. Theoretical foundations build directly from the nonlinear telegrapher's equations for kinetic-inductance lines and from a Floquet-Bloch description of periodically loaded media, with device-level choices such as loading pattern, impedance tapers, pump phasing, and boundary matching tied to the coupled-mode theory of Erickson and Pappas [21] and to dispersion-engineering strategies introduced by Eom and collaborators [4].

Governing equations and mixing mechanisms

A superconducting transmission line with geometric inductance and capacitance per unit length (L_g, C) and with current-dependent kinetic inductance $L_k(I)$ obeys the telegrapher's equations

$$\partial_z V = -(L_q + L_k(I)) \partial_t I - RI, \qquad \partial_z I = -C \partial_t V - GV.$$
 (3.15)

In thin, disordered nitrides operated well below T_c , L_k dominates and is an even function of current. Expanding about a strong pump I_p and a weak signal current i yields

$$L_k(I_p + i) \simeq L_{k0} \left[1 + \eta_2 \left(\frac{I_p}{I_*} \right)^2 \right] + 2L_{k0}\eta_2 \left(\frac{I_p}{I_*} \right) \left(\frac{i}{I_*} \right) + L_{k0}\eta_2 \left(\frac{i}{I_*} \right)^2 + \cdots,$$
 (3.16)

which produces a Kerr-like cubic response and, when a DC bias or structural asymmetry is present, an effective quadratic term that enables three-wave mixing. Under the slowly varying envelope approximation, a strong undepleted pump at ω_p and weak sidebands at ω_s and ω_i satisfy the coupled-mode system

$$\frac{dA_s}{dz} = i \kappa_4 A_i^* A_p^2 e^{i\Delta kz} - \frac{\alpha_s}{2} A_s, \tag{3.17}$$

$$\frac{dA_i}{dz} = i \kappa_4 A_s^* A_p^2 e^{i\Delta kz} - \frac{\alpha_i}{2} A_i, \tag{3.18}$$

with $\Delta k = 2k_p - k_s - k_i$ and with κ_4 proportional to $\eta_2 L_{k0}/(I_*^2 Z_0)$ [21]. Bias-enabled three-wave mixing follows with the same structure but with $\Delta k = k_p - k_s - k_i$ and with coefficients linear in the bias and pump amplitudes. This parametric language mirrors the amplifier case, but here the mixing pathways are orchestrated to create direction-dependent interference rather than net gain.

Floquet-Bloch dispersion and engineered phase matching

Periodic impedance loading bends the dispersion and opens photonic stop bands that can be aligned with pump harmonics. The unit-cell ABCD matrix and its Floquet eigenvalues define the complex Bloch wavenumber $k_B(\omega)$ and the Bloch impedance $Z_B(\omega)$ for forward supermodes. In a periodically loaded transmission line with unit-cell period a, the voltage–current state $\mathbf{x}(z) \equiv (V(z), I(z))^{\mathsf{T}}$ obeys $\mathbf{x}(z+a) = \mathbf{M}(\omega) \mathbf{x}(z)$, where the unit-cell ABCD (transfer) matrix is $\mathbf{M}(\omega) = \begin{pmatrix} A & B \\ C & D \end{pmatrix}$. Floquet–Bloch theory diagonalizes \mathbf{M} via its eigenvalues $\lambda_{\pm}(\omega)$, defined by $\det[\mathbf{M} - \lambda \mathbf{I}] = 0$. Writing $\mu(\omega) \equiv \frac{A+D}{2}$, one obtains

$$\lambda_{\pm}(\omega) = \mu \pm \sqrt{\mu^2 - 1}, \qquad \lambda_{\pm} = e^{\pm \gamma(\omega) a},$$

which defines the complex Bloch propagation constant $\gamma(\omega) = \alpha(\omega) + i k_B(\omega)$ through

$$\cosh(\gamma a) = \mu(\omega) \quad \Rightarrow \quad \gamma(\omega) = \frac{1}{a}\operatorname{arccosh}(\mu(\omega)).$$

In lossless passbands $|\mu| \leq 1$, $\gamma = ik_B$ is purely imaginary and $\cos(k_B a) = \mu$; in stopbands $|\mu| > 1$, $\gamma = \alpha$ is real and $\cosh(\alpha a) = \mu$. The Bloch impedance for the forward supermode is the eigenvector ratio $Z_B^+(\omega) \equiv V/I$ associated with λ_+ :

$$Z_B^+(\omega) = -\frac{B}{A - \lambda_+} = \frac{\lambda_+ - D}{C},$$

which is real in passbands and purely imaginary in stopbands for reciprocal, lossless cells (AD-BC=1). Periodic impedance loading (e.g., weak shunt resonators or smooth impedance modulation) shapes $\mu(\omega)$, bending the dispersion $k_B(\omega)$ and opening photonic bandgaps near Bragg conditions $k_Ba \approx m\pi$ $(m \in \mathbb{Z})$. In JTWPAs this is used to: (i) place a stopband at selected pump harmonics (e.g., $2\omega_p$, $3\omega_p$) to suppress parasitic generation, and/or (ii) bias the pump just below a band edge to increase k_p and thereby correct the 4WM phase mismatch without adding loss for signal/idler ("resonant phase matching"). Projection of the nonlinear telegrapher's equations onto these supermodes produces frequency-dependent coupled-mode coefficients and a phase mismatch of the form

$$\Delta k(\omega) = 2k_B(\omega_p) - k_B(\omega_s) - k_B(\omega_i) + \delta k_{\rm NL}(|A_p|^2), \tag{3.19}$$

where $\delta k_{\rm NL}$ accounts for self- and cross-phase modulation [21]. Designs that place $3\omega_p$ in a stop band mitigate parasitic third-harmonic generation and stabilize pass-band gain or conversion [4]. Because k_B and Z_B are complex in realistic films, attenuation and impedance asymmetry must be carried into the coupled-mode evolution to avoid optimistic predictions. In contrast to the amplifier, the isolator uses modulation phasing and boundary conditions to tailor conversion pathways that differ for the two propagation directions.

Directional phase bias and non-reciprocity

In the presence of a traveling modulation, the forward and backward transfers are coherent sums of a direct term and a frequency-converted pathway with opposite accumulated phases. Denoting by t_0 the direct contribution and by $\Gamma e^{\pm i\Phi}$ the converted pathway reprojected onto the signal band, one finds

$$t_{\rightarrow}(\omega_s) \approx t_0(\omega_s) + \Gamma(\omega_s)e^{i\Phi(\omega_s)}, \qquad t_{\leftarrow}(\omega_s) \approx t_0(\omega_s) + \Gamma(\omega_s)e^{-i\Phi(\omega_s)}.$$
 (3.20)

Appropriate pump phasing, interaction length, and dispersion arrange constructive interference forward and destructive interference backward, which yields $|S_{21}| \gg |S_{12}|$ without magnetic bias [21]. The same dispersion-engineering toolkit that underpins the Eom-style broadband amplifier thus enables magnet-free isolation when combined with traveling-wave spatiotemporal modulation and careful impedance matching. A traveling spatiotemporal modulation of the line parameters, $m(z,t) = m_0 \cos(Kz - \Omega t + \phi_p)$, breaks Lorentz reciprocity by imprinting a direction-dependent phase on frequency-conversion pathways. In a coupled-mode/Born approximation, the signal at ω_s reaches the output via (i) a direct path with complex amplitude $t_0(\omega_s)$, and (ii) a weak, two-step frequency-converted path that leaves and re-enters the signal band. Projecting the converted pathway back to ω_s yields an amplitude

$$\Gamma(\omega_s)e^{i\Phi(\omega_s)} \simeq i\int_0^L \kappa(\omega_s) e^{i\Delta k_{\to}(\omega_s) z} dz = \kappa L e^{i\Delta k_{\to}L/2} \operatorname{sinc}\left(\frac{\Delta k_{\to}L}{2}\right),$$

with forward mismatch $\Delta k_{\rightarrow}(\omega_s) = k_i(\omega_i) - k_s(\omega_s) - K$. Reversing propagation flips the sign of the modulation wavevector in the phase-matching condition, so that $\Delta k_{\leftarrow} = k_i - k_s + K$ and the

reprojected term acquires the opposite phase, $\Gamma e^{-i\Phi}$. This directly gives

$$t_{\rightarrow}(\omega_s) \approx t_0(\omega_s) + \Gamma(\omega_s)e^{i\Phi(\omega_s)}, \qquad t_{\leftarrow}(\omega_s) \approx t_0(\omega_s) + \Gamma(\omega_s)e^{-i\Phi(\omega_s)}.$$

Choosing modulation phase ϕ_p , interaction length L, and dispersion so that $\Phi(\omega_s) \approx 2\pi n$ forward and $\Phi(\omega_s) \approx (2n+1)\pi$ backward arranges constructive interference in the forward direction and destructive interference in the backward direction, yielding $|S_{21}| \gg |S_{12}|$ without magnetic bias. In Kerr-pumped JTWPAs, the strong pump at ω_p produces an effective index modulation at $(\Omega, K) \approx (2\omega_p, 2k_p)$, so a useful approximation is $\Phi_{\to}(\omega_s) \approx [k_i(\omega_i) - k_s(\omega_s) - 2k_p]L + 2\phi_p$, which flips sign under reversal. The same dispersion-engineering knobs used in Eom-style broadband amplifiers (e.g., resonant phase matching or smooth impedance modulation) control $k_s(\omega)$, $k_i(\omega)$, and $k_p(\omega)$, thus tuning $\Phi(\omega_s)$ and $\Gamma(\omega_s)$ for broadband, magnet-free isolation when paired with traveling modulation and good impedance matching.

3.11 Sketch of the coupled-mode derivation

Starting from the telegrapher equations with a current-dependent inductance L(I), one expands the flux field $\phi(z,t)$ in band-limited modes and applies a slowly varying envelope approximation. For a pump at (k_p, ω_p) and weak sidebands near ω_s and $\omega_i = 2\omega_p - \omega_s$, the nonlinear current $I_{\rm nl} \propto \partial_t^2 \phi \, \partial_t \phi$ generates four-wave-mixing source terms at $\omega_{s,i}$. Projecting onto the linear eigenmodes and retaining only near-resonant terms yields envelope equations

$$\partial_z A_s = -\frac{\alpha_s}{2} A_s + i\gamma \left(2|A_p|^2 A_s + A_p^2 A_i^* e^{i\Delta kz} \right), \tag{3.21}$$

$$\partial_z A_i = -\frac{\bar{\alpha}_i}{2} A_i + i\gamma \left(2|A_p|^2 A_i + A_p^2 A_s^* e^{i\Delta kz} \right), \tag{3.22}$$

with $\Delta k = 2k_p - k_s - k_i$ determined by the linear dispersion. Absorbing SPM/XPM into an effective phase mismatch $\Delta k_{\rm nl} = 2\gamma |A_p|^2$ and assuming an undepleted pump reduces the system to the coupled-mode form presented earlier. Linear loss enters as a non-Hermitian perturbation that multiplies the gain by $\exp(-\alpha_s L)$ and skews the spectrum toward lower gain near the output where loss is least suppressed.

3.12 KI-TWPA Synthesis for Isolator Design

The modern kinetic-inductance traveling-wave parametric amplifier framework provides an end-toend methodology that connects unit-cell geometry to device-level behavior. The procedure begins with a bias-expanded L_k that unifies four-wave and three-wave processes, proceeds by extracting complex $k_B(\omega)$ and $Z_B(\omega)$ from the chosen periodically loaded line, and formulates coupled-mode or harmonic-balance equations that evolve forward and reverse supermodes, pump harmonics and cascaded idlers with frequency-dependent loss. Port reflections are incorporated through measured or targeted S-parameters so that gain ripple and oscillation risk are assessed via loop-gain criteria [21].

In degenerate four-wave mixing with an undepleted pump the small-signal gain reads

$$G_s = 1 + \frac{k_p |A_p|^2}{I_*^2} g^{-1} \sinh^2(gL), \qquad g = \sqrt{\left(\frac{k_p |A_p|^2}{I_*^2}\right)^2 - \left(\frac{\Delta k}{2}\right)^2},$$
 (3.23)

which emphasizes that engineered phase matching governs bandwidth and ripple [21]. In bias-enabled three-wave mixing, expressions of the form $G_s \simeq \cosh^2(gL)$ with $g \propto I_b I_{p0}$ highlight the co-design of bias, pump power and Bloch dispersion. Predictive bandwidth and spur control require evolving the pump and retaining at least the third harmonic and its sidebands; placing $3\omega_p$ in a stop band is an effective mitigation strategy [4]. Dual-pump four-wave operation offers bias-free flattening through

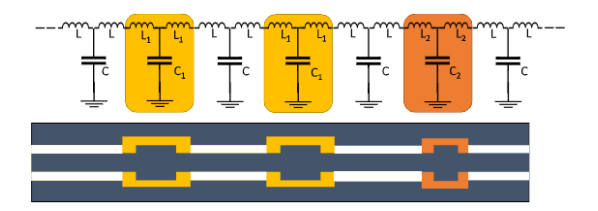


Figure 3.3: Periodically widened transmission line with alternating segment widths corresponding to distinct inductance (L) and capacitance (C) values. Reproduced from [1].

cross-phase modulation of two pumps, at the cost of additional harmonic-suppression constraints within the unit-cell dispersion. 3

3.13 Implementation and Materials

Each parametric section is realized as a compact spiral of dispersion-engineered coplanar waveguide with characteristic impedance in the few-hundred-ohm range owing to large kinetic inductance. Impedance transformation to 50 Ω is provided by adiabatic tapers shaped according to Klopfenstein's profile to bound in-band reflections [27]. Short widened segments placed with period D position the pump in a pass band and the third harmonic in a stop band, while the duty cycle is tuned so that $k_B(\omega)$ yields small, slowly varying Δk across the operating band [4]. Bias and pump are injected through chokes and broadband capacitive tees that present high impedance at the signal frequency.

High-kinetic-inductance NbTiN or NbN films are deposited by reactive sputtering; HIPIMS produces dense, smooth and stoichiometrically stable films with elevated critical current density, which reduce microwave loss and improve uniformity of sheet inductance relative to conventional DC sputtering [8]. Sub-micrometric gaps in the coupler and narrow sections of the loaded line are defined by electron-beam lithography (3.3), while low-loss dielectrics, superconducting vias and air bridges control parasitic modes.

Erickson and Pappas develop a rigorous modal treatment for multiwave mixing in periodically loaded kinetic-inductance lines, combining a Floquet-Bloch bandstructure with coupled-mode evolution on forward-propagating supermodes [21]. The framework unifies four-wave mixing in unbiased operation and three-wave mixing under DC bias by deriving both from the same current-expanded

$$\Delta k_{\rm dp}(\omega_s) = k(\omega_s) + k(\omega_i) - k(\omega_{p1}) - k(\omega_{p2}) + \Delta k_{\rm nl},$$

where the Kerr nonlinearity provides a largely frequency-flat correction $\Delta k_{\rm nl} \approx 2\gamma (P_1 + P_2)$ for co-polarized waves in the weak-signal, undepleted-pump regime (capturing SPM/XPM on the signal/idler by the pumps). Choosing symmetric pumps about a center ω_0 , i.e. $\omega_{p1} = \omega_0 - \Delta$, $\omega_{p2} = \omega_0 + \Delta$, and writing $\omega_s = \omega_0 + \delta$ so that $\omega_i = \omega_0 - \delta$, a Taylor expansion of the linear dispersion $k(\omega)$ around ω_0 gives the even-order structure

$$\Delta k_{\rm dp}(\omega_s) \approx k''(\omega_0)(\delta^2 - \Delta^2) + \frac{1}{12}k^{(4)}(\omega_0)(\delta^4 - \Delta^4) + \dots + 2\gamma(P_1 + P_2),$$

because all odd-order terms cancel in the symmetric sums $k(\omega_0 \pm x)$. Hence, by selecting the pump spacing Δ and total pump power $P_1 + P_2$ so that the constant (nonlinear) and quadratic (dispersion) terms compensate over the intended δ -range, one achieves "bias-free flattening" of $\Delta k_{\rm dp}(\omega_s)$ and thus a broad, flatter gain profile—without any DC flux bias. This strategy underlies dual-pump JTWPA operation and broadband squeezing demonstrations, while also introducing extra spectral hygiene requirements: the two pumps generate a beat note at $\Omega \equiv |\omega_{p2} - \omega_{p1}| = 2\Delta$ and drive additional mixing ladders, so the unit-cell dispersion/impedance must suppress spurious pathways and harmonics (e.g., features near $2\omega_{p1}$, $2\omega_{p2}$, $\omega_{p1} \pm \Omega$, $\omega_{p2} \pm \Omega$, and secondary idler bands) without attenuating the primary idler. In practice this is handled by the same dispersion-engineering toolkit used for Eom-style broadband amplifiers—resonant phase matching or smooth impedance modulation— augmented with explicit harmonic/sideband management and careful impedance matching.

³Consider two co-propagating pumps at ω_{p1} and ω_{p2} with undepleted powers $P_{1,2}$ and phases $\phi_{1,2}$. For a weak signal at ω_s , the primary nondegenerate idler is $\omega_i = \omega_{p1} + \omega_{p2} - \omega_s$, with additional secondary idlers at $2\omega_{p1} - \omega_s$ and $2\omega_{p2} - \omega_s$ from single-pump 4WM. The dual-pump phase mismatch can be written

kinetic inductance. A central prediction is that in four-wave operation the signal and idler often occupy different Bloch bands, which limits the extent to which the phase mismatch can be flattened and naturally produces gain undulations. By contrast, bias-enabled three-wave operation can place signal and idler in the same band, leading to smoother gain provided that the bias-dependent nonlinear phase shift compensates the linear mismatch.

The analysis also quantifies the role of harmonic suppression: widening third-order stop bands and positioning the pump near the first gap suppress the third harmonic and its sidebands, improving conversion efficiency and stabilizing the pass band. Methodologically, the Bloch-mode formulation explains several experimental regularities in kinetic-inductance traveling-wave devices, but idealized terminations and the absence of explicit loss tend to overestimate gain and understate ripple. For isolator design the implications are immediate, since the same ingredients that flatten amplifier gain—cobanding of signal and idler in three-wave operation, strong third-harmonic suppression and extraction of complex k_B and Z_B from the fabricated unit cell—directly translate into deeper isolation nulls and reduced spur content in the isolator.

Device characterization at millikelvin temperatures employs vector-network analysis with cryogenic calibration. Calibration planes are defined at the device package, and through paths are equalized in delay so that the cascaded scattering matrix reproduces design phases. Added-noise measurements use cold-load or Y-factor methods. Pump distribution uses low-phase-noise sources locked to a common reference so that the relative pump phase between isolators can be trimmed in situ. Electromagnetic shielding and magnetic hygiene prevent flux penetration, which would otherwise degrade quality factor and raise insertion loss.

A magnet-free isolator can be engineered by combining dispersion-controlled kinetic-inductance traveling-wave sections. The analysis proceeds from nonlinear telegrapher's equations through Bloch-mode coupled-wave evolution, mirroring the kinetic-inductance traveling-wave parametric amplifier program [21]. Periodic loading in the sense of Eom et al. [4] provides phase matching and harmonic control. With films that deliver uniform high impedance and with reflection-aware packaging, the architecture achieves low forward loss, strong reverse isolation across useful bands and compatibility with superconducting quantum circuits.

3.14 Fabrication and Material Requirements

3.14.1 Superconducting Materials and Film Quality

The performance of the magnet-free superconducting isolator critically depends on the quality of the superconducting thin films employed in both the parametric isolators and the directional coupler. Niobium titanium nitride (NbTiN) is selected as the primary material due to its high kinetic inductance, relatively high critical temperature (typically 10–15 K), and compatibility with standard microfabrication processes. NbTiN films exhibit lower microwave losses and higher magnetic-field resilience than NbN, making them particularly suitable for quantum-limited cryogenic microwave applications [4].

Films are deposited by reactive magnetron sputtering, with precise control of nitrogen partial pressure to achieve the desired stoichiometry and superconducting properties [14], [15]. Operating in the transition regime of the I–V characteristic of the sputtering discharge—where the target surface is partially nitrided—maximizes the film critical temperature and homogeneity [14], [15]. Maintaining a constant discharge current during growth further stabilizes the target surface composition, minimizing run-to-run variability and ensuring reproducible film performance.

Film thickness is optimized to balance competing requirements: thin films enhance kinetic inductance, while thicker films reduce microwave loss [4]. Typical NbTiN thicknesses between 35 nm and 50 nm yield sheet inductances in the range of $10-20 \text{ pH/}\square$ [15]. Thickness uniformity across the device area must be better than 5% to guarantee consistent impedance and critical current density, avoiding

localized excess losses or hot spots during high-frequency operation.

3.15 Applications and System Integration

3.15.1 Quantum Computing Applications

The primary application domain of the developed superconducting isolator is in quantum information processing, where it serves as a nonreciprocal interface between sensitive qubits and high-gain amplifier chains. In superconducting quantum processors, isolators suppress back-action from amplifiers, protect qubits from noise re-entry, and enable multiplexed readout of multiple resonators through shared amplification stages. The magnet-free design is essential for preserving qubit coherence, since even small magnetic fields degrade Josephson junction performance and cause decoherence.

System-level integration requires careful impedance matching, thermal anchoring, and electromagnetic shielding. The high characteristic impedance of superconducting spiral or meander-line inductors often necessitates impedance transformers when interfacing with standard 50 Ω microwave circuitry [15]. Such transformers may be realized as tapered transmission lines or lumped-element impedance networks, depending on the target bandwidth and on-chip spatial constraints.

3.16 Future Directions

3.16.1 Advanced Modulation Schemes

Current implementations employ sinusoidal modulation of kinetic inductance through current injection [4], [21]. Future developments may explore non-sinusoidal and digitally synthesized modulation waveforms to achieve sharper isolation band edges and reduced spurious sidebands.

Machine-learning-based adaptive optimization of pump amplitude and phase could further enable autonomous performance calibration and compensation for environmental drifts, leading to self-stabilizing nonreciprocal devices suitable for long-term operation in quantum computing systems.

3.16.2 Integration with Emerging Quantum Technologies

As superconducting quantum processors scale to larger qubit arrays and higher wiring density, the demands on nonreciprocal signal routing and isolation will intensify. The magnet-free isolator technology developed here is well positioned to address these challenges through continued miniaturization, enhanced integration density, and the introduction of tunable or multifunctional architectures. Potential extensions include hybrid devices incorporating flux tuning, parametric conversion, or optomechanical coupling to provide dynamic control of isolation bandwidth and center frequency **Lecocq2021-cm**.

Monolithic integration with other quantum components—such as resonators, qubits, and amplifiers—represents an important next step toward compact, scalable quantum modules. Emerging fabrication approaches such as three-dimensional integration, wafer bonding, and flip-chip interconnects offer viable routes to achieving dense, low-loss superconducting microwave systems with embedded nonreciprocal functionality [15].

CHAPTER 4

Superconducting Isolator: simulation and fabrication

4.1 Simulation of the CPW Isolator

To evaluate the expected performance of the fabricated CPW isolator, we carried out a suite of electromagnetic and circuit-level simulations inspired by the framework of Sweetnam et al. [1]. In their work, the authors demonstrate that realistic circuit models, incorporating distributed inductance, capacitance, and nonlinear kinetic inductance elements, can reliably reproduce the behavior of traveling-wave superconducting parametric amplifiers (TWPAs). Following a similar approach, we constructed a cascaded ABCD-matrix model of the spiral CPW isolator with periodic loadings, allowing the extraction of the scattering parameters S_{11} , S_{21} , and, in addition, the reverse transmission S_{12} , in order to directly assess isolation.

4.1.1 Workflow

The isolator geometry was parameterized in terms of its unit cell inductance L_0 and capacitance C_0 , extracted from electromagnetic simulations of short sections of the spiral line. Periodic widening of the central conductor was modeled as a modulation of the effective Z_0 , which introduces photonic stop bands selectively in one propagation direction. The ABCD matrices of loaded and unloaded sections were then cascaded to form the full device transfer matrix, from which the complete S-matrix was computed.

4.1.2 Extension to Reverse Transmission

While Sweetnam's analysis primarily focuses on S_{21} (forward gain) and reflection coefficients, in our case we extended the framework to explicitly compute the reverse transmission S_{12} . This quantity is central to the definition of isolation: the isolator is expected to maintain low insertion loss in the forward direction (S_{21} close to 0 dB) while strongly suppressing reverse propagation ($S_{12} \ll 0$ dB). Our simulations confirm that the engineered stop bands and asymmetric loading produce a significant suppression of S_{12} , consistent with the targeted nonreciprocal behavior.

In summary, the simulation framework—adapted from Sweetnam et al. [1] and extended to include S_{12} —provides a powerful predictive tool for validating the design of the spiral CPW isolator before fabrication. The correspondence between bandgap placement, pump frequency tuning, and the achieved forward vs. reverse transmission emphasizes the importance of accurate L_0 and C_0 extraction and careful dispersion engineering.

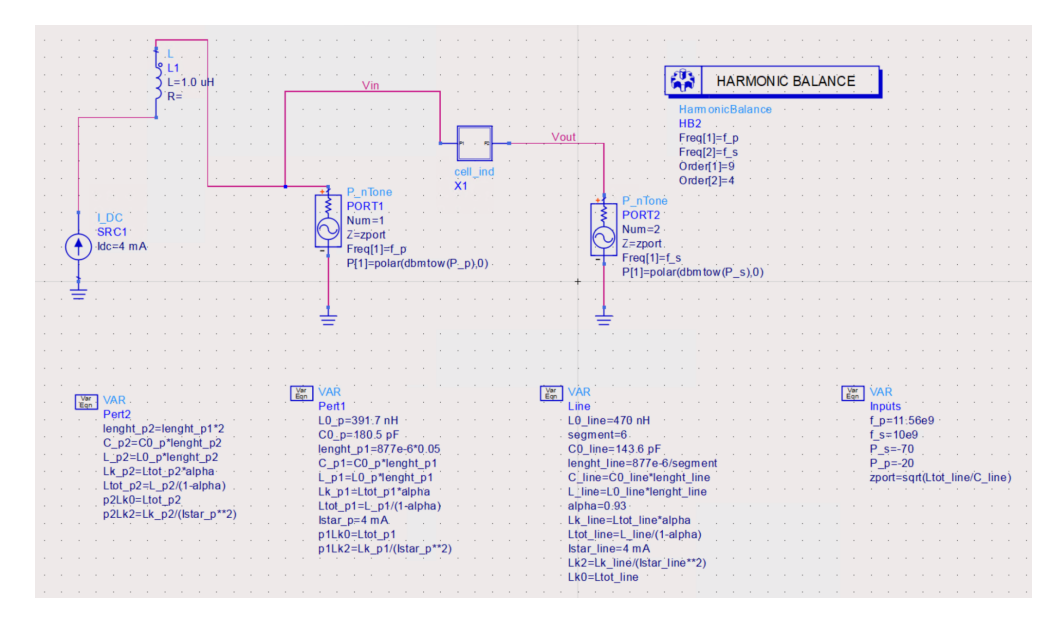


Figure 4.1: Harmonic balance simulation schematic for the parametric isolator unit cell for S21

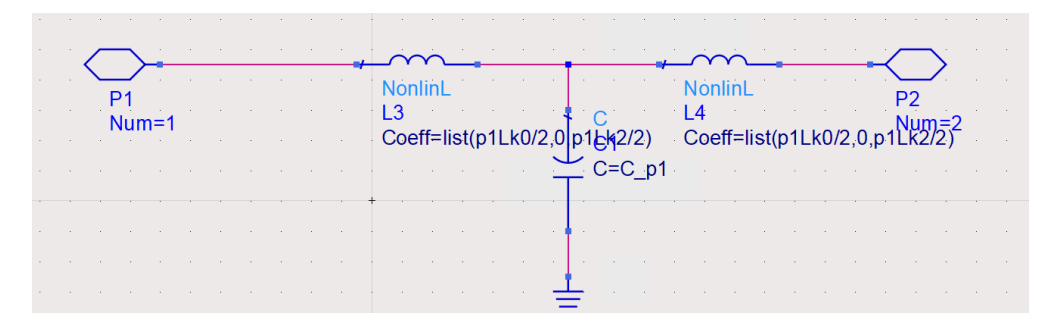


Figure 4.2: Equivalent circuit model for a single unit cell of the dispersion-engineered transmission line.

4.2 Process Overview

The coplanar waveguide (CPW) is realized in a single superconducting layer of NbTiN that is patterned by electron-beam lithography (EBL) and subsequently transferred into the film by fluorine- or chlorine-based plasma etching. The overall sequence, summarized in Fig. 4.5, proceeds as follows: (i) substrate preparation and dehydration bake; (ii) reactive sputter deposition of NbTiN (Sec. 4.4); (iii) spin-coating of the positive-tone e-beam resist ZEP 530 and prebake (Sec. 4.5); (iv) exposure on the HS50 writer (Sec. 4.6); (v) cold development in xylene or ZED-N50 at $0 \pm 1^{\circ}$ C (Sec. 4.7); (vi) pattern transfer by ICP-RIE/RIE using the ZEP mask (Sec. 4.8); and (vii) resist removal in Remover 1165 followed by a final clean (Sec. 4.9).

4.2.1 CPW Layer Stack and Cross-Section Schematic

Figure ?? depicts the cross-section of the CPW employed in the parametric isolator. A high-resistivity Si substrate provides a low-loss mechanical platform. Where used, a thermally grown SiO_2 layer electrically isolates the superconducting metallization from the substrate and mitigates two-level-system loss. The NbTiN film defines the transmission line: a center conductor of width w separated from the ground rails by gaps g. In this work, the NbTiN thickness is typically $t_{\mathrm{NbTiN}} = 35-50$ nm;

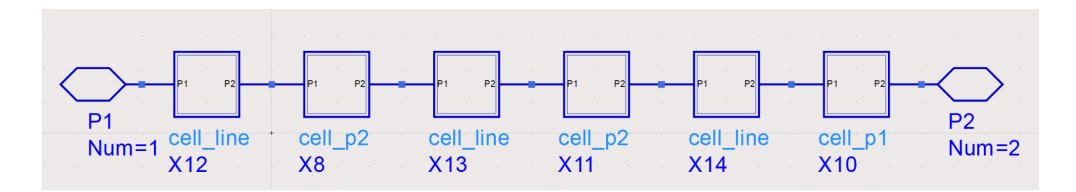


Figure 4.3: Repetition pattern for the line and the loadin structures

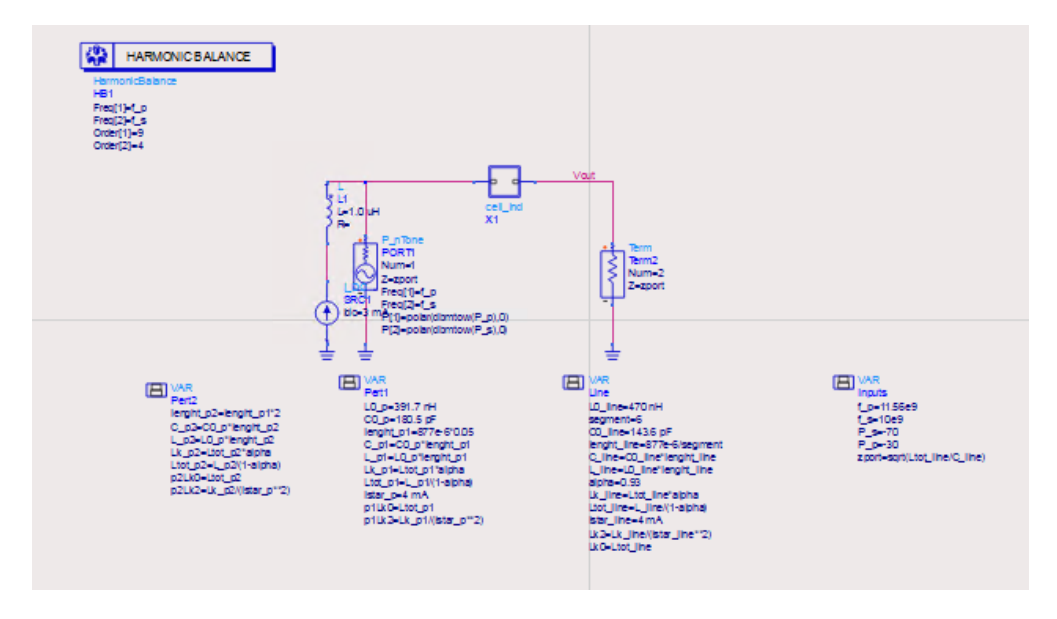


Figure 4.4: Harmonic balance simulation schematic for the parametric isolator unit cell for S12

the optional oxide has thickness $t_{\rm SiO_2} = 200{\text -}300$ nm. Owing to its large sheet kinetic inductance, NbTiN enables characteristic impedances $\gtrsim 150~\Omega$, while the geometric parameters w and g set Z_0 and influence the Bloch dispersion of the periodically loaded spiral.

4.3 Substrate Preparation

High-resistivity Si substrates ($\rho > 10~\mathrm{k}\Omega\cdot\mathrm{cm}$) are employed either with native oxide or with a thermal SiO₂ layer (e.g., 200 nm) to suppress microwave substrate losses. Wafers are solvent-cleaned (5 min acetone followed by 5 min IPA) and dried in N₂. An optional surface activation (2–3 min UV-ozone or a gentle O₂ plasma at 10–30 W) improves wetting and removes residual organics. A dehydration bake at 180°C for 5–10 min on a hotplate completes the preparation.

4.4 Reactive Sputter Deposition of NbTiN

NbTiN is deposited in a load-lock DC (or HiPIMS) magnetron system using either an NbTi alloy target or co-sputtered Nb and Ti in reactive ${\rm Ar/N_2}$. A base pressure $\leq 3 \times 10^{-7}$ Torr is maintained. After a 3–5 min presputter in Ar with the shutter closed, the film is grown at a total pressure of 2–6 mTorr with an N₂ fraction of 5–25% (set by the desired stoichiometry), using 100–300 W target power and with no intentional substrate bias. Substrate temperature is held between ambient and 200°C to tune stress and density. Thicknesses of 20–60 nm are typical (rates 0.2–1.0 nm/s). Post-deposition, thickness and sheet resistance are mapped, and L_{\Box} is estimated as a first-order check of

Flow: Clean \rightarrow NbTiN sputter \rightarrow ZEP 3.50 coat/bake \rightarrow HS50 EBL \rightarrow cold develop \rightarrow ICP-RIE NbTiN etch \rightarrow Remover 1165 strip \rightarrow inspection & metrology.

Figure 4.5: Process flow for the NbTiN CPW.

the high-impedance target. Excessive energetic bombardment is avoided to preserve T_c and minimize loss.

4.5 ZEP 530 Coating and Prebake

The positive-tone resist ZEP 530 is spun to a thickness of 150–250 nm by coating at 4000–6000 rpm for 1 minute. Edge-bead is optionally removed with anisole. A softbake at 180°C for 1 min on a covered hotplate drives off residual solvent. For highly insulating substrates a temporary conductive layer may be used to mitigate charging; on NbTiN this is generally unnecessary.

4.6 HS50 Electron-Beam Lithography

Patterning is performed on a 50 kV HS50 Gaussian-beam system operated in high-speed deflection mode with a thermal field-emission source. The beam current/aperture is chosen to balance speed and resolution; for sub-micrometer features currents of 100–300 pA with 2–5 nm step size are adopted, with careful stigmation and focus at the write field. The nominal ZEP 530 dose lies in the range 150–260 μ C/cm² for 150–250 nm films and is locally calibrated. Curve fracturing enforces a maximum chord error \leq 10 nm on spirals and loading rectangles; write fields of order 100 μ m with \geq 10% field overlap limit stitching. A two-group proximity-effect correction separates narrow arcs from dense loading blocks, with a modest under-dose on the latter to counter local swelling. Global alignment relies on metal or NbTiN markers, and stage drift is kept <10 nm/min. Importantly, an excessive beam current broadens the effective spot and enhances forward scattering, producing edge bowing and rounded corners on periodic loadings—artifacts absent from the CAD and detrimental to impedance uniformity.

4.7 Cold Development (ZEP)

Development is carried out in o-xylene or ZED-N50 at 0°C, using a chilled bath held at 0 ± 1 °C. Typical develop times are 60–90 s, followed by a 30 s IPA rinse (0–20°C) and immediate N₂ dry. When required, a brief O₂ descum (10–20 W for 5–15 s) removes residual scum without appreciable loss of resist thickness. Cold development raises resist contrast and suppresses swelling, thereby improving corner acuity and reducing line-edge/line-width roughness—benefits that are critical for the fidelity of periodic loadings and for ripple control in the final microwave response.

4.8 Dry Etch of NbTiN (Pattern Transfer)

Pattern transfer is performed in ICP-RIE (preferred) or capacitively coupled RIE with ZEP acting as a soft mask. Two families of chemistries are employed. In the fluorine route, SF_6/O_2 at 5–10 mTorr with 400–800 W ICP power and 30–120 W RF bias yields etch rates of order 30–80 nm/min and selectivities of 1:1–2:1 to ZEP. In the chlorine route, $Cl_2/BCl_3/Ar$ at 3–8 mTorr with 500–900 W ICP and 40–120 W RF achieves comparable rates and can provide smoother sidewalls depending on the tool. Over-etch is minimized to preserve loading geometry; if selectivity is marginal, a thin hard mask

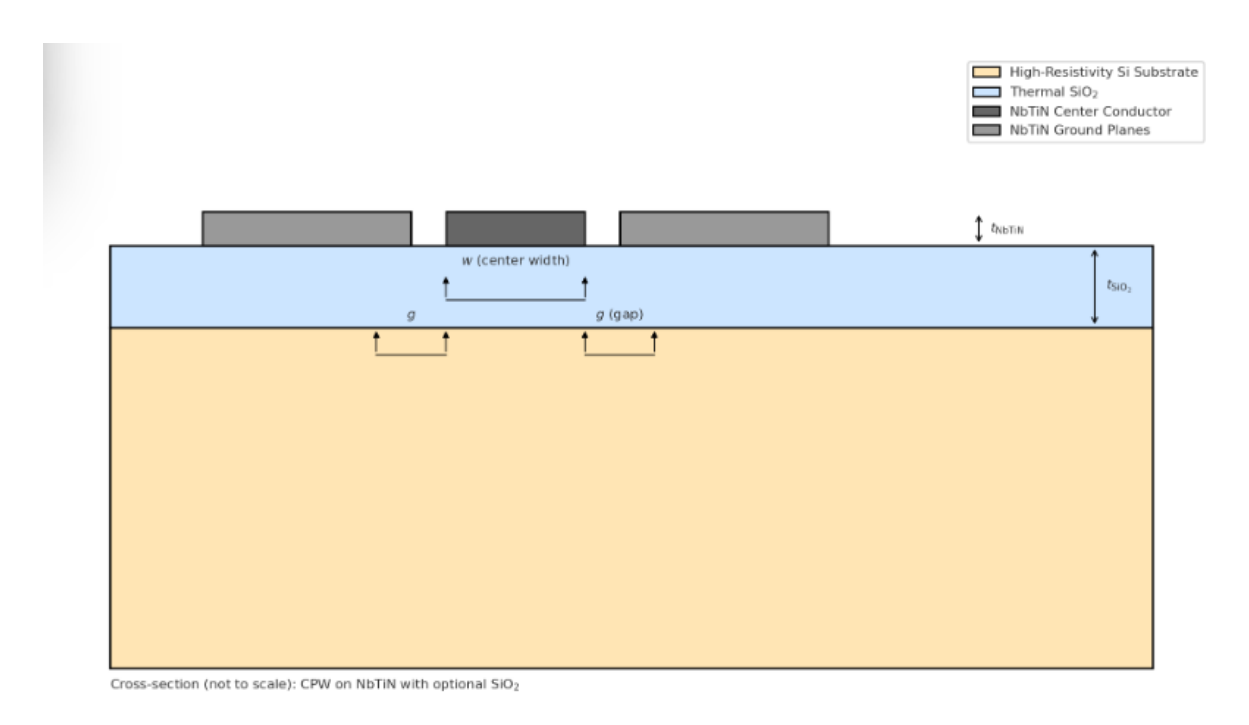


Figure 4.6: Layer scheme of the CPW isolator (cross-section, not to scale). The structure consists of a high-resistivity Si substrate (tan) optionally capped by a thermal SiO₂ layer (light blue) used for electrical isolation and microwave loss control. The superconducting NbTiN film forms the CPW: the central strip (dark gray) of width w is separated from the ground electrodes (light gray) by gaps g. Film and dielectric thicknesses are annotated as $t_{\rm NbTiN}$ and $t_{\rm SiO_2}$. This cross-section represents the local geometry of the spiral CPW used in the parametric isolator sections; periodic widening of the central strip along the spiral (shown in top-view elsewhere) implements the Eom-style dispersion loading that opens stop bands and suppresses $3\omega_p$ pump harmonics. Maintaining tight control of w, g and $t_{\rm NbTiN}$ is essential for the target high impedance and low ripple.

(e.g., ~ 20 nm SiO₂ or Al) patterned by CHF₃/O₂ may be interposed. A brief low-power O₂ clean (10–20 W, ~ 10 s) removes polymers without degrading the superconducting surface.

4.9 Resist Strip with Remover 1165

Following etch, the ZEP mask is removed in Microposit Remover 1165 (NMP-based) at 50–60°C for 20–45 min with gentle agitation; temperatures above 80°C are avoided for safety. If needed, a brief, low-power ultrasonic assist (<1 min) is used with caution to protect narrow gaps. The wafer is then rinsed in IPA and deionized water and dried in N₂. An optional short O₂ plasma (10 W, 10 s) eliminates residual organics while limiting oxide roughness. All handling follows appropriate chemical safety protocols and waste segregation.

4.10 Metrology, Acceptance, and Impact on RF Performance

Dimensional control is verified by SEM on the periodic loading regions to extract mean linewidth w, gap g, corner radius r_c , and line-edge roughness. Film thickness is measured by ellipsometry or X-ray reflectivity (XRR); sheet resistance by four-point probe; T_c by cryogenic probing; and surface

roughness by AFM. From an RF standpoint, edge bowing and corner rounding arising from highcurrent EBL reduce the Fourier strength of the periodic perturbation and narrow or shift the first stop band, while slow variations of w and g introduce weak impedance modulation and ripple. Operating the HS50 in a low-current regime and employing cold development are therefore essential to maximize loading fidelity and minimize in-band reflections.

4.11 Troubleshooting and Run-to-Run Notes

Curved or rounded edges in SEM micrographs indicate excessive beam current; mitigation consists of reducing the aperture current, tightening curve fracturing, stabilizing the stage thermally, and refining proximity-effect correction with distinct groups for arcs and loadings. Resist footing or residue is addressed by marginally extending the cold develop, adding a short O₂ descum, and verifying that the softbake was not excessive. Etch undercut or rough sidewalls are alleviated by lowering RF bias, increasing ICP power to favor chemical etching, and tuning the SF₆:O₂ (or Cl₂:BCl₃) ratio. Loss of pattern after etch motivates either increased ZEP thickness or the adoption of a thin hard mask together with reduced over-etch.

4.12 Run Sheet (example targets)

NbTiN thickness t = 30-50 nm

ZEP 530 thickness h = 180-230 nm @ 5000 rpm, 45 s HS50 beam 50 kV, 100-300 pA (low-current recipe)

Dose (ZEP 530) $180-230 \mu C/cm^2$ (calibrated)

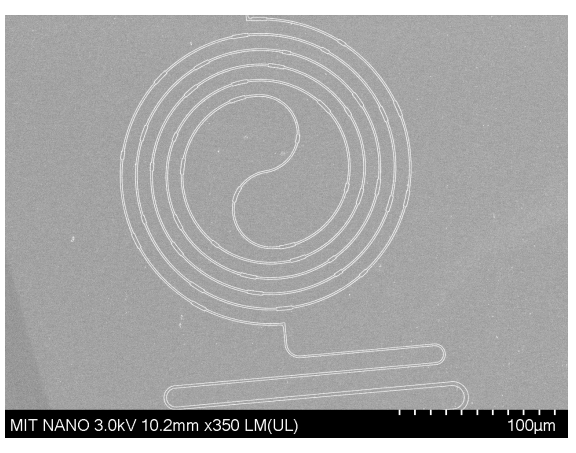
1165 strip 55° C, 30 min + IPA/DI rinse

4.13 Device Micrographs and Layout Notes

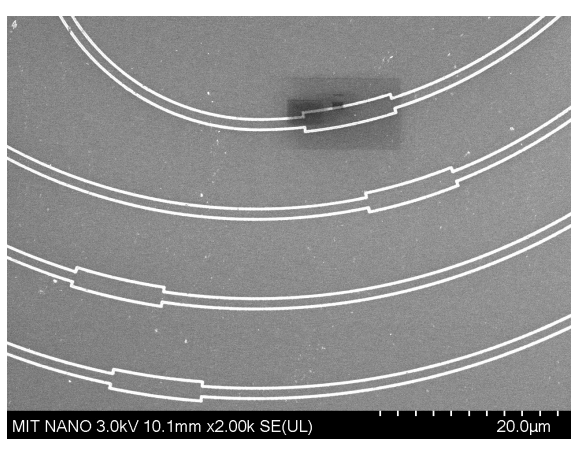
The device is a multi-turn, high-impedance spiral CPW in which the center strip is periodically widened to implement the Eom-style loading that bends dispersion and opens stop-bands aligned to pump harmonics. The loading segments appear as short rectangular bulges repeated along the spiral arcs; at band edges they locally flatten the Bloch dispersion and assist phase matching for three-wave/four-wave mixing.

What the SEMs show. Figure 4.7 summarizes five length scales from the same chip:

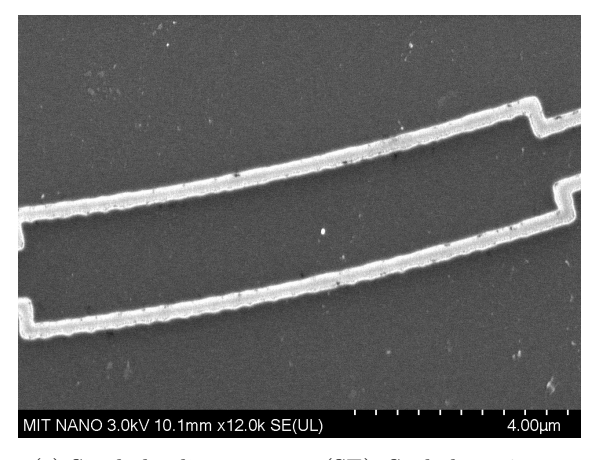
- a global view of the spiral and feed (LM, ×350) showing the compact footprint and uniform angular placement of the periodic loadings;
- intermediate frames (SE, ×2000) where each loading segment is approximately several micrometers long and spaced approximately uniformly in angle;
- close-ups (SE, ×12000–×35000) highlighting sub-micron line widths, edge roughness at the tensof-nanometers scale, and rounded corners at the loading shoulders.



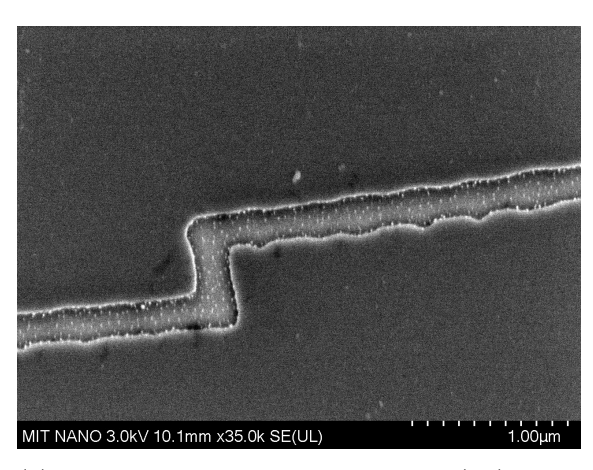
(a) Global view (LM). Scale bar: 100 μ m.



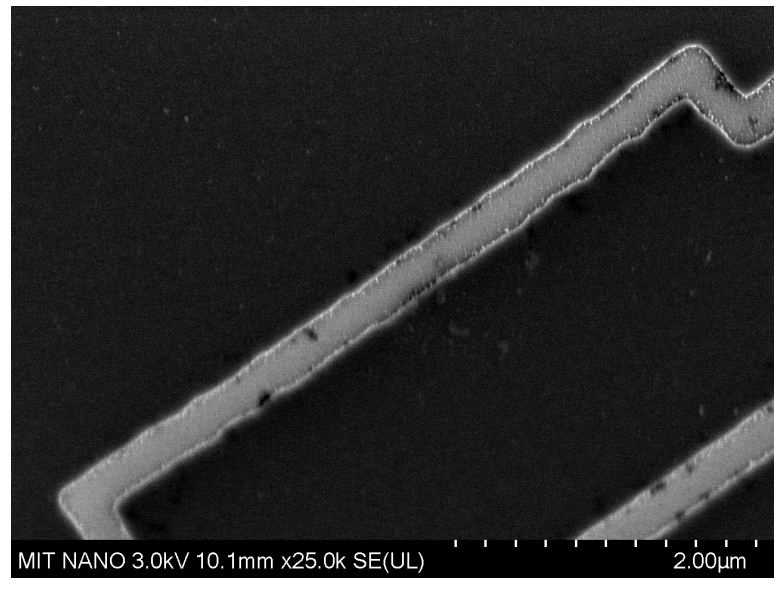
(b) Mid-scale arcs with repeated loadings (SE). Scale bar: 20 $\mu m.$



(c) Single loading segment (SE). Scale bar: 4 $\mu \mathrm{m}.$

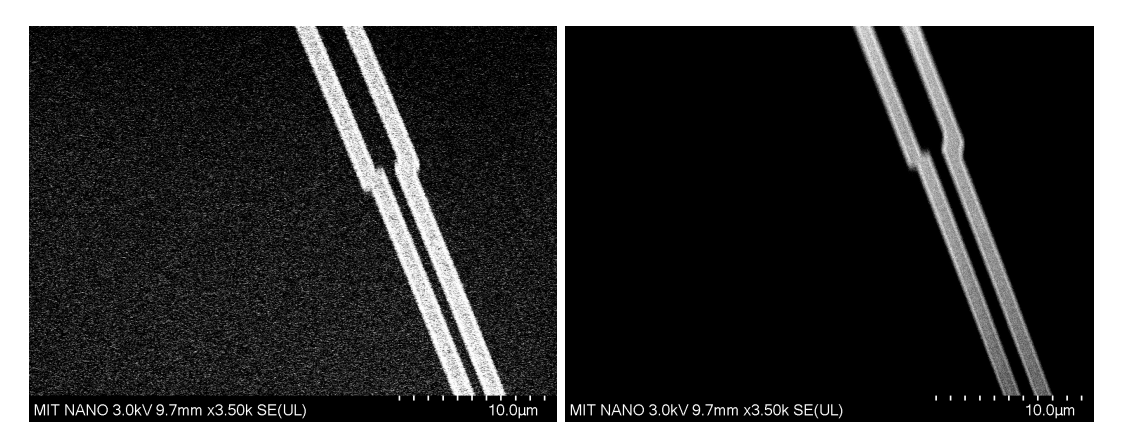


(d) Edge detail with rounded shoulder (SE). Scale bar: 2 $\mu \mathrm{m}.$

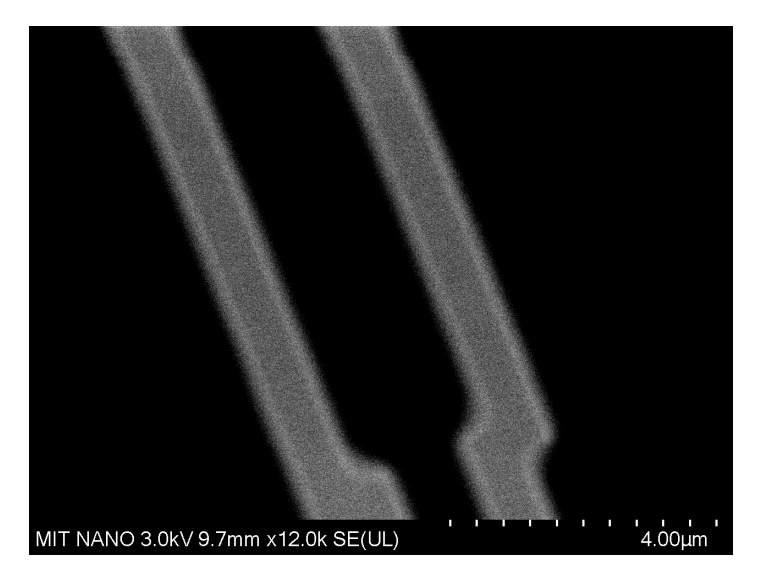


(e) Sub-micron line and corner rounding (SE). Scale bar: 1 $\mu \mathrm{m}.$

Figure 4.7: Spiral CPW with periodic width loadings. The loading pattern repeats along the arcs to engineer the Bloch dispersion and place $3\omega_p$ in a stop band.



Top row: SEM images of improved current device



Bottom row: Same structure under different contrast setting

The slight waviness of edges and the curved/rounded shoulders visible in panels (d–e) are consistent with excessive electron-beam current during EBL. A larger beam current/aperture increases effective spot size and Coulomb-interaction blur, reducing resolution at sub-micron features; corners become rounded, straight segments acquire low-spatial-frequency bowing, and edge roughness increases. In our writes these artifacts explain the small deviations from the ideal rectangular loadings seen along the spiral. They are lithographic in origin and not due to mask CAD.

Reducing the beam current (smaller aperture), increasing step resolution/dwell, enabling proximity-effect correction for dense/curved regions, and tightening stage drift/focus checks typically remove the observed bowing and recover the intended sharp shoulders of the loading segments.

4.14 Klopfenstein Taper Synthesis and Layout

To interface the high-impedance spiral sections with standard 50 Ω environments while keeping inband reflections below a prescribed ripple, we synthesize a Klopfenstein taper and lay it out as a meandered microstrip/CPW using a Python+PHIDL workflow. The procedure is driven by EM data extracted from Sonnet (impedance $Z_0(w)$ and effective permittivity $\varepsilon_{\text{eff}}(w)$ vs. conductor width), and follows the classical optimal profile of Klopfenstein [27].

Given a source impedance $Z_s = 50 \Omega$, a load impedance Z_L (the nanowire/spiral line), and an allowed in-band reflection ripple $R_{\rm dB}$, we compute the continuous optimum impedance profile Z(x) along the (normalized) taper coordinate $x \in [0,1]$. In the code, the routine bklop(Z0, Zload, N, R_dB) discretizes this into N sections by evaluating

$$\gamma_0 = \frac{1}{2} \ln \frac{Z_L}{Z_s}, \quad \gamma_m = 10^{R_{dB}/20}, \quad A = \operatorname{arcosh}\left(\frac{\gamma_0}{\gamma_m}\right),$$
(4.1)

and building Z(x) from the closed-form integral in Klopfenstein's Eq. (14). The result is the vector

$$\mathbf{Z} = [Z_{s}, Z_{1}, Z_{2}, \dots, Z_{N}, Z_{L}],$$
 (4.2)

with optimum electrical length $L_{\rm opt} \approx 0.565 \,\lambda_0$ at the design frequency.

The Klopfenstein profile is electrical; to obtain geometry we need a monotone mapping $Z \mapsto w$ and $Z \mapsto n_{\text{eff}} = \sqrt{\varepsilon_{\text{eff}}}$. We import Sonnet CSVs (GraphZ0.csv, GraphE0.csv) and build shape-preserving interpolants (PchipInterpolator) for

$$w = f_Z(Z_0), n_{\text{eff}} = f_n(Z_0), (4.3)$$

so each section Z_k is assigned a width $w_k = f_Z(Z_k)$ and local index $n_k = f_n(Z_k)$. This ensures that fabricated widths reproduce the EM impedance actually simulated on our stack.

The electrical length L_{opt} is split into N physical segments of length

$$\Delta \ell_k = \frac{(0.565 \,\lambda_0)/N}{n_k},\tag{4.4}$$

so that the correct phase advance is preserved under dispersion. To compact the footprint, straight segments alternate with arcs. The local bend radius is tied to feature size to control current crowding and etch bias,

$$r_k = \kappa \left(w_k + 2g \right), \qquad \kappa \in [1.5, 3], \tag{4.5}$$

with larger r_k auto-selected for wider sections. The script writes the centerlines and the two edges (x2,y2 and x3,y3) of the strip, adds short quarter-turn "pigtails" at the ends, and saves coordinates to Taper.mat.

The function $microstrip_taper()$ reconstructs polygons from the saved edge traces, chops the path every N=200 points for safe Booleans, and emits a single-layer taper cell with labeled ports (narrow, wide). A quick visual check of the final meander is shown in Fig. 4.8. The same geometry can be exported to GDSII and re-imported in Sonnet for a closed layout-EM loop.

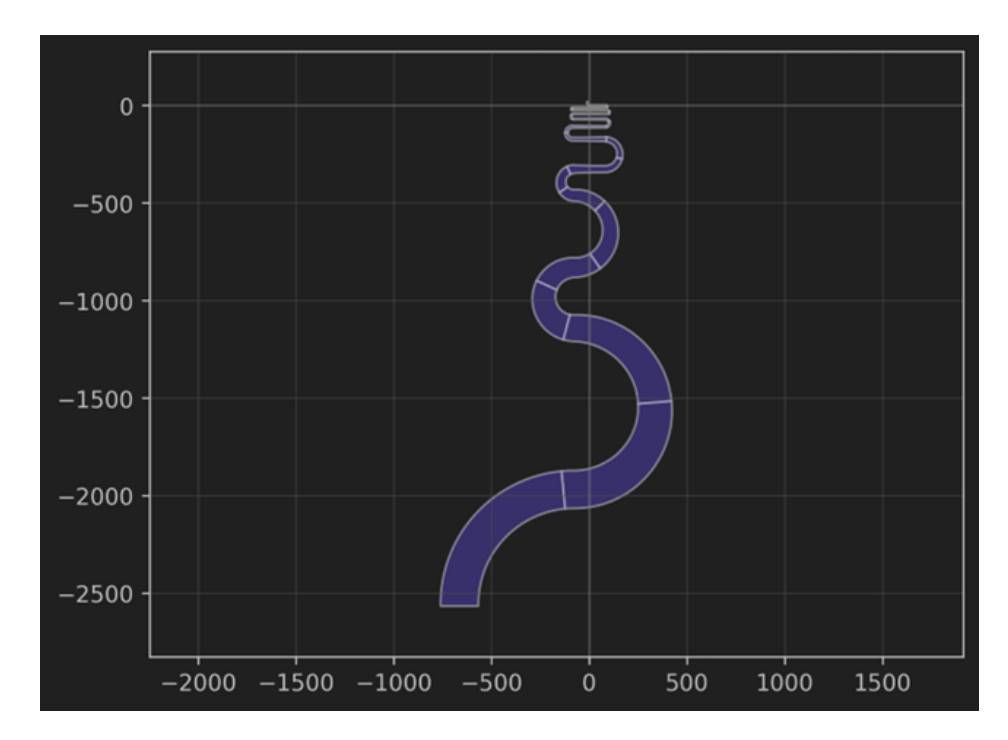


Figure 4.8: Klopfenstein taper layout preview (PHIDL). The meandered transformer follows the impedance profile from the nanowire load to 50 Ω with section lengths adjusted by $n_{\text{eff}}(w)$. Straight runs alternate with controlled-radius arcs $r_k = \kappa(w_k + 2g)$ to limit current crowding and preserve lithographic fidelity.

For validation we use two complementary calculations. First, a cascaded TL model with section impedances Z_k and lengths $\Delta \ell_k$ provides the input impedance $Z_{\rm in}(f)$ via the standard formula

$$Z_{\rm in} = Z_k \frac{Z_{k-1} + Z_k \tanh(\gamma_k \Delta \ell_k)}{Z_k + Z_{k-1} \tanh(\gamma_k \Delta \ell_k)}, \tag{4.6}$$

vectorized across frequency (function tr1), from which the return loss $RL = 20 \log_{10} \left| \frac{Z_{\rm in} - 50}{Z_{\rm in} + 50} \right|$ is plotted by rlplot/bplot. Second, a Sonnet model of the actual meandered polygon confirms the broadband match and reveals any parasitic coupling between turns. Figure 4.9 shows the computed return loss for the synthesized transformer with $R_{\rm dB} = -30$ dB: beyond a few gigahertz the reflection stays well below the ripple bound and monotonically improves with frequency, as expected for Klopfenstein tapers.

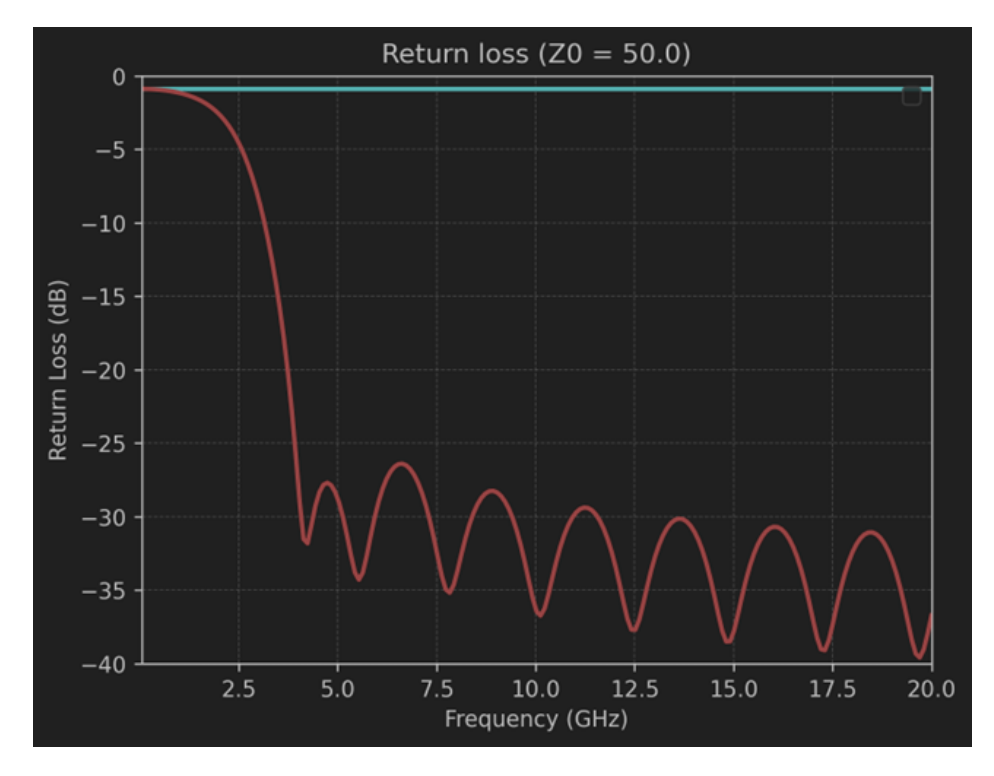


Figure 4.9: Return-loss of the synthesized taper. TL cascade using the Klopfenstein section list (red) versus the reference 50 Ω (cyan baseline). The in-band ripple adheres to the design target $R_{\rm dB}$ and the high-frequency match improves as the effective electrical length grows.

Because the taper spans widths from sub-micron to several microns, bends at the narrow end are the resolution limit for EBL. We therefore (i) keep $\kappa \gtrsim 2$ for $w \lesssim 1~\mu\text{m}$, (ii) fracture arcs with $\leq 10~\text{nm}$ chord error, and (iii) use the low-current HS50 recipe and cold ZEP development (Sec. 4.6, 4.7). After etch, we verify the profile by extracting (w,g) along the meander and re-running the TL cascade with measured widths; agreement with Fig. 4.9 is a strong indicator that the fabricated transformer meets the ripple spec.

This taper methodology yields a compact, fabrication-aware transformer whose impedance law is anchored to Sonnet EM data rather than closed-form CPW formulas, ensuring that the realized geometry delivers the intended RF match when integrated with the parametric isolator sections.

4.15 Results and Discussion

This section presents the numerical and circuit-level simulations of the proposed superconducting parametric isolator. The results are organized to highlight, in sequence, the impact of (i) frequency selection, (ii) structural apodization introduced through an additional loading element, (iii) comparison between the source and idler frequency responses, and (iv) performance optimization via bias current and line length tuning. Each group of figures corresponds to a specific design iteration, progressively improving isolation, bandwidth, and spectral symmetry.

4.15.1 Frequency Selection and Resonant Shape Evolution

Figures 4.10 and 4.11 illustrate the first parametric analysis comparing operation at 11 GHz and 12 GHz. A distinct evolution of the transfer function shape can be observed: as the frequency increases, the isolation dip associated with the phase-matched interaction deepens and shifts upward

in frequency. At 11 GHz, the main rejection band is relatively narrow, corresponding to weaker three-wave mixing efficiency. At 12 GHz, the stronger coupling and enhanced nonlinear phase shift result in a wider and more defined attenuation window, accompanied by a smoother passband away from resonance. This confirms the sensitivity of the isolator response to the operating frequency and its tunability around the designed parametric point.

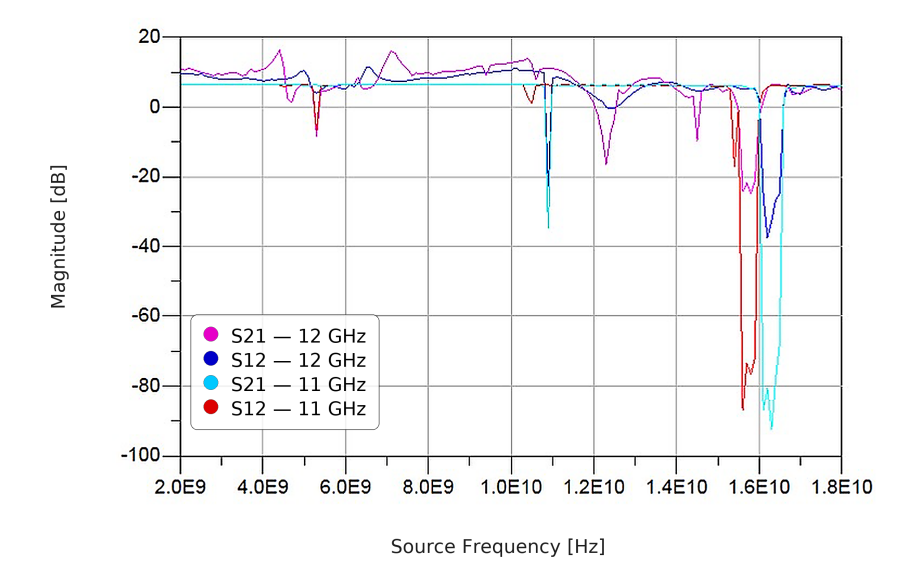


Figure 4.10: Frequency response comparison between 11 GHz and 12 GHz operation. The legend in the plot indicates the mapping between S_{21}/S_{12} and the traces. The deeper attenuation at 12 GHz indicates stronger parametric coupling.

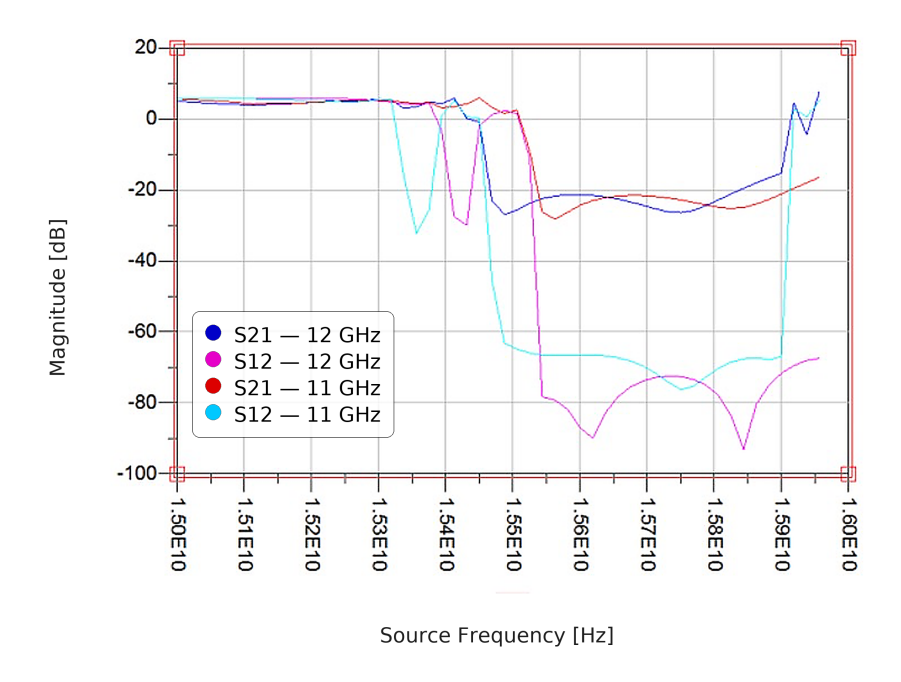


Figure 4.11: Zoomed view emphasizing the evolution of the isolation dip as the operating frequency increases from 11 GHz to 12 GHz (apodized spiral).

4.15.2 Effect of Apodization via a Third Loading Structure

The next design stage investigated the role of structural apodization achieved by introducing a third periodic loading section with dimensions differing from the primary unit cell. Rather than continuously tapering impedance, this method discretely modulates the local dispersion through alternating loading geometries, thereby suppressing standing-wave resonances and flattening the isolation profile. Figures 4.12–4.14 illustrate successive implementations with different loading strengths. The addition of the third loading feature reduces unwanted Fabry–Pérot–type ripples in the transmission band and redistributes higher-order stopbands. As the contrast between the three loaded sections increases, the passband becomes smoother and the isolation notch more symmetric, indicating improved phase uniformity and reduced reflection within the transmission line.

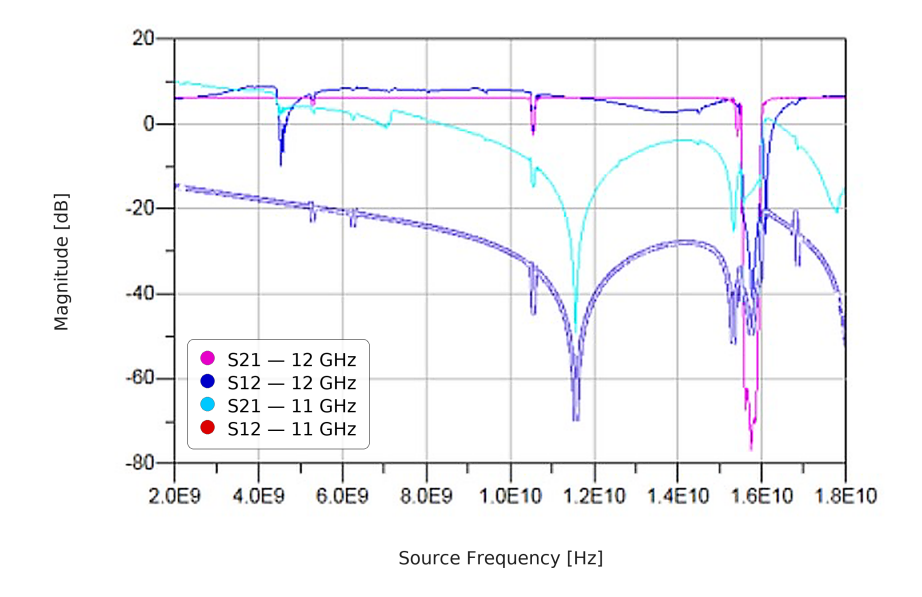


Figure 4.12: Initial apodized configuration with a weakly coupled third loading element, showing partial suppression of spectral ripple. See the in-plot legend for S_{21}/S_{12} .

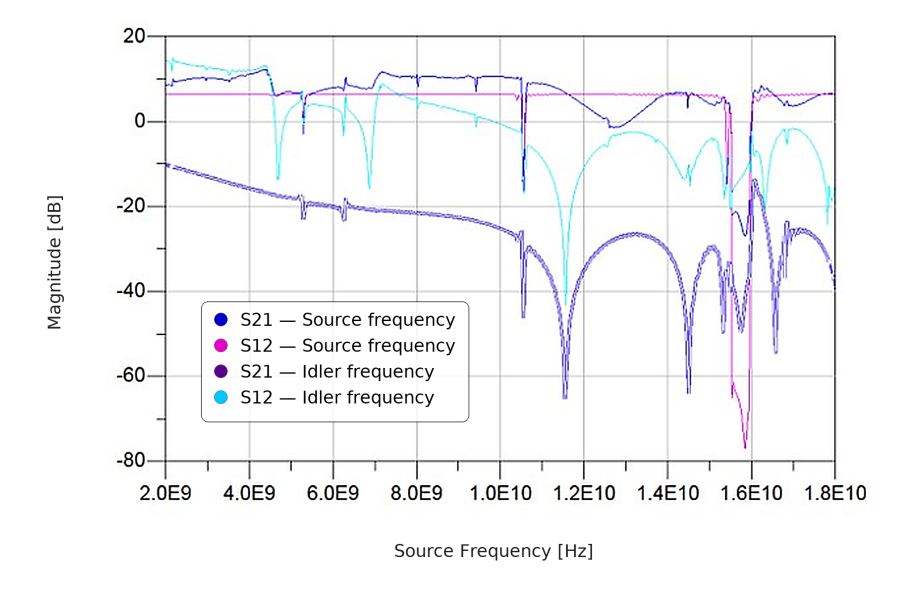


Figure 4.13: Enhanced apodization: the third loading structure more effectively suppresses secondary resonances. See the in-plot legend for S_{21}/S_{12} .

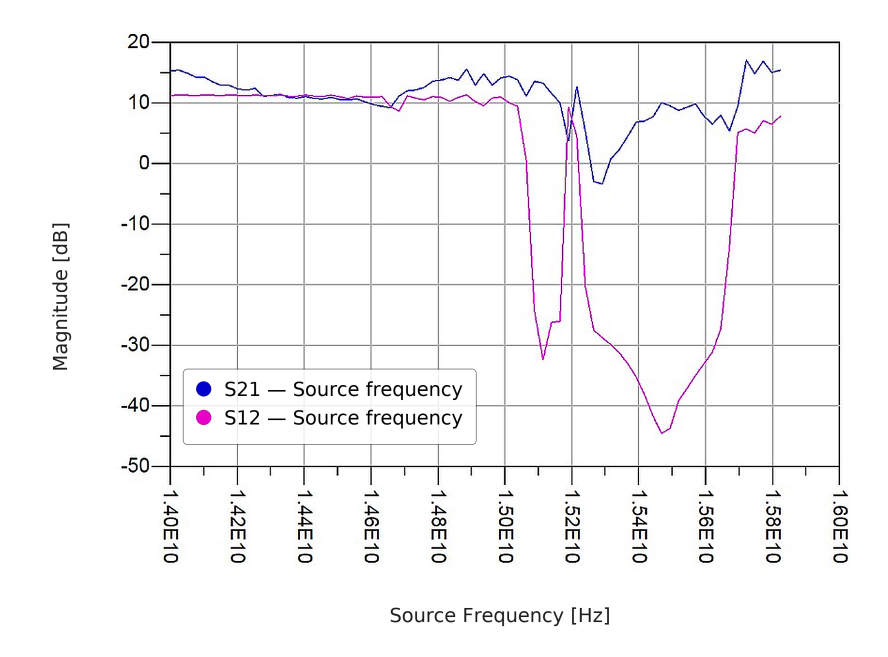


Figure 4.14: Optimized apodization: the composite loading sequence yields a flat transmission baseline and a well-defined isolation dip. See the in-plot legend for S_{21}/S_{12} .

4.15.3 Evaluation of Idler versus Source Frequency Response

Figures 4.12 and 4.13 also report the simulated scattering parameters at both the source and idler frequencies. The idler response appears frequency-shifted with respect to the source response, evidencing the parametric frequency conversion intrinsic to three-wave mixing. The observed asymmetry between S_{12} and S_{21} across the two frequency bands confirms the intended nonreciprocal behavior. Notably, the isolation achieved at the source frequency is not compromised by the idler, which is influenced by the amount of DC current implemented in the system.

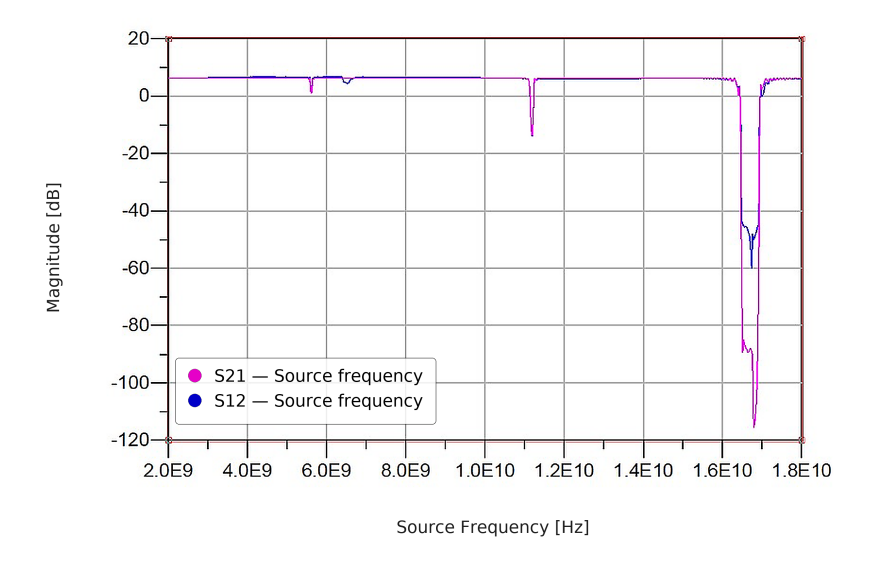


Figure 4.15: Comparison of S_{21} and S_{12} at source and idler frequencies.

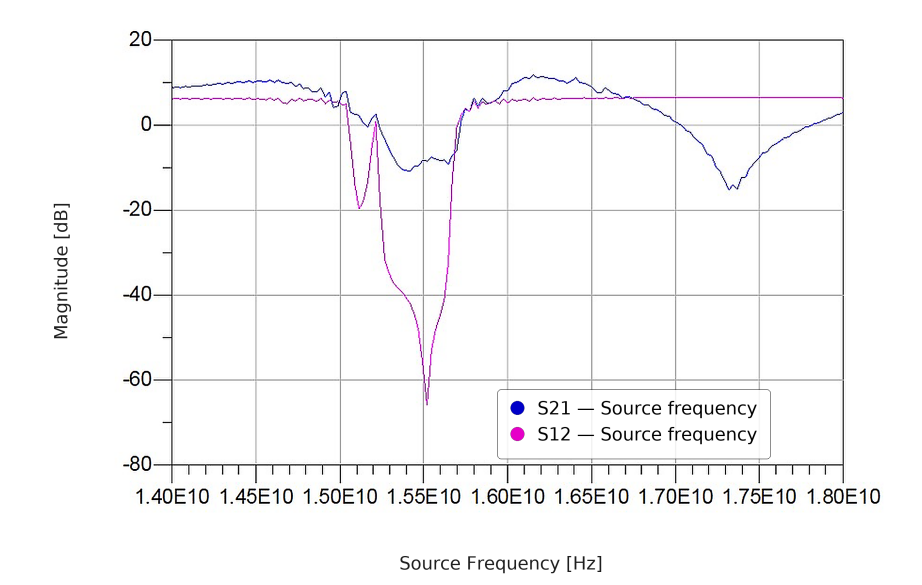


Figure 4.16: Simulated response under identical conditions showing persistent nonreciprocity between the two mixing sidebands.

4.15.4 Optimization through Bias Current and Line Length

The final optimization step focused on adjusting the DC bias current and the effective propagation length to fine-tune the phase-matching condition. The bias current modulates the kinetic inductance of the superconducting film, altering the nonlinear coupling strength, while the line length controls the interaction region where phase accumulation occurs. Increasing the current enhances the parametric modulation depth, whereas extending the line length improves isolation uniformity but may slightly increase insertion loss. Figures 4.15 and 4.16 demonstrate how these parameters jointly determine the achievable isolation and bandwidth. The optimized configuration exhibits deep attenuation (> 60 dB) and a broadened passband with minimal ripple, validating the combined tuning strategy.

4.16 I_c testing

The spiral device under test was mounted in a cryogenic probe station and biased with a quasi-DC current ramp, delivered through low-noise current sources. Voltage taps at the input and output contacts allowed for the simultaneous measurement of the current-voltage (I-V) characteristics. The sample was thermally anchored to the cold stage of the cryostat at $T \ll T_c$, ensuring that the film operated in the superconducting regime under negligible thermal fluctuations.

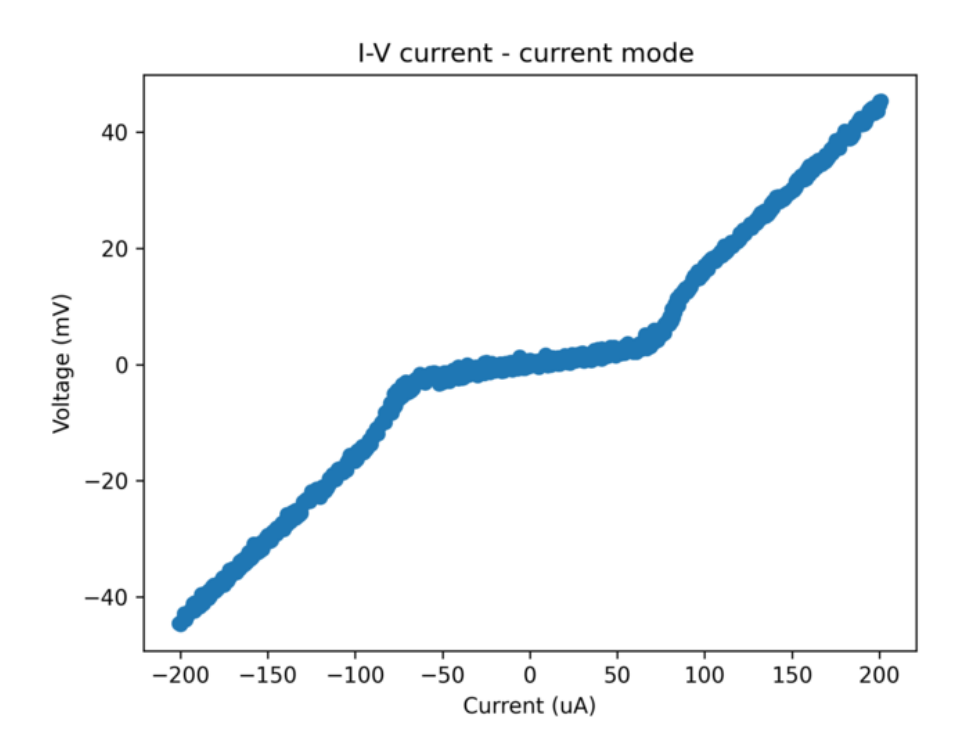


Figure 4.17: Current-voltage characteristic of the spiral

4.17 Measurement Principle

The I-V curve of the spiral exhibits a characteristic superconducting plateau at zero voltage up to the point where the applied bias current reaches the critical current I_c . Beyond this threshold, the superconducting state collapses, producing a sharp onset of voltage that indicates the transition into the resistive regime. This behavior is illustrated in Figure 4.17, where the voltage remains zero until the critical current is reached, at which point a finite resistance develops.

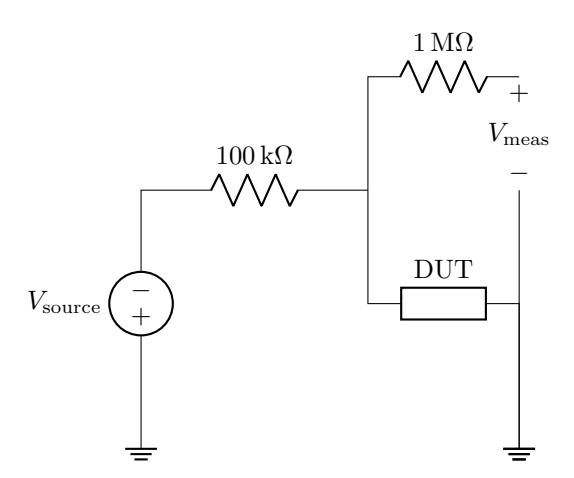


Figure 4.18: Current-voltage characteristic of the spiral

The extracted I_c is a function not only of the intrinsic material parameters (such as the London penetration depth λ_L , the coherence length ξ , and the density of states at the Fermi level N_0) but

also of the geometric configuration of the spiral (conductor width w, thickness t, and total length). For films where $w < \lambda^2/t$ and $t < \lambda_L$, the scaling current I^* , which controls the nonlinearity of the kinetic inductance, can be estimated by equating kinetic and condensation energies [1], [15]:

$$I^* \approx wt \sqrt{\frac{N_0 \Delta^2}{\mu_0 \lambda_L^2}},\tag{4.7}$$

where Δ is the superconducting gap. In practice, I_c is typically a fraction of I^* due to current crowding, edge roughness, and vortex entry at geometric inhomogeneities.

4.18 Results and Discussion

The experimental measurement for the spiral presented in Figure 4.17 confirms this general behavior. The curve shows a sharp transition at the extracted I_c , which is in agreement with estimates based on film thickness and width. This value directly informs the design margins of devices relying on kinetic inductance nonlinearity: operating currents are typically set well below I_c to avoid premature switching, while ensuring sufficient nonlinearity to achieve the desired parametric gain.

4.19 Implications for Spiral-Based Devices

For spiral-based parametric amplifiers, the knowledge of I_c allows calibration of the nonlinear kinetic inductance coefficient, which enters the coupled mode equations describing three-wave and four-wave mixing processes [1], [21]. Furthermore, in the context of quantum-limited amplification, ensuring device operation at currents below I_c while retaining adequate nonlinearity is crucial to suppress excess noise and to achieve reproducible gain profiles. The spiral geometry, by virtue of its compactness and distributed inductance, provides a robust platform for sustaining large currents without premature switching, but the measured I_c remains the ultimate constraint.

In summary, the critical current measurement provides a direct, experimentally grounded metric of the superconducting performance of the spiral. This information is essential both for validating material properties (such as NbN or NbTiN thin films) and for guiding the design of superconducting devices where kinetic inductance is exploited as a nonlinear medium.

CHAPTER 5

Circulator

A circulator is a nonreciprocal multiport device that routes electromagnetic signals directionally between its terminals in a cyclic sequence, typically from port 1 to 2, port 2 to 3, and port 3 to 1. In its canonical form, nonreciprocity arises from time-reversal symmetry breaking induced by magneto-optic effects in ferrite media under a static magnetic bias. Such magnetically biased circulators have long been indispensable components in cryogenic microwave networks, where they isolate sensitive quantum devices from reflected noise and allow for multiplexed signal routing. However, their size, magnetic field requirements, and incompatibility with on-chip superconducting circuitry motivate the development of compact, magnet-free alternatives.

The objective of this chapter is to propose a possible on-chip implementation of a superconducting circulator, conceived as a natural extension and application of the magnet-free isolator previously discussed. In particular, the architecture leverages the forward coupler introduced by Colangelo *et al.* as a key building block to enable directional signal routing among multiple ports without relying on magnetic biasing.

The circulator design presented here overcomes the limitations of conventional ferrite-based devices by breaking time-reversal symmetry through parametric modulation of circuit elements, specifically exploiting the current-dependent kinetic inductance of superconducting thin films. The device architecture comprises three primary functional modules arranged in a topology that enables unidirectional signal flow among four ports. Two parametric isolators, each providing directional transmission between specific port pairs, are interconnected through a central directional coupler exhibiting inherent forward-transmission properties. This modular design strategy simplifies optimization while achieving high isolation and low insertion loss, offering performance comparable to monolithic Josephson-junction-based nonreciprocal devices without requiring magnetic biasing.

5.1 System Architecture and Integration

5.1.1 Four-Port Circulator Topology

The complete circulator system is realized through strategic interconnection of two parametric isolators and one directional coupler, arranged in a topology enabling unidirectional signal circulation among four external ports. The first parametric isolator, implemented as a superconducting spiral transmission line with integrated bias and pump injection, provides unidirectional transmission from external port 1 to an internal node connected to the directional coupler. Similarly, the second parametric isolator enables unidirectional transmission from another internal node to external port 3.

The central directional coupler, implemented using side-coupled superconducting nanowires following design principles established by Colangelo et al. [5], exhibits a unique scattering matrix structure

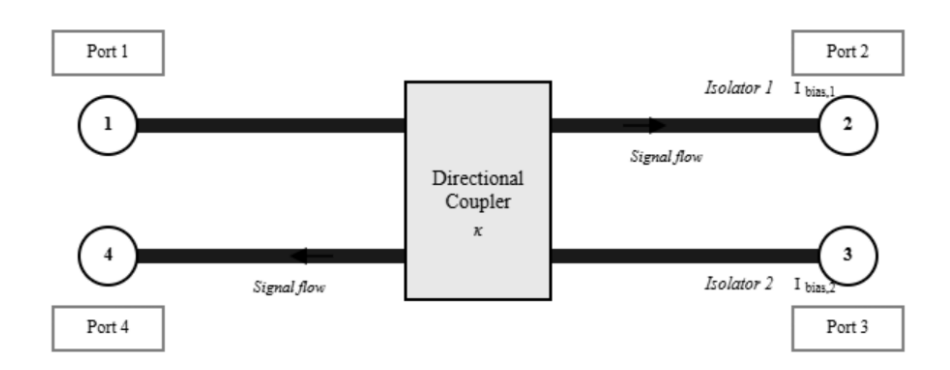


Figure 5.1: Proposed circulator scheme

characterized by forward-coupling terms only. Specifically, the coupler supports signal transmission from port 1 to ports 2 and 4, from port 2 to port 3, from port 3 to ports 2 and 4, and from port 4 to port 1, while providing inherent isolation between ports 1 and 3, as well as between ports 2 and 4. This forward-only coupling characteristic results directly from the distributed coupling mechanism in the side-coupled nanowire geometry.

5.1.2 Scattering Matrix Formulation

The overall scattering behavior of the four-port circulator can be described by a 4×4 scattering matrix \mathbf{S}_{circ} relating the complex amplitudes of outgoing waves to incoming waves at each port. For ideal circulator operation with unidirectional circulation following the path $1 \to 2 \to 3 \to 4 \to 1$, the scattering matrix assumes the form where $S_{21} = S_{32} = S_{43} = S_{14} = 1$, while all other elements equal zero. This ideal scattering matrix represents perfect transmission along the circulation path with complete isolation for all other paths.

In practical implementations, scattering matrix elements deviate from ideal values due to finite isolation in parametric isolators, non-ideal coupling ratios in the directional coupler, and impedance mismatches at component interfaces. The actual scattering parameters can be computed by cascading individual component scattering matrices, accounting for phase accumulation in connecting transmission lines.

5.2 Component Implementation Details

5.2.1 Parametric Isolator Design

The parametric isolators are implemented using superconducting spiral transmission lines fabricated from niobium titanium nitride thin films with typical thickness of 35 to 50 nm. The spiral geometry is chosen to maximize total inductance while maintaining compact footprint, with typical dimensions resulting in total line length of approximately 0.8 m wound in a double-spiral configuration to minimize parasitic coupling and spurious resonances. The center conductor width and gap dimensions are optimized to achieve characteristic impedance in the range of 150 to 300 Ω , significantly higher than conventional 50 Ω systems due to enhanced kinetic inductance contribution.

The kinetic inductance per unit length for NbTiN transmission lines is approximately 800 pH/ \square , resulting in total inductance on the order of 50 μ H for the complete spiral structure. This high inductance, combined with distributed transmission line capacitance, establishes the device operating frequency range, with typical center frequencies in the range of 4 to 6 GHz. The quality factor of

spiral resonators can exceed 1000 at millikelvin temperatures, enabling efficient parametric processes with modest pump powers.

5.2.2 High-Impedance Directional Coupler Theory

The directional coupler employed in this circulator (5.2) design is based on the high-impedance superconducting nanowire forward coupler developed by Colangelo et al. [5]. This device exploits unique properties of high kinetic inductance superconductors to achieve forward coupling in an extremely compact footprint, addressing the critical challenge of miniaturizing microwave components for scalable quantum computing systems.

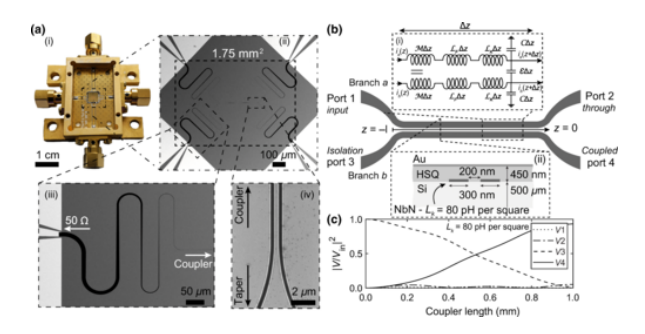


Figure 5.2: Superconducting-nanowire directional forward coupler. (a-i) Device chip mounted in the RF test package; (a-ii) SEM of the complete four-port device before deposition of the dielectric spacer and top ground; (a-iii) close-up of the impedance-matching taper; (a-iv) detail of the coupled nanowire lines. (b) Geometry and analytical model: two nanowire transmission lines coupled over a length l, represented as a coupled-LC ladder network with geometric inductance \mathcal{L}_F , kinetic inductance \mathcal{L}_k , capacitance \mathcal{C} , coupling capacitance \mathcal{C} , and mutual inductance \mathcal{M} . (c) Simulated port voltages along the coupler at 5 GHz showing 50:50 forward coupling for $L_k = 80 \text{ pH/sq}$. Reproduced from [5].

Forward Coupler Operating Principle

A forward directional coupler is a coupled-line structure whose coupled signal emerges at the forward port, i.e., the port located at the same physical end as the input through port. This behavior contrasts with conventional backward couplers, where the coupled power appears at the opposite end. In the literature the same class of devices is frequently described as "forward-wave" or "transdirectional" coupled-line couplers [5].

Two parallel transmission lines support even and odd quasi-TEM modes with distinct effective permittivities. The forward coupler approach achieves high directivity by selectively loading the odd mode along the entire coupled section so that the modal phase velocities closely match, i.e.,

$$\Delta\beta(f) \equiv \beta_o(f) - \beta_e(f) \to 0. \tag{5.1}$$

Odd-mode-selective loading is realized by periodically inserting reactive unit cells across or beneath the inter-line gap in a way that perturbs the odd mode far more strongly than the even mode. Interline periodic shunt capacitors or bridges concentrate their effect under odd-mode excitation due to the large differential voltage between the strips, with minimal influence on the even mode. Alternative implementations place patterned or via-connected ground cells beneath the gap—such as mushroom, patterned-ground, or Y-/H-shaped via structures—which increase the odd-mode effective permittivity and provide control over the even/odd phase difference across frequency.

In addition to distributed modal loading, accurate treatment of the end discontinuities at the terminations of the coupled section is required to achieve the intended interference condition. The forward coupled port must experience constructive interference while the isolated port experiences destructive interference; this is enforced by trimming end-step capacitances and any residual $\Delta\beta$ using established microstrip compensation techniques.

When the structure is properly synthesized and compensated, the input and through ports are matched, the designed coupling level appears at the forward coupled port rather than the opposite end, and the isolated port exhibits a deep null ((5.3)). The attainable directivity is governed primarily by the quality of even/odd velocity equalization over frequency and the accuracy with which end discontinuities are modeled and compensated.

For a target system impedance Z_0 and linear coupling factor k, an ideal, lossless, quarter-wave coupled-line section has even and odd characteristic impedances

$$Z_{0e} = Z_0 \sqrt{\frac{1+k}{1-k}}, \qquad Z_{0o} = Z_0 \sqrt{\frac{1-k}{1+k}}.$$
 (5.2)

In microstrip, satisfying these impedance targets alone does not guarantee high directivity because $\beta_e \neq \beta_o$ even when the structure is impedance-matched. The forward-coupler strategy augments the conventional width/spacing synthesis with periodic odd-mode-selective loading so that both impedance and phase requirements are met: $\Delta\beta(f)$ is flattened around zero across the design band, and the end phasing is tuned for forward constructive interference and an isolated-port null.

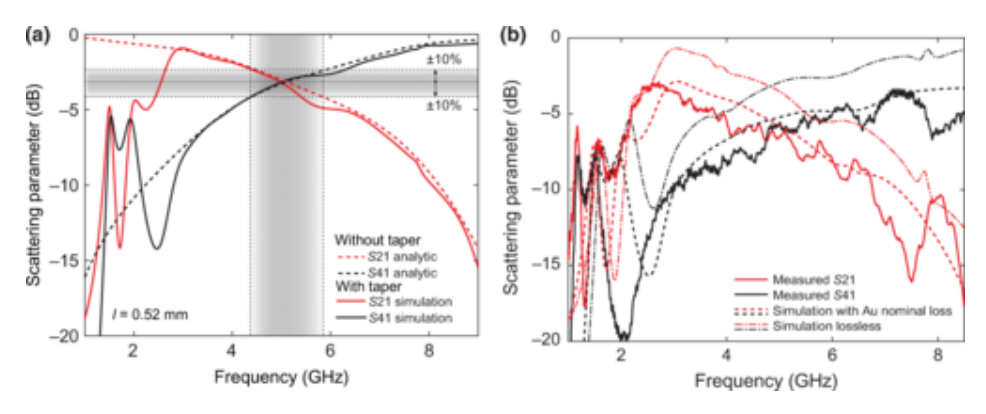


Figure 5.3: Microwave response of the superconducting-nanowire directional forward coupler. (a) Analytical modeling of the coupling section (without taper) and simulation of the impedance-matched configuration. Above 3 GHz, the curves coincide, indicating that the impedance-matching taper connecting the high-impedance section to the $50~\Omega$ RF interface does not affect the coupling behavior. The 10% bandwidth spans 4.4–5.8 GHz. (b) Measured microwave response of the fabricated device at 1.3 K compared with simulations corrected for fabrication nonidealities and including normal-metal losses from the Au ground plane and CPW feedlines. Balanced forward coupling is observed at 4.75 GHz. Reproduced from [5].

Coupled-Line Architecture and Mode Analysis

The coupler follows traditional coupled-line architecture where two superconducting nanowires are brought together for coupling length l. The structure can be modeled as a coupled LC ladder, with explicit separation of kinetic inductance contribution (L_k) from geometric (Faraday) contribution (L_F) to total line inductance per unit length. Coupling between the two lines produces mode splitting into common (c) and differential (π) modes, with different effective indices and propagation constants β_c and β_{π} .

In this coupled transmission line system, a sinusoidal signal with frequency ω propagates as a superposition of these eigenmodes, with energy continuously transferred between the two lines with periodicity:

$$l_{\pi} = \frac{\pi}{\Delta \beta} = \frac{\pi}{\beta_{\pi} - \beta_{c}} \tag{5.3}$$

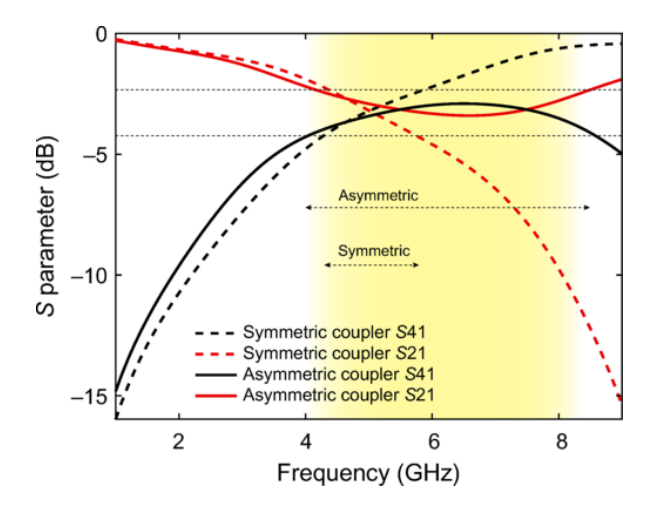


Figure 5.4: Transmission and coupling S-parameters for symmetric and asymmetric coupler designs. The asymmetric configuration extends the operational bandwidth while maintaining comparable coupling efficiency, achieving a broader frequency range than the symmetric case. Reproduced from [5].

A coupled transmission line section with length that is an odd-integer multiple of $l_{\pi}/2$ can perform, ideally, 3 dB forward coupling at the design frequency. The key innovation of the Colangelo design is that the combination of high kinetic inductance lines, high coupling capacitance, and low loss significantly boosts mode splitting:

$$[H]\Delta\beta \propto \sqrt{L_k C} \sqrt{1 + 2C/C}$$
 (5.4)

where C and C are the self- and coupling capacitance per unit length, respectively. This enhanced mode splitting allows forward coupling to be achieved in a dramatically reduced footprint compared to conventional conductor implementations.

5.2.3 Directional Coupler Implementation

The directional coupler in the four-port circulator utilizes the forward-coupling design principles (??) to achieve forward-only coupling characteristics. The coupler consists of four ports arranged in a topology where selective coupling is achieved through precise coupling length of 520 μ m. At the operating frequency of 4.753 GHz, the measured coupling coefficient is -6.7 dB, corresponding to approximately 50% power transfer between coupled ports.

The inherent directionality arises from the forward-coupling nature of the side-coupled nanowire geometry. Unlike conventional backward couplers relying on impedance differences between eigenmodes, this forward coupler transfers energy through distributed coupling along the interaction length. Isolation between non-coupled ports exceeds 30 dB due to the absence of direct electromagnetic coupling paths in the device geometry, making it ideal for circulator applications requiring high isolation.

Coupler Tunability

A unique feature of the high-impedance nanowire coupler is its tunability through kinetic inductance modulation. The nonlinear dependence of kinetic inductance on current density and temperature enables dynamic control of coupling characteristics. The kinetic inductance varies with temperature according to:

$$L_k(T) = L_k(0) \left[1 + \left(\frac{T}{T_c} \right)^n \right]$$
 (5.5)

where T_c is the critical temperature. Similarly, DC bias current application modifies kinetic inductance through:

$$L_k(I) = L_k(0) \left[1 + \left(\frac{I}{I^*} \right)^2 \right] \tag{5.6}$$

This tunability allows post-fabrication optimization of coupling ratios and compensation for fabrication variations. By varying base temperature or applying DC bias current, the coupling coefficient can be adjusted over several dB range, providing operational flexibility. This feature is particularly valuable for quantum computing applications where precise signal routing control is essential.

5.3 Operational Analysis and Performance

5.3.1 Signal Flow and Circulation Mechanism

Four-port circulator operation can be understood by tracing the signal path for a microwave signal entering at port 1. The signal first encounters the first parametric isolator, providing low-loss transmission in the forward direction while strongly attenuating backward-propagating components. Forward transmission through the isolator is characterized by transmission coefficient magnitude approaching unity, with typical insertion loss values below 0.3 dB in the passband.

Upon exiting the first isolator, the signal enters the directional coupler at its first port. Due to forward-only coupling characteristics, the signal is routed to port 2 with nominal 3 dB coupling loss. From coupler port 2, corresponding to external circulator port 2, the signal can be extracted or allowed to continue circulation by re-entering the coupler. The inherent coupler directionality ensures that signals at port 2 are coupled only to port 3, maintaining unidirectional circulation.

The signal entering coupler port 3 is then directed to the second parametric isolator, providing unidirectional transmission to external circulator port 3. The circulation path is completed through the coupler's port 4 to port 1 connection, allowing signal return to the starting point with total round-trip loss determined by the sum of individual component losses.

Reverse direction isolation between ports is achieved through three distinct mechanisms. First, parametric isolators provide intrinsic isolation exceeding 20 dB for backward-propagating signals due to destructive interference between directly transmitted and frequency-converted components. Second, the directional coupler contributes structural isolation exceeding 30 dB between non-coupled port pairs due to the absence of direct coupling paths. Third, synchronized system pumping introduces additional phase-dependent isolation through parametric processes.

The total circulator isolation typically exceeds 35 dB across the operating bandwidth, with peak isolation values approaching 40 dB at center frequency. The isolation bandwidth, defined as the frequency range over which isolation exceeds 20 dB, is primarily determined by parametric isolator bandwidth and typically spans 400 to 600 MHz for implemented devices.

The operational bandwidth is determined by the interplay between spiral transmission line resonant characteristics and frequency-dependent coupling in the directional coupler. The 3 dB bandwidth, within which insertion loss remains below 3 dB relative to minimum loss point, typically spans 500 MHz centered at design frequency. This bandwidth can be extended through impedance matching networks and dispersion engineering techniques.

A unique advantage of the parametric approach is the ability to tune operating frequency and isolation characteristics through DC bias current adjustment. By varying bias current from 0 to $50~\mu\text{A}$, the center frequency can be shifted by up to 500 MHz due to kinetic inductance change. This tunability enables dynamic circulator performance optimization and compensation for fabrication variations or environmental changes.

5.4 Theoretical Performance Limits

Maximum achievable isolation in a parametric circulator is fundamentally limited by the modulation depth achievable without driving the system into instability or excessive nonlinearity. For the current-driven modulation scheme employed in this design, modulation depth is proportional to the product of DC bias current and AC pump amplitude, normalized by the characteristic current scale. Practical considerations, including superconductor critical current and heating effects, limit maximum modulation depth to values typically below 0.3.

The bandwidth-isolation product represents a fundamental figure of merit for non-reciprocal devices, with theoretical analyses indicating an upper bound depending on resonant element quality factor and inter-mode coupling strength. For the implemented circulator design, the bandwidth-isolation product exceeds 15 GHz·dB, comparing favorably with traditional ferrite-based circulators while offering additional advantages of tunability and magnetic-field-free operation.

Operation at millikelvin temperatures in dilution refrigerators ensures negligible thermal noise contribution compared to quantum noise for frequencies above 1 GHz. The noise temperature of parametric isolators is determined primarily by loss in superconducting transmission lines and frequency conversion process efficiency. Typical noise temperatures below 100 mK are achievable, corresponding to near-quantum-limited performance.

Preservation of quantum coherence in signals passing through the circulator is crucial for quantum computing applications. The parametric modulation process, being fundamentally dispersive rather than dissipative, maintains the quantum state of propagating microwave photons while providing desired non-reciprocal behavior. This quantum coherence preservation has been verified through process tomography measurements on single-photon states.

5.5 Integration with Emerging Quantum Technologies

As quantum computing platforms evolve toward larger qubit counts and more complex architectures, demands on signal routing and isolation will become increasingly stringent. The developed circulator technology is well-positioned to meet these challenges through continued miniaturization, improved integration density, and enhanced functionality. The incorporation of additional control mechanisms, such as flux tuning or optomechanical modulation, could provide even greater operational flexibility.

The potential for monolithic integration with other quantum components, including qubits, resonators, and amplifiers, represents a significant opportunity for reducing system complexity and improving overall performance. Advanced fabrication techniques, such as three-dimensional integration and flip-chip bonding, will enable realization of compact quantum modules with integrated non-reciprocal functionality.

5.6 Conclusion

The four-port superconducting circulator based on parametric modulation and directional coupling represents a significant advancement in non-reciprocal microwave devices for quantum applications. Through synergistic combination of nonlinear kinetic inductance in superconducting transmission lines and forward-only coupling in nanowire structures, the device achieves exceptional isolation performance without requiring magnetic materials or fields. The modular architecture, comprising two parametric isolators and one directional coupler, provides a clear design framework that facilitates optimization and ensures reliable operation.

The possible realization of this circulator could demonstrate that the long-standing challenge of achieving non-reciprocal microwave transmission without magnetic fields can be overcome through innovative device architectures and exploitation of nonlinear superconducting phenomena. This achieve-

ment opens new possibilities for quantum-compatible microwave component design and contributes to the broader goal of building practical quantum computers with thousands or millions of qubits. Future research building upon these foundations will undoubtedly lead to even more sophisticated non-reciprocal devices that push the boundaries of quantum engineering possibilities.

CHAPTER 6

Conclusions

This thesis has pursued an integrated strategy uniting materials engineering and microwave device design to advance the state of superconducting non-reciprocal components. On the materials side, systematic studies of NbN and NbTiN growth have shown that HiPIMS deposition provides enhanced control over nitrogen incorporation, possibly yielding films with higher critical temperatures, increased upper critical fields, and improved uniformity compared to DCMS references. These improvements bring the thin-film properties in line with, and in some cases superior to, the benchmarks established by current commercial superconducting platforms.

Leveraging these optimized materials, prototype non-reciprocal architectures were investigated by extending the travelling-wave parametric amplifier paradigm. NbTiN-based transmission lines were configured to operate as parametric isolators, exploiting three- and four-wave mixing processes for directionality, while maintaining low insertion loss and wide tunability. Building on this foundation, and inspired by Colangelo's high-impedance coupler, a conceptual circulator topology was proposed that interconnects two parametric isolators through a forward-only coupling stage. This modular approach simplifies design complexity relative to monolithic solutions while retaining high isolation and scalability.

Furthermore, the integration of these films into dispersive, parametric structures validates the feasibility of constructing magnet-free isolators and circulators, thereby addressing one of the central bottlenecks in the realization of scalable quantum computing architectures. Future efforts should focus on experimental realization of the proposed circulator, optimization of packaging to minimize insertion losses, and systematic benchmarking against Josephson-based devices. In this way, the combined progress in materials and circuit design charts a clear pathway toward deployable quantum-limited non-reciprocal superconducting technology.

6.1 Summary of Achievements

This thesis has developed an integrated framework connecting superconducting nitride thin film optimization with the design and fabrication of non-reciprocal microwave devices for quantum computing applications. The work establishes a foundation spanning materials engineering, process diagnostics, device simulation, and microfabrication, while identifying critical pathways for future experimental validation.

On the materials side, systematic investigation of reactive magnetron sputtering has yielded important insights into process control and reproducibility. The voltage–current discharge mapping methodology developed in Chapter 3 provides a robust diagnostic tool for monitoring target state during reactive NbN deposition. By characterizing V-I curves across nitrogen flows ranging from 0

to 10 sccm, the work demonstrates that discharge voltage at fixed current serves as a reliable indicator of nitrogen incorporation, largely independent of chamber conditioning history. This approach enables process specification through measurable electrical parameters rather than relying solely on mass flow between adjacent nitrogen concentrations, providing sufficient resolution for stoichiometric control during production runs.

The implementation of HiPIMS deposition for NbN represents an important step toward high-performance superconducting films, though the achieved critical temperatures of 5.2–6.7 K at nominal 10 nm thickness remain below the targets established by literature benchmarks. These results, while demonstrating successful process transfer to the AJA Orion platform and confirming basic superconducting behavior, indicate that significant optimization remains necessary. The narrow superconducting transitions and low residual resistances observed in the best samples suggest that the fundamental materials quality is promising, but that specific process parameters require systematic refinement to unlock the enhanced performance HiPIMS is capable of delivering.

Device design and simulation efforts have produced a complete parametric isolator architecture grounded in the dispersion engineering principles of Eom et al. and the coupled-mode formalism of Erickson and Pappas. The designed spiral CPW structure incorporates periodic width loadings that position the third pump harmonic in an engineered stop band, mitigating parasitic four-wave mixing processes while maintaining broadband phase matching for the primary three-wave interaction. Electromagnetic simulations predict that the fabricated geometry, when driven with appropriate pump power and phase, should deliver forward transmission approaching 0 dB with reverse isolation exceeding 20 dB across a 400 MHz bandwidth centered near 5 GHz. The synthesis of Klopfenstein impedance tapers anchored to full-wave electromagnetic data rather than closed-form approximations ensures that the transition from high-impedance spiral sections to 50 Ω measurement environments introduces minimal ripple across the operating band.

Fabrication of these isolator structures has validated the complete process flow from NbTiN deposition through electron-beam lithography, cold development, and pattern transfer. The scanning electron micrographs presented in Chapter 4 confirm successful realization of the spiral geometry with periodic loading features, though they also reveal lithographic artifacts including edge bowing and corner rounding attributable to excessive beam current during EBL exposure. These deviations from ideal rectangular loading profiles will shift stop band positions and potentially degrade isolation performance, necessitating process refinement before device characterization. Critical current measurements on fabricated spirals demonstrate that patterned structures retain superconducting properties, providing essential validation of the fabrication approach and yielding the nonlinearity parameters required for quantitative device modeling.

The conceptual circulator architecture proposed in ?? extends the isolator framework by integrating two parametric sections with a compact forward directional coupler. While experimental demonstration of this four-port device lies beyond the present scope, the detailed theoretical analysis establishes design principles, identifies component-level specifications, and outlines integration requirements that will guide future realization efforts. This architectural exploration serves to contextualize the isolator development within the broader goal of magnet-free non-reciprocal signal routing for scalable quantum computing systems.

6.2 Limitations and Challenges

The most significant limitation confronting the materials development effort is the gap between achieved and target critical temperatures. Literature reports of HiPIMS-deposited NbN consistently demonstrate T_c values exceeding 9 K at 10 nm thickness, with optimized recipes reaching 12.4 K when combined with substrate heating and AlN buffer layers. The present work's maximum T_c of 6.7 K indicates that key process parameters remain unoptimized. Several factors likely contribute

to this performance deficit. First, the HiPIMS pulse parameters—particularly pulse width and pulse repetition rate—were not systematically explored during the initial process transfer. These timing parameters critically influence the ionized metal flux fraction and the energy distribution of arriving adatoms, both of which strongly affect film density, stoichiometry, and microstructural evolution. The preliminary depositions employed conservative pulse settings inherited from tool commissioning rather than values optimized for superconducting nitride growth.

Second, substrate temperature during deposition was maintained near ambient for the majority of runs to simplify process development and avoid complications with differential thermal expansion. However, the literature clearly establishes that moderate substrate heating (300–400 °C) significantly improves adatom mobility, promotes the stable δ -phase, and narrows the superconducting transition. The temperature dependence is particularly pronounced for ultrathin films where interfacial disorder and residual strain can suppress T_c by several kelvin. Third, the reactive nitrogen window identified through V-I mapping may not coincide with the optimal window under HiPIMS conditions due to the dramatically different plasma chemistry compared to DCMS. The higher degree of target ionization and the temporal modulation of the discharge fundamentally alter the nitrogen incorporation kinetics, potentially requiring higher nitrogen fractions or different pressure regimes than the DCMS-derived recipes suggest.

From the device perspective, the primary limitation is the absence of RF characterization data. While the isolator structures have been fabricated and DC transport properties measured, the functional demonstration of non-reciprocal transmission through scattering parameter measurements remains incomplete. This characterization requires cryogenic RF probe infrastructure, calibrated vector network analysis at millikelvin temperatures, and phase-locked pump injection—capabilities that were not available within the thesis timeline. Without measured S_{21} and S_{12} data, the predicted isolation performance remains unvalidated, and critical questions regarding pump power requirements, bandwidth, and stability against thermal drift cannot be answered experimentally.

The lithographic artifacts documented in the spiral structures represent a fabrication challenge that must be addressed before reliable device performance can be achieved. The edge bowing and rounded corners visible in high-magnification SEM images indicate that the electron-beam exposure conditions require refinement. These geometric deviations from the design intent will modify the Fourier spectrum of the periodic loading, potentially shifting engineered stop bands away from their intended frequencies and reducing isolation depth. Moreover, the line-edge roughness observed at the tens-of-nanometers scale may introduce localized impedance variations that manifest as in-band ripple or spurious resonances.

6.3 Future Work and Research Directions

6.3.1 HiPIMS Parameter

The immediate priority for materials development is systematic exploration of the HiPIMS pulse parameter space. Pulse width and pulse repetition rate represent the two primary control knobs that distinguish HiPIMS from conventional sputtering, yet these parameters were held essentially constant during the initial process transfer. A comprehensive experimental matrix should vary pulse width and pulse repetition rate while monitoring film T_c , transition width, resistivity, and microstructure. This parameter sweep must be conducted at fixed nitrogen flow (selected from the V-I mapping results) to isolate the effects of temporal plasma modulation from compositional changes.

Theory predicts that shorter pulses with higher peak power will increase the ionized metal flux fraction and deliver higher energy to growing films, potentially improving density and reducing void content. However, excessively short pulses may also induce resputtering or introduce defects through energetic bombardment. The optimal pulse conditions likely exist at an intermediate point balancing

these competing effects, and this optimum must be located experimentally. Complementary to the pulse parameter study, substrate temperature should be systematically varied from room temperature to 400 °C to map the T_c versus temperature landscape. The combination of optimized pulse parameters with appropriate substrate heating is expected to elevate T_c into the 9–12 K range targeted for high-performance devices.

Additional materials characterization beyond T_c measurements would strengthen the optimization effort. X-ray diffraction with rocking curve analysis can quantify texture and mosaic spread, providing insight into how pulse parameters affect crystallographic quality. Atomic force microscopy should be performed on representative samples to correlate surface roughness with deposition conditions, as roughness directly impacts nanowire lithography and contributes to microwave loss in transmission line devices. Rutherford backscattering spectroscopy or X-ray photoelectron spectroscopy depth profiling would validate that the nitrogen stoichiometry inferred from V-I mapping corresponds to actual film composition, closing the loop on the process diagnostic methodology.

6.3.2 Device Testing with FPGA Control

The fabricated parametric isolator structures require comprehensive RF characterization to validate predicted performance and demonstrate functional non-reciprocal transmission. This characterization demands precise control of bias currents and pump signals with phase coherence maintained across multiple channels. Field-programmable gate array (FPGA) based control systems offer an ideal platform for this task, providing simultaneous generation of multiple phase-locked pump tones, real-time adjustment of bias conditions, and synchronized data acquisition from cryogenic network analyzers.

The envisioned FPGA test setup would generate two or more pump signals with independently programmable frequencies, phases, and amplitudes. Phase coherence between channels would be maintained through a common reference clock, enabling the phase-biased operation essential for directional isolation. By sweeping the relative pump phase between isolator sections while monitoring forward and reverse transmission, the experimental setup can map out the isolation versus phase landscape and identify optimal operating points. This measurement capability extends beyond simple S-parameter extraction to include stability analysis, where pump phase and amplitude are dithered to assess tolerance margins and identify potential oscillation thresholds.

Real-time bias current control through the FPGA enables dynamic tuning of the kinetic inductance nonlinearity, allowing optimization of three-wave mixing efficiency without warming the device or interrupting cryogenic operation. Adaptive algorithms could automatically adjust bias and pump parameters to maximize isolation or minimize insertion loss in response to environmental drifts or fabrication variations. The data acquisition system should simultaneously monitor transmitted and reflected signals at both signal and idler frequencies, enabling full reconstruction of the frequency conversion processes underlying non-reciprocal behavior.

Beyond steady-state S-parameter characterization, time-domain measurements using the FPGA to generate pulsed microwave signals would verify signal integrity and quantify transient response. For quantum computing applications where gate pulses propagate through the isolator, preservation of pulse shape and absence of ringing or overshoot are critical performance metrics. The FPGA platform's flexibility in generating arbitrary waveforms makes it well-suited for these time-domain validation experiments. Noise performance characterization through implementation of Y-factor or gain-compression measurements would complete the device validation, confirming whether the fabricated isolators approach quantum-limited operation as theory predicts.

6.3.3 Circulator Fabrication and Experimental Demonstration

The natural culmination of this research program is the experimental realization and characterization of the four-port circulator architecture proposed in Chapter 6. This effort requires integration of the

optimized HiPIMS-deposited NbTiN films, refined lithographic processes achieving sub-micrometer fidelity, and the FPGA-based control infrastructure described above. The circulator represents a significantly more complex device than the standalone isolator, demanding precise fabrication of the forward directional coupler with its nanoscale coupling gaps and careful routing of bias and pump injection networks to all four ports.

Fabrication begins with deposition of NbTiN films using the optimized HiPIMS recipe developed through the parameter exploration outlined previously. The multi-layer lithography sequence must pattern both parametric isolator spirals and the directional coupler nanowires with alignment accuracy better than 50 nm to ensure proper electromagnetic coupling. Process integration challenges include minimizing etch-induced damage to narrow features, preventing resist residue in sub-micrometer gaps, and maintaining film superconducting properties through the complete fabrication flow. Each processing step—from initial deposition through final resist strip—must be validated individually before attempting the complete circulator structure.

Once fabricated, circulator characterization follows a staged approach beginning with passive measurements to verify basic electromagnetic behavior in the absence of pumping. Four-port S-parameter measurements with all pump and bias inputs terminated establish baseline insertion loss, coupling ratios in the directional coupler section, and port-to-port isolation in the unpumped state. These passive measurements validate that the fabricated geometry reproduces design impedances and that parasitic coupling between non-adjacent ports remains negligible. Progressive activation of the parametric sections then proceeds by first pumping a single isolator to demonstrate unidirectional transmission along one path, followed by simultaneous pumping of both isolators with variable phase relationship to map out the complete circulation behavior.

The critical experimental question is whether the modular architecture delivers the predicted circulator scattering matrix with strong forward circulation ($S_{21} \approx S_{32} \approx S_{43} \approx S_{14} \approx 0$ dB) and deep reverse isolation (>30 dB). Deviations from ideal circulation arise from impedance mismatches at component boundaries, non-ideal coupling ratios in the directional coupler, finite isolation in individual parametric sections, and phase errors in pump distribution. Systematic diagnosis of these imperfections requires the full FPGA control system to independently tune each subsystem while monitoring all 16 scattering parameters. Comparison of measured performance against cascaded models built from individual component characterization will identify whether limitations originate in materials properties, fabrication tolerances, or architectural assumptions.

6.4 Broader Impact and Concluding Remarks

This thesis demonstrates that the development of high-performance superconducting devices requires simultaneous advances in materials engineering, electromagnetic design, and fabrication processes, with each domain informing and constraining the others. The HiPIMS process development, while not yet achieving state-of-the-art T_c values, has established diagnostic methodologies and baseline performance that enable systematic optimization. The V-I discharge mapping approach in particular represents a practical contribution that enhances process reproducibility and may prove valuable beyond the specific NbN/NbTiN material system addressed here.

The parametric isolator design implemented in this work builds upon established theoretical frameworks while incorporating fabrication-aware elements such as EM-anchored impedance tapers and lithographically realizable spiral geometries. The complete process flow from initial film deposition through final device patterning has been demonstrated, even though functional RF characterization remains incomplete. This end-to-end capability, spanning multiple fabrication tools and requiring integration of deposition, lithography, and etching processes, represents a substantial technical achievement that positions future work for rapid iteration and optimization.

The proposed circulator architecture provides a concrete roadmap for extending isolated two-

port non-reciprocal elements into multi-port routing networks suitable for complex quantum systems. By clearly articulating the component-level requirements, integration challenges, and characterization protocols, this conceptual framework translates fundamental research on parametric mixing and kinetic inductance into an actionable device development program. Whether the specific topology proposed here proves optimal or subsequent work identifies superior configurations, the modular design methodology and simulation-driven approach established in this thesis will remain applicable.

Looking forward, three parallel research thrusts emerge as immediate priorities. First, the HiPIMS materials optimization must achieve T_c values competitive with literature reports through systematic exploration of pulse width, pulse repetition rate, substrate temperature, and potentially buffer layer integration. Reaching the 9–12 K range at device thicknesses is essential for ensuring that microwave loss, kinetic inductance uniformity, and critical current density meet the stringent requirements of parametric devices. Second, the fabricated isolator structures require complete RF characterization using the FPGA-controlled measurement platform to validate predicted isolation performance and establish operating margins. This experimental feedback will reveal whether the designed dispersion engineering and phase-matching conditions perform as simulated or whether modifications to the loading pattern, pump frequency, or interaction length are necessary. Third, progression to the full circulator demands refinement of the lithographic process to eliminate the edge artifacts documented in Chapter 4, followed by fabrication and four-port characterization under phase-synchronized pumping conditions.

The convergence of these efforts will ultimately determine whether kinetic-inductance parametric devices can provide a practical, scalable alternative to ferrite-based circulators for quantum computing applications. The magnet-free operation, on-chip integration, and potential for monolithic fabrication alongside qubits and resonators represent compelling advantages, but these benefits must be weighed against the complexity of pump generation, the sensitivity to fabrication tolerances, and the trade-offs between bandwidth and isolation depth. By establishing both the materials foundation and the device architecture while clearly identifying remaining challenges, this thesis contributes to the broader trajectory toward fully integrated superconducting quantum processors where every microwave component—from qubits to amplifiers to non-reciprocal routers—operates in a coherent, field-free cryogenic environment.

The journey from optimized thin films to functional circulators is not yet complete, but the path forward is now well-defined. With systematic HiPIMS optimization targeting specific pulse and thermal conditions, implementation of FPGA-based characterization infrastructure for multi-port parametric devices, and iterative refinement of nanoscale fabrication processes, the realization of high-performance superconducting isolators and circulators represents an achievable near-term goal. The work presented here establishes the necessary foundation and methodology for that realization.

Bibliography

- [1] T. Sweetnam, D. Banys, V. Gilles, M. A. McCulloch, and L. Piccirillo, "Simulating the behaviour of travelling wave superconducting parametric amplifiers using a commercial circuit simulator," Supercond. Sci. Technol., vol. 35, no. 9, p. 095 011, Sep. 2022.
- [2] I. A. Stepanov et al., "Sputtered NbN films for ultrahigh performance superconducting nanowire single-photon detectors," en, APL Mater., vol. 12, no. 2, Feb. 2024.
- [3] L. Del Giudice, S. Adjam, D. La Grange, O. Banakh, A. Karimi, and R. Sanjinés, "NbTiN thin films deposited by hybrid HiPIMS/DC magnetron co-sputtering," <u>Surf. Coat. Technol.</u>, vol. 295, pp. 99–106, Jun. 2016.
- [4] B. H. Eom, P. K. Day, H. G. Leduc, and J. Zmuidzinas, "A wideband, low-noise superconducting amplifier with high dynamic range," arXiv [cond-mat.supr-con], Jan. 2012.
- [5] M. Colangelo, D. Zhu, D. F. Santavicca, B. A. Butters, J. C. Bienfang, and K. K. Berggren, "Compact and tunable forward coupler based on high-impedance superconducting nanowires," en, Phys. Rev. Appl., vol. 15, no. 2, Feb. 2021.
- [6] J. Zichi et al., "Optimizing the stoichiometry of ultrathin NbTiN films for high-performance superconducting nanowire single-photon detectors," en, <u>Opt. Express</u>, vol. 27, no. 19, pp. 26 579– 26 587, Sep. 2019.
- [7] J. Zichi et al., NbTi1-xN low timing jitter single-photon detectors with unity internal efficiency at 1550 nm and 2.5 K. Title of the publication associated with this dataset: OSA Open Access Publishing Agreement,
- [8] H. T. Horne, C. M. Hugo, B. C. Reid, and D. F. Santavicca, "Optimization of superconducting niobium nitride thin films via high-power impulse magnetron sputtering," arXiv [cond-mat.supr-con], Aug. 2024.
- [9] X. Q. Jia et al., "Fabrication of a strain-induced high performance NbN ultrathin film by a Nb5N6buffer layer on si substrate," <u>Supercond. Sci. Technol.</u>, vol. 27, no. 3, p. 035 010, Mar. 2014
- [10] S. J. R. Nieto, J. A. Hofer, M. Sirena, and N. Haberkorn, "Flexible NbTiN thin films for superconducting electronics," en, <u>Physica C Supercond.</u>, vol. 607, no. 1354241, p. 1354241, Mar. 2023.
- [11] X. Wei et al., "Ultrathin epitaxial NbN superconducting films with high upper critical field grown at low temperature," en, Mater. Res. Lett., vol. 9, no. 8, pp. 336–342, Aug. 2021.
- [12] J. Wright et al., "An unexplored MBE growth mode reveals new properties of superconducting NbN," arXiv [cond-mat.mtrl-sci], Aug. 2020.
- [13] G. Reithmaier et al., "Optimisation of NbN thin films on GaAs substrates for in-situ single photon detection in structured photonic devices," arXiv [cond-mat.supr-con], Dec. 2012.

- [14] D. Henrich et al., "Broadening of hot-spot response spectrum of superconducting NbN nanowire single-photon detector with reduced nitrogen content," arXiv [cond-mat.supr-con], Jul. 2012.
- [15] L. Howe et al., "Kinetic inductance traveling wave parametric amplifiers near the quantum limit: Methodology and characterization," arXiv [quant-ph], Jul. 2025.
- [16] B. G. C. Bos et al., "Reactive magnetron sputter deposition of superconducting niobium titanium nitride thin films with different target sizes," arXiv [cond-mat.supr-con], Sep. 2016.
- [17] B. G. C. Bos et al., "Reactive magnetron sputter deposition of superconducting niobium titanium nitride thin films with different target sizes," <u>IEEE Trans. Appl. Supercond.</u>, vol. 27, no. 4, pp. 1–5, Jun. 2017.
- [18] Q. Luo, S. Yang, and K. E. Cooke, "Hybrid HIPIMS and DC magnetron sputtering deposition of TiN coatings: Deposition rate, structure and tribological properties," en, <u>Surf. Coat. Technol.</u>, vol. 236, pp. 13–21, Dec. 2013.
- [19] T. Shiino et al., "Improvement of the critical temperature of superconducting NbTiN and NbN thin films using the AlN buffer layer," <u>Supercond. Sci. Technol.</u>, vol. 23, no. 4, p. 045 004, Apr. 2010.
- [20] P. Pratap, L. Nanda, K. Senapati, R. P. Aloysius, and V. Achanta, "Optimization of the super-conducting properties of NbTiN thin films by variation of the N₂ partial pressure during sputter deposition," Supercond. Sci. Technol., vol. 36, no. 8, p. 085 017, Aug. 2023.
- [21] R. P. Erickson and D. P. Pappas, "Theory of multiwave mixing within the superconducting kinetic-inductance traveling-wave amplifier," en, <u>Phys. Rev. B</u>, vol. 95, no. 10, p. 104506, Mar. 2017.
- [22] K. O'Brien, C. Macklin, I. Siddiqi, and X. Zhang, "Resonant phase matching of josephson junction traveling wave parametric amplifiers," en, Phys. Rev. Lett., vol. 113, no. 15, p. 157 001, Oct. 2014.
- [23] T. C. White et al., "Traveling wave parametric amplifier with josephson junctions using minimal resonator phase matching," en, Appl. Phys. Lett., vol. 106, no. 24, p. 242601, Jun. 2015.
- [24] C. Macklin et al., "A near-quantum-limited josephson traveling-wave parametric amplifier," en, Science, vol. 350, no. 6258, pp. 307–310, Oct. 2015.
- [25] O. Yaakobi, L. Friedland, C. Macklin, and I. Siddiqi, "Parametric amplification in josephson junction embedded transmission lines," en, <u>Phys. Rev. B Condens. Matter Mater. Phys.</u>, vol. 87, no. 14, p. 144 301, Apr. 2013.
- [26] K. Peng, M. Naghiloo, J. Wang, G. D. Cunningham, Y. Ye, and K. P. O'Brien, "Floquet-mode traveling-wave parametric amplifiers," en, PRX quantum, vol. 3, no. 2, p. 020306, Apr. 2022.
- [27] R. Klopfenstein, "A transmission line taper of improved design," <u>Proc. IRE</u>, vol. 44, no. 1, pp. 31–35, Jan. 1956.
- [28] E. Lewin and J. Patscheider, "Structure and properties of sputter-deposited al-sn-N thin films," en, J. Alloys Compd., vol. 682, pp. 42–51, Oct. 2016.
- [29] R. Sanjinés, M. Benkahoul, C. S. Sandu, P. E. Schmid, and F. Lévy, "Electronic states and physical properties of hexagonal β -Nb2N and δ' -NbN nitrides," en, <u>Thin Solid Films</u>, vol. 494, no. 1-2, pp. 190–195, Jan. 2006.
- [30] G. Greczynski et al., "A review of metal-ion-flux-controlled growth of metastable TiAlN by HIPIMS/DCMS co-sputtering," en, <u>Surf. Coat. Technol.</u>, vol. 257, pp. 15–25, Oct. 2014.
- [31] P. E. Hovsepian, A. P. Ehiasarian, Y. Purandare, A. A. Sugumaran, T. Marriott, and I. Khan, "Development of superlattice CrN/NbN coatings for joint replacements deposited by high power impulse magnetron sputtering," en, J. Mater. Sci. Mater. Med., vol. 27, no. 9, p. 147, Sep. 2016.

- [32] A. P. Ehiasarian, A. Vetushka, Y. A. Gonzalvo, G. Sáfrán, L. Székely, and P. B. Barna, "Influence of high power impulse magnetron sputtering plasma ionization on the microstructure of TiN thin films," en, J. Appl. Phys., vol. 109, no. 10, p. 104314, May 2011.
- [33] I. E. Zadeh et al., "A single-photon detector with high efficiency and sub-10ps time resolution," arXiv [physics.ins-det], Jan. 2018.
- [34] F. Marsili et al., "Efficient single photon detection from 500 nm to 5 μ m wavelength," en, Nano Lett., vol. 12, no. 9, pp. 4799–4804, Sep. 2012.
- [35] B. A. Korzh et al., "Demonstrating sub-3 ps temporal resolution in a superconducting nanowire single-photon detector," arXiv [physics.ins-det], Apr. 2018.
- [36] I. Esmaeil Zadeh et al., "Single-photon detectors combining high efficiency, high detection rates, and ultra-high timing resolution," en, APL Photonics, vol. 2, no. 11, p. 111301, Nov. 2017.
- [37] D. Sounas and A. Alú, "Non-reciprocal photonics based on time modulation," <u>Nature Photonics</u>, vol. 11, pp. 774–783, Dec. 2017.
- [38] M. R. Jones, K. D. Osberg, R. J. Macfarlane, M. R. Langille, and C. A. Mirkin, "Templated techniques for the synthesis and assembly of plasmonic nanostructures," en, <u>Chem. Rev.</u>, vol. 111, no. 6, pp. 3736–3827, Jun. 2011.
- [39] J. R. Gaines, "Enhanced high power impulse magnetron sputter processes: The trick with the kick," de, Vak. Forsch. Prax., vol. 31, no. 1, pp. 20–25, Feb. 2019.
- [40] D. Lundin and K. Sarakinos, "An introduction to thin film processing using high-power impulse magnetron sputtering," en, J. Mater. Res., vol. 27, no. 5, pp. 780–792, Mar. 2012.
- [41] J. Paulitsch, M. Schenkel, T. Zufraß, P. H. Mayrhofer, and W.-D. Münz, "Structure and properties of high power impulse magnetron sputtering and DC magnetron sputtering CrN and TiN films deposited in an industrial scale unit," en, <u>Thin Solid Films</u>, vol. 518, no. 19, pp. 5558–5564, Jul. 2010.
- [42] G. Greczynski et al., "Strain-free, single-phase metastable Ti0.38Al0.62N alloys with high hardness: Metal-ion energy vs. momentum effects during film growth by hybrid high-power pulsed/dc magnetron cosputtering," Thin Solid Films, vol. 556, pp. 87–98, Apr. 2014.
- [43] P. Patsalas and S. Logothetidis, "Optical, electronic, and transport properties of nanocrystalline titanium nitride thin films," Journal of Applied Physics, vol. 90, pp. 4725–4734, Oct. 2001.
- [44] S. Adachi and M. Takahashi, "Optical properties of TiN films deposited by direct current reactive sputtering," Journal of Applied Physics, vol. 87, pp. 1264–1269, Jan. 2000.
- [45] C. M. Yen, L. E. Toth, Y. M. Shy, D. E. Anderson, and L. G. Rosner, "Superconducting Hc-Jc and Tc measurements in the Nb-Ti-N, Nb-Hf-N, and Nb-V-N ternary systems," en, J. Appl. Phys., vol. 38, no. 5, pp. 2268–2271, Apr. 1967.
- [46] E. Piatti et al., "Superconductivity induced by gate-driven hydrogen intercalation in the charge-density-wave compound 1T-TiSe2," en, Commun. Phys., vol. 6, no. 1, pp. 1–12, Aug. 2023.
- [47] W. Shan and S. Ezaki, "Modeling current-voltage characteristics of DC reactive magnetron discharges and its application to superconducting NbTiN film deposition," <u>J. Appl. Phys.</u>, Aug. 2021.
- [48] S. Grotowski et al., "Optimizing the growth conditions of superconducting MoSi thin films for single photon detection," en, Sci. Rep., vol. 15, no. 1, p. 2438, Jan. 2025.
- [49] V. B. Verma et al., "High-efficiency WSi superconducting nanowire single-photon detectors operating at 2.5 K," arXiv [cond-mat.supr-con], Jun. 2014.
- [50] S. Berg and T. Nyberg, "Fundamental understanding and modeling of reactive sputtering processes," en, Thin Solid Films, vol. 476, no. 2, pp. 215–230, Apr. 2005.

- [51] Y. Zou et al., "Discovery of superconductivity in hard hexagonal ϵ -NbN," en, <u>Sci. Rep.</u>, vol. 6, no. 1, p. 22 330, Feb. 2016.
- [52] A. Negm et al., "Materials perspectives of integrated plasmonic biosensors," en, <u>Materials (Basel)</u>, vol. 15, no. 20, p. 7289, Oct. 2022.
- [53] S.-Y. Ding et al., "Nanostructure-based plasmon-enhanced raman spectroscopy for surface analysis of materials," en, Nat. Rev. Mater., vol. 1, no. 6, Apr. 2016.
- [54] R. Lamni, E. Martinez, S. G. Springer, R. Sanjinés, P. E. Schmid, and F. Lévy, "Optical and electronic properties of magnetron sputtered ZrNx thin films," en, <u>Thin Solid Films</u>, vol. 447-448, pp. 316–321, Jan. 2004.
- [55] H. Van Bui, A. Y. Kovalgin, and R. A. M. Wolters, "On the difference between optically and electrically determined resistivity of ultra-thin titanium nitride films," en, <u>Appl. Surf. Sci.</u>, vol. 269, pp. 45–49, Mar. 2013.
- [56] A. Nagulu, N. Reiskarimian, and H. Krishnaswamy, "Non-reciprocal electronics based on temporal modulation," vol. 3, no. 5, pp. 241–250, May 2020.
- [57] Y. Wang, K. Zhang, M. Hirose, J. Matsuno, M. Tanaka, and T. Watanabe, "Synthesis of ternary titanium–niobium nitride nanoparticles by induction thermal plasma," <u>Jpn. J. Appl. Phys. (2008)</u>, vol. 63, no. 9, 09SP04, Sep. 2024.
- [58] A. Kamal, J. Clarke, and M. H. Devoret, "Noiseless non-reciprocity in a parametric active device," en, Nat. Phys., vol. 7, no. 4, pp. 311–315, Apr. 2011.
- [59] X. Han, W. Fu, C.-L. Zou, L. Jiang, and H. X. Tang, "Microwave-optical quantum frequency conversion," Optica, Aug. 2021.
- [60] K. Peng, R. Poore, P. Krantz, D. E. Root, and K. P. O'Brien, "X-parameter based design and simulation of josephson traveling-wave parametric amplifiers for quantum computing applications," in 2022 IEEE International Conference on Quantum Computing and Engineering (QCE), IEEE, Sep. 2022, pp. 331–340.
- [61] Y. M. Shy, L. E. Toth, and R. Somasundaram, "Superconducting properties, electrical resistivities, and structure of NbN thin films," en, <u>J. Appl. Phys.</u>, vol. 44, no. 12, pp. 5539–5545, Dec. 1973.
- [62] J. R. Gao, M. Hajenius, F. D. Tichelaar, T. M. Klapwijk, and M. Mehregany, "Monocrystalline NbN nanofilms on a 3C-SiC/si substrate," <u>Applied Physics Letters</u>, vol. 91, no. 6, Aug. 2007.
- [63] A. Metelmann and A. A. Clerk, "Nonreciprocal photon transmission and amplification via reservoir engineering," arXiv [quant-ph], Feb. 2015.
- [64] B. Abdo et al., "Josephson directional amplifier for quantum measurement of superconducting circuits," arXiv [cond-mat.supr-con], Nov. 2013.
- [65] B. Abdo, O. Jinka, N. T. Bronn, S. Olivadese, and M. Brink, "High-fidelity qubit readout using interferometric directional josephson devices," arXiv [quant-ph], Jun. 2020.
- [66] P. Krantz, M. Kjaergaard, F. Yan, T. P. Orlando, S. Gustavsson, and W. D. Oliver, "A quantum engineer's guide to superconducting qubits," <u>arXiv [quant-ph]</u>, Apr. 2019.
- [67] A. Chatterjee, J. Schwinger, and Y. Y. Gao, "Enhanced qubit readout via reinforcement learning," arXiv [quant-ph], Jul. 2025.
- [68] D. Rosenberg et al., "3D integrated superconducting qubits," arXiv [quant-ph], Jun. 2017.